Modeling of Particle Transport in Commercial Electrostatic Precipitators

Zamany, Jamshid; Larsen, Poul Scheel

Publication date:
1992

Document Version
Publisher's PDF, also known as Version of record

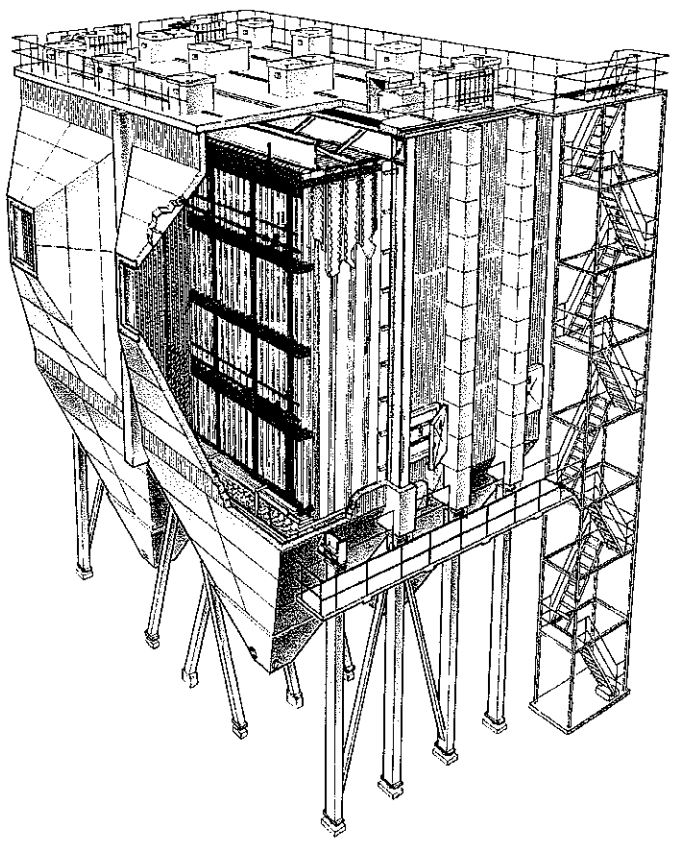

Modeling of Particle Transport in Commercial Electrostatic Precipitators

By
Jamshid Zamany

FLSmiljo

Modeling of Particle Transport in Commercial Electrostatic Precipitators

By

Jamshid Zamany

ERHVERVSFORSKERPROJEKT (Ph.D), **EF 316**
Akademiet for de Tekniske Videnskaber, ATV
Department of Fluid Mechanics, Technical University of Denmark
FLS miljø a/s, Enviromental Managements, Copenhagen, Denmark

ISBN 87–984457–0–7

September 1992

Preface

This report forms the basic of my Ph.D. thesis which is financially supported by the FLS–miljø company and the Danish Academy of Technical Science (ATV). The thesis is based on a theoretical and experimental study performed during the period January 1990 to September 1992 at both the Department of Fluid Mechanics (DFM), Technical University of Denmark and the FLS–miljø company.

The study has been carried out under the supervision of Professor, Ph.D, Poul Scheel Larsen and Lic. techn. Leif Lind, FLS–miljø, to whom I would like to express my best appreciations for their continuous supports and inspiring and suggestive discussions. Thanks also to my colleagues in FLS–miljø and DFM for their help with the experimental setup.

Finally, I would like to thank may family for their support and patience during the last part of my study.

September 1992

Jamshid Zamany

Abstract

The spatial distribution of particle concentration in commercial electrostatic precipitators (ESP) is modeled numerically. The model involves numerically solution of the three–dimensional electric field, the flow field, and the particle transport throughout the ESP.

Maxwell equations for electrostatic fields with influence of ionic and particle space charge for three–dimensional complex geometries are solved numerically.
Fluctuations of space charge field correlated with electric field fluctuations give raise to charge diffusion between the electrodes and collector plates. These correlations are modeled numerically.
Among non–ideal electrical effects, the back corona phenomenon has been investigated and a simple numerical estimation for prediction of this phenomenon is developed.
The current–charge and the potential–charge relationships may contribute to understanding of the corona discharge phenomenon, therefore these relationships for both the negative and positive corona discharge are investigated.
Meassurements of current density distribution at the collector plate has made it possible to examine the reliability of the numerical model. The comparisons between measurements and calculations show good agreement.

The velocity field inside the ESP is influenced by the electric field and the geometrical configuration. The influence of the electric field on the flow patterns inside the ESP is investigated numerically in two and three dimensions using the elliptic time–averaged Navier–Stokes equations with a constant eddy viscosity model.
LDA measurements of the velocity and the turbulence fields inside a labratory scale ESP are compared with numerical calculations. A basic experimental study of secondary flows due to electrical vorticity sources is reported. Numerical results for two dimensional flow show close agreement to experiments.
Particles with different size have different electrical drift velocity inside the LDA measuring volume which will be precived as turbulent fluctuations by the LDA system. The level of false turbulence due to particle size variations inside the LDA measuring volume is both estimated and measured. Re–entrainment of seeding particles (glycerin drops) close to collector plate have been measured and found to be negligible.

The transport of charged particles under the effect of three dimensional electric field, flow field and interaction between these parameters is calculated numerically. Results are compared with experimental data for particle concentration profile inside labratory scale ESP reported in the literature.
The particle charging mechanism is affected by the interactions between the particle and the ionic space charge within the charging electric field. In order to approach the physic of the electrostatic charging mechanism, these interactions are modeled numerically in the ESP model.

The resulting computer model developed for the prediction of the performance of ESP's takes the following parameters into account:
–total inlet dust concentration (represented by up to 10 monodisperse, spherical particle classes)
–particle turbulent diffusion coefficient and relative dielectric constant
–inlet gas velocity, density, dynamic viscosity, and turbulent diffusion coefficient
–electrode geometry, potential, and space charge at corona point
–ESP geometry, section length, and number of sections
–maximum permitted dust layer at collector plate and dust density.

The computer model provides the following output results along the ESP:
–total efficiency and penetration
–efficiency of each particle class
–mean dust concentration and size distribution for all particle classes
–dust layer thickness variation
–rapping time
–flow patterns
–electric field and space charge field
–mean current density
–current density distribution at collector plate.

The effect of bulk velocity and electrode–collector distance on ESP's efficiency and price has been investigated. The model results agree reasonably well with the performance of actual industrial precipitators even though negative effects such as re–entrainment and rapping losses are not modeled. Model calculations also suggest that current design practice is close to the optimum, but that improvements should be possible.

Abstract (in Danish)

En numerisk model til bestemmelse af den rumlige partikelkoncentrations fordeling i kommercielle elektrofiltre (ESP) er udviklet. Denne numeriske model omfatter løsning af det tredimensionale elektriske felt, strømningsfeltet og partikeltransporten gennem filteret.

De Maxwell'ske ligninger for elektrostatiske felter med indflydelse fra ion– ogpartikelrumladninger er løst numerisk for tredimensionale komplekse geometrier. Fluktuationer af rumladning korreleret med fluktuationer i det elektriske felt giveranledning til ladningsdiffusion mellem elektroderne og udfældningspladen. Disse korrelationer er modelleret numerisk. Blandt de ugunstige elektriske forhold er back–corona–fænomenet blevet undersøgt, og en simpel numerisk estimering er udviklet til at forudsige fænomenet. Strøm–ladningsrelationerne og spændings–ladningsrelationerne kan bidrage til forståelsen af corona udladningsmekanismen, og disse relationer er derfor undersøgt for negativ såvel som for positiv corona–udladning. Måling af strømtætheden på udfældningspladen har gjort det muligt at efterprøve pålideligheden af den numeriske model. Sammenligninger mellem målinger og beregninger viser god overensstemmelse.

Hastighedsfeltet i ESP er influeret af både det elektriske felt og den geometriske konfiguration. Det elektriske felts indflydelse på hastighedsfeltet i ESP er undersøgt numerisk i to og tre dimensioner ved brug af elliptiske tidsmidlede Navier–Stokes'ske ligninger med konstant eddy viskositetsmodel. LDA målinger af hastigheds– og turbulensfelter i en laboratorie–skala ESP er sammenlignet med numeriske beregninger. Et basalt, eksperimentelt studie af sekundære strømninger skabt af inhomogene elektriske volumenkræfter i systemet er udført, og de numeriske, todimensionale strømningsberegninger viser god overensstemmelse med de eksperimentelle data. Partikler af forskellig størrelse har forskellig elektrisk driftshastighed i LDA målevolumenet, hvilket vil blive opfattet som turbulente fluktuationer i LDA systemet. Niveauet af disse falske turbulenser er både estimeret og målt. Re–entrainment af seeding–partikler (glycerindråber) tæt ved udfældningspladen er blevet målt og har vist sig at være negligible.

Transport af ladede partikler i filteret under indflydelse af det tredimensionale elektriske felt, gasstrømningsfeltet og samspillet mellem disse er beregnet numerisk. Resultaterne er sammenlignet med eksperimentelle data for koncentrationsprofilet i en laboratorieskalamodel af ESP som rapporteret i litteraturen. Partikelladningsmekanismen er influeret af interaktioner mellem partikel– og ionrumladningen i det opladende elektriske felt. For at kunne tilnærme fysikken i denne elektrostatiske lademekanisme er disse interaktioner modelleret numerisk i ESP–modellen.

I den resulterende computermodel, der er udviklet til beregning af filtereffektivitet, indgår de følgende parametre som ind–data:

- total indløbsstøvkoncentration (repræsenteret med op til 10 forskellige kugleformede partikelstørrelser eller klasser
- turbulens–diffusionskoefficent af partikler og relativ dielektrisk konstant
- gasindløbshastighed, massetæthed, dynamisk viskositet og turbulens–diffusionskonstant
- elektrodegeometri, potentiale og rumladning i corona punktet
- ESP geometri, sektionslængde og antal sektioner
- maksimalt tilladelig støvlagstykkelse på udfældningspladen og støvets

massetæthed.

Computermodellen giver følgende ud–data for hele filterlængden:

- total virkningsgrad og masse–gennemtrængning
- rensningsgrad for hver partikelklasse
- middelstøvkoncentration og størrelsesfordeling for alle partikelklasser
- støvlagets tykkelsesvariation
- pladerystningstid
- gasstrømningsmønstre
- elektrisk– og rumladningsfelt
- middel strømtæthed
- strømtæthedsfordeling på udfældningspladen.

Virkningen af bulk–hastigheden og elektrode/udfældningsplade–afstanden på ESP'ens effektivitet og pris er blevet undersøgt. Model–resultaterne er i rimelig overensstemmelse med aktuelle data fra industrielle filtre, også selv om negative effekter som for eksempel re–entrainment og pladerystningstab ikke er blevet taget med i betragtning. Modelberegningerne viser også at nuværende filterkonstruktioner er tæt på det optimale, men at yderligere forbedringer stadig er mulige.

Contents

Figures and tables

Nomenclature

Latin symbols

A	Dummy Argument
A	Areal
$\underline{\underline{A}}$	Coefficient matrix
B	Dummy argument
b	Exponent factor
b	Mean mobility
b_e	Electron mobility
b_i	Ion mobility
b_p	Particle mobility
C	Dummy argument
C_a	Cunningham correction parameter
c_d	Cummulative–distribution function
ck	Particle to ionic space charge ratio
C_r	Charging rate coefficient
D	Dummy argument
d	Electrode–collector plate distance
D	Particle diffusion coefficient
D_i	Ionic diffusion coefficient
d_p	Particle diameter
d_{pg}	Geometric mean diameter of particle
d_{pj}	Arbitrary particle size (j–th class)
d_0	Particle mean diameter at the inlet of ESP
E	Mean electric field between the electrodes and collector plate
$\mathbf{E}$	Electric field
$\mathbf{E}_{dust}$	Electric field within dust layer
E_0	Electric field strength at corona point
$\boldsymbol{F}$	Electric force
F_e	Froude number
f_f	Electrical body force
$\boldsymbol{J}$	Current density
J_m	Mean current density
l	Turbulence length scale
l_x	Cell length in axial direction
l_y	Cell length in transversal direction
l_z	Cell length in vertical direction
m	Mass
$\dot{m}_{dust}$	Dust mass flux to collector plate
$\dot{m}_i$	Inlet mass flux
m_p	Particle mass
$\dot{m}_u$	Outlet dust mass flux
N	Number of grid points in y–directions
$\mathbf{n}$	Normal direction
n	Concentration
n_d	Exponent factor
n_0	Inlet concentration
p	Pressure
p	Penetration
q	Particle charge

q_s	Particle saturation charge
q_{sj}	Saturation charge of j–th particle class
$\mathbb{R}$	Resistivity
$\mathbb{R}_{dust}$	Dust resistivity
S	Concentration parameter in W_k theorem
S_{agg}	Agglomeration parameter
S_i	Inlet dust loading
S_0	Concentration at the inlet of ESP in W_k theorem
t	Time
u	Cartesian velocity component in axial direction
u_{slip}	Slip velocity at collector plate
u_τ	Friction velocity
U_0	Bulk velocity
v	Cartesian velocity component in transversal direction
v	Collision velocity of charge carriers
ve	Particle electric drift velocity
v_f	Gas (fluid) velocity
v_P	Particle velocity
w	Cartesian velocity component in vertical direction
W	Electrical drift velocity used in Deutsch models
W_b	Electrical drift velocity used in W_b theorem
W_{b-ref}	Electrical drift velocity used in W_{b-ref} theorem
W_k	Electrical drift velocity used in W_k theorem
W_0	Electrical drift velocity used in W_0 theorem
w_c	Weighting coefficient
x, y, z	Cartesian co–ordinates
x_i	Value of present iteration
x_i^0	Value from last iteration
y^+	Dimension less distance

Greek symbols

α	Slope coefficient
β	Slope coefficient
$\delta\rho_i$	Perturbed value of ionic space charge density
δE	Perturbed value of electric field
δJ	Perturbed value of current density
Δy, Δz	Distance between the grid points in x,y,z–direction
ϵ	Dissipation rate
ϵ_0	Vacuum permitivity
ϵ_r	Dielectric constant for particles
φ_0	Applied potential at the emission electrode
φ_w	Potential at collector plate
φ	Potential
φ_s	Corona start potential
γ	Frequency function
η	Efficiency
κ	Turbulence kinetic energy
λ	Collision mean free Path

μ	Gas kinematic viscosity
ν_τ	Turbulence diffusivity coefficient
ν	Molecular diffusivity coefficient
Ω_x, Ω_y, Ω_z	Electrical vorticity components in x,y,z–direction
ρ	Total space charge
ρ_P	Particle space charge
ρ_{Pj}	Space charge of j–th particle class
ρ_0	Onset space charge at corona point
ρ_c	constant total space charge
ρ_e	Space charge of electrons
ρ_s	Pseudo Space charge
ρ_N	Space charge density at collector plate
ρ_i	Ionic space charge
ρ_f	Gas (fluid) density
σ	Electric coductivity
σ_s	Variance or standard deviation
σ_g	Geometric standard deviation
τ_w	Shear force at wall
τ	resident time

Suffix

$(\underline{\underline{\ }})$	Matrix
$(\underline{\ })$	Vector
$\overline{(\ )}$	Mean value
$(\ )'$	Fluctuating part

1 Introduction

The particulate matter in industrial emission gases has been the main source of environmental pollution this century. Here, particles in submicron size in polluted air are particularly hazardous because they are inhaled and become absorbed in the lungs which may lead to serious diseases. Furthermore, particles in industrial emission gases can either be the main product of a certain process (like cement production) or they can be an undesirable byproduct in other connections (a 320 MW coal fired–power plant produces 15 tons precipitated ash every hour [49]). Therefore, it has been investigated in different possible ways how to remove the particulate matter in emission gases since the beginning of this century. In this connection, the electrostatic precipitators, ESP, and the mechanical processes have been the basic methods in removal processes.

The essential difference between the mechanical and the ESP processes is the form of removal forces. In mechanical processes particles are removed via inertial or mechanical forces while in the ESP process the removal forces stem from an adjustable external source in form of electrical body forces. The mechanical methods like gravity settling, centrifugal (like cyclone), filtration through screens, fabric bags and some agglomeration [31] have been successfully used in small precipitation scale. But, due to high energy consumption in the mechanical processes, it is continuously preferred to use ESPs as the main facility in control of industrial emission gases in large scale precipitation processes. Even finest particles in the submicron size range can be collected effectively by ESPs because of relatively large electrical body forces. Therefore, it is the propose of the present study to develop a general model for predicting and optimization of ESP processes supported by experimental data in laboratory scale.

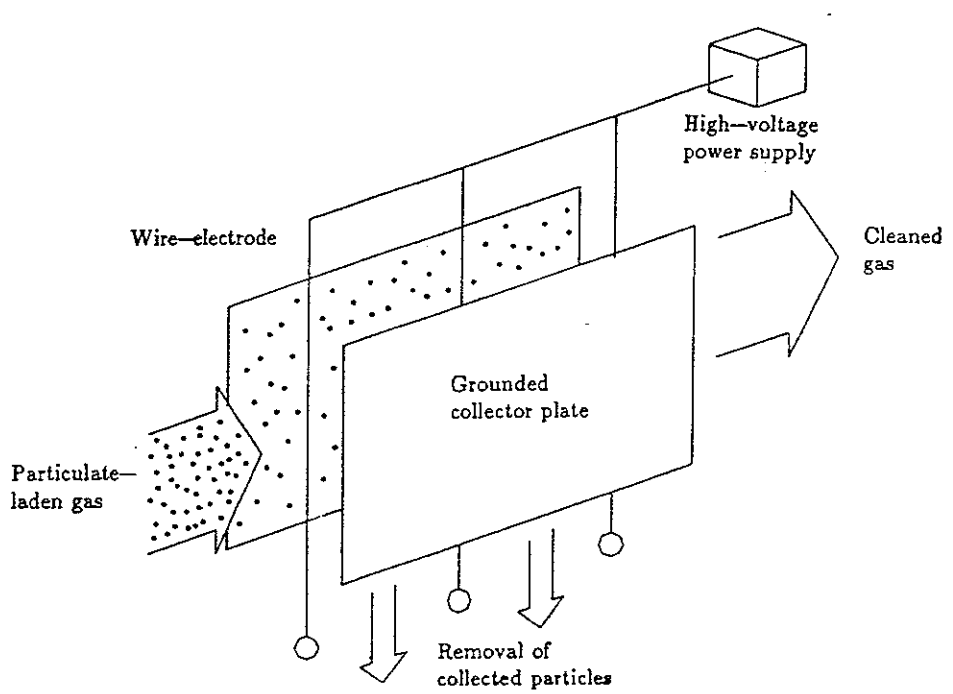

Fig. 1.1 Basic principle of a single–stage, wire–pale ESP.

1.1 ESP design

The most common design of an ESP consists of sectioned parallel plates separated by a distance of 0.2 to 0.5 meters with emission electrodes installed in between them, fig. 1.1. Gas with suspended particles flows horizontally between the plates with a velocity of 0.5 to 3 m/s. A sufficiently high imposed voltage on the electrodes induces ionized gas and free electrons in the space between the electrodes and grounded plates (collector plates). Particles in the flow get charged by free charges, migrate transversely to the flow direction and precipitate on the collector plates. The precipitated particles accumulate on the surface of the collector plates in form of a dust layer. The collected dust gathers in hoppers for disposal by rapping the collector plates periodically.

1.2 Areas of potential improvement of ESPs

The improvement of the ESP process has been investigated intensively since this removal method was presented for industrial world. Many researchers in the absence of computer power have tried to improve ESP's efficiency through empirical, and experimental investigations. But, in most of the cases there are no basic mathematical or physical evidence to explain the reasons for improvements or performance changes.

The complexity of the precipitation process is due to parameters such as three–dimensional electric field, flow patterns, variable boundary conditions, particle behavior, and the interaction between these mechanisms (the main precipitation mechanisms). In this connection, there has been a very few researchers who have tried to model the ESP problem through the derivation and the three dimensional solution of the governing equations simultaneously. The simultaneous solution of the governing equations makes it possible to take the interactions between the electric field, the flow field, and the particle concentration during precipitation process into account. For example, two dimensional numerical programs have been developed for simple ESP geometries (plate to plate and wire to plate) of laboratory scale by [6], [7], [8] and [10]. Such models solve the particle transport equation for monodisperse particles using an uniform flow field together with an analytic expression for calculation of the electric field. Furthermore, [35] has developed a calculating model for simple laboratory ESP which includes the influence of a prescribed three dimensional electric field and uses a prescribed flow field. This model assumes that the particle diffusion in axial direction is negligible and particles are monodisperse. However, in none of these numerical models the influence of the actual flow field or the interaction between the main precipitation mechanisms are taken into account. Therefore, the calculation results of these models disagree with the ESP data of complex geometries and dust loading parameters [53].

Non–ideal effects like particle re–enterainment, back corona, and sneakage (chap. 3 gives a short description over these parameters) show influence on the ESP process. In some cases, they represent the main part of adverse effects in precipitation process, and a basic investigation of these parameters from a physical point of view would effectively improve the prediction of the ESPs efficiency. However, before such effects are actual, one should have a reliable basic model for normal operating conditions.

We believe that the areas of potential improvement of ESP model will be found by taking the influence of the electric field, the flow field, the particle behavior, the non–ideal effects, and the interaction between these parameters during the precipitation process into account.

2 Basic theory and governing equations

The particle transport and precipitation process in ESP are governed by the gas flow and the imposed electric field. The electric field acts on ionized gas and charged particles in form of body forces mainly transversal to flow direction. These electrical body forces (Coulomb forces) make particles to move toward the collector plates and at the same time induce secondary flows if the electric field is strongly non–uniform of nature. The gas discharge and particle charging processes are governed by polarity of the electric field, electrode–collector geometrical configuration and the field strength [38].

Usually the precipitation process is expressed by an efficiency rate η, or a penetration rate, p which is the percentage of particles remaining after a certain length of the ESP. The relation between p and η is defined as

$$\eta = 1 - p \,, \tag{2.1}$$

and p is given by

$$p = n / n_0 \,, \tag{2.2}$$

where n_0 is the initial particle concentration at the inlet and n is the concentration in a certain section or place in the ESP. For instance n can be the concentration at the outlet, hence p and η will become the total penetration and efficiency of the whole ESP unit. The particle transport equation (conservation of mass) represents the governing equation to concentration variations in the steady state,

$$\nabla \cdot (n \mathbf{v}_p) = 0 \,, \tag{2.3}$$

where $\mathbf{v}_p$ is the particle velocity.

Physically, it can be assumed that particles in submicron size have the same velocity as the gas with no slip [46]. Hence we can write

$$\mathbf{v}_p = \mathbf{v}_f + \mathbf{v}_e \,, \tag{2.4}$$

where $\mathbf{v}_f$ is the gas (fluid) velocity and $\mathbf{v}_e$ is the drift velocity of the particles relative to the gas due to electrical body forces. $\mathbf{v}_e$ can be determined by establishing the balance between the electrical and viscous forces. After a few simplifications due to other minor forces [46], the following equation can be derived

$$m \frac{d\mathbf{v}_e}{dt} = -3\pi \, d_p \, \mu \, \mathbf{v}_e + q \, \mathbf{E} \,. \tag{2.5}$$

In this equation, m is the particle mass, μ is the gas viscosity, d_p is the particle diameter, q is the particle charge and E i the electric field strength. The solution to Eq.(2.5) is

$$\mathbf{v}_e = \frac{qE}{3\pi \cdot d_p \cdot \mu} \left[1 - \exp{-(\frac{3\pi \cdot d_p \cdot \mu}{m})t} \right] . \tag{2.6}$$

The ratio $\frac{6\pi \cdot d_p \cdot \mu}{m}$ for particles ($d_p \leq 10$ μm) is of the order 10^3, therefore the exponential term becomes negligible over a time scale of a few milliseconds and it can be

assumed that $\mathbf{v}_e$ is proportional to $\mathbf{E}$ and q i.e.

$$\mathbf{v}_e = \frac{q\mathbf{E}}{3\pi \cdot d_p \cdot \mu} . \tag{2.7}$$

The ratio $\frac{q}{3\pi \cdot d_p \cdot \mu}$ is called the particle mobility, b_p so

$$\mathbf{v}_e = b_p \mathbf{E} . \tag{2.8}$$

The flow pattern $\mathbf{v}_f$, is governed by inertia forces, body forces and the boundary conditions. Navier–stockes equations describe the flow motions due to these forces in following form

$$\nabla \cdot (\rho_f \mathbf{v}_f) = 0 , \tag{2.9}$$

$$\rho_f \mathbf{v}_f \nabla \mathbf{v}_f = -\nabla p + \mu \nabla^2 \mathbf{v}_f + \mathbf{f}_e , \tag{2.10}$$

where ρ_f is the fluid density, p is the pressure, and $\mathbf{f}_e$ is the electrical body force. In these equations, it is assumed that the gravitational and buoyancy forces are negligible compared to electrical forces and that the flow is steady.

The electrical body force arises when the electric field strength acts on charged gas ions or charged particles. Having an electric field requires a potential difference between two electrodes in the operating system (in our case the electrodes are the wires and the collector plates).

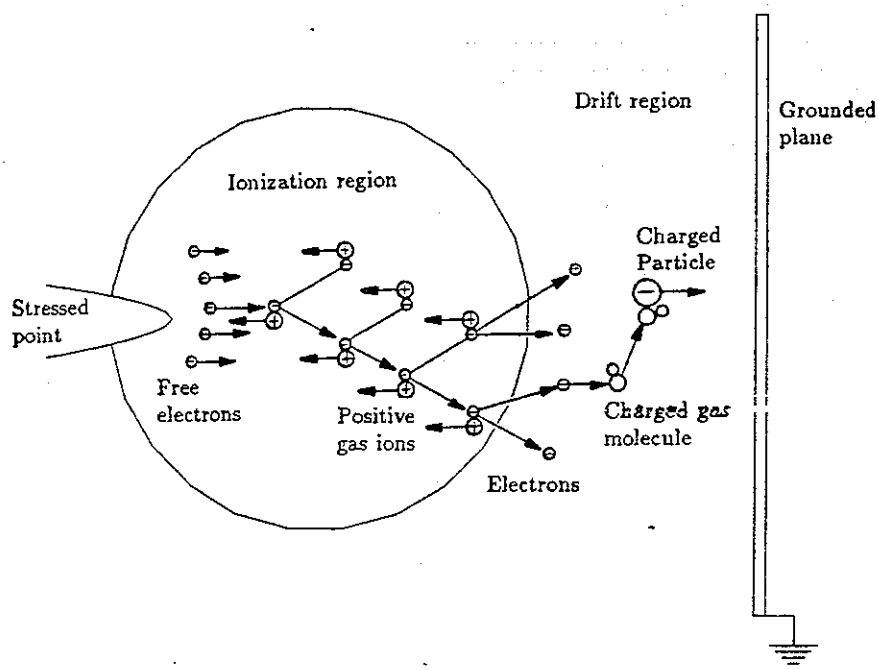

Fig. 2.1 Illustration of the negative corona discharge process (and the particle charging), from [36].

Particle and space charging due to corona discharge are the complicated mechanism, which are not clarified entirely yet. Figure 2.1 illustrates the negative corona discharge for point to plate gap. Simple theories describe the gas ionization and the particle charging by following words: a discharge point (corona point) produces free electrons in the space around itself (ionization region). Corona starts at a certain potential–voltage between the corona point and the grounded plate. Free electrons gain kinetic energy – from the intense electric field at the point – large enough to ionize the gas through impact and thereby initiate avalanches. The avalanches develop in a direction away from the point out to that distance where the electron attachment equals the gas ionization. The electrons generated by the ionization are injected into the drift region, where they attach to the large molecules producing a space charge, [38] and [36]. The charged gas molecules impact the suspended particles and attach their electrons to them.

The governing equations for the electrical conditions with the assumption of a linear isentropic medium and neglecting the magnetic effects, reduce to the quasi–static electrodynamic equations [36]. These are represented by the Poisson equation for the potential field and the continuity equation for space charge transport in the following conservative form

$$\nabla\cdot(-\nabla\varphi) - \frac{\rho}{\epsilon_0} = 0 \,, \tag{2.11}$$

$$\nabla\cdot(-b\rho\,\nabla\varphi) = 0 \,, \tag{2.12}$$

where φ is the potential, ρ represents the space charge, and b is the gas mobility. Eq.(2.11) is elliptic, while Eq.(2.12) is 1.order hyperbolic. Furthermore, the electric field strength, $\mathbf{E}$ has been defined as

$$\mathbf{E} = -\nabla\varphi \,, \tag{2.13}$$

and the electrical body force acting on the gas phase in Eq.(2.10) is the product of electric field strength, $\mathbf{E}$ and space charge, ρ,

$$\mathbf{f}_e = \rho\mathbf{E} \,. \tag{2.14}$$

The foregoing equations for electric fields of potential and charge, as well as velocity field of the gas and the concentration field of particles, are subject to boundary conditions to be discussed later.

3 Introduction to parameters influencing the precipitation rate

This section gives a short description of parameters influencing the precipitation process. The precipitation process is influenced by flow, electric field and particles as it was presented in the foregoing chapters. In this connection table 1 is arranged to show the influencing parameters classified under their main physical property. Most of the parameters in table 3.1 can be found in the previously derived governing equations. But those parameters which do not appear in these equations may either have influence on the boundary conditions or they are found through empirical methods in order to express the integral effects.

3.1 Flow

We begin at the top of table 3.1.

– u, v and w are cartesian components of the gas velocity, v_f.

– ν_T is the turbulence diffusivity coefficient, which can be calculated by employing the κ–ϵ model, the algebraic model or can be assumed constant.

– The flow boundary conditions can be laminar or turbulent. In order to catch the velocity gradients near the boundary, one may either construct a very fine grid in this region, or employ a boundary–freestream decoupling model like the logarithmic law (wall function), in order to reduce the number of grid points.

3.2 Electric field

– The electric field calculation can be performed by taking the influence of space charge into account or by assuming that the space charge variations have no influence on the electric field, and may be ignored. Doing the calculations regardless of the space charge variations (or assuming a guessed spatial variation of space charge in the calculation domain) makes the calculations very easy. However, such approaches are not accurate, since the coupled system of equations should be solved simultaneously for both the electric field and ionic space charge transport.

– The potential at the electrode and collector plate surface varies due to dust layer buildup. These variations can be included in a predicting model by assuming a known potential value per unit thickness of ash layer.

– The pulse energization makes it possible to impose a higher potential on the system, in order to get a stronger electrical drift velocity toward the collector plates. Beside this, the pulse energization increases the ionic (see chap. 6) diffusion which makes it possible to have a more uniform distributed current density at the collector plate, causing a better collection efficiency in this regions.

– The spark over phenomenon occurs at a certain potential between the electrodes and the collector plates. This phenomenon depends on geometry, polarity of energization, temperature, ash resistivity, gas composition and humidity.

3.3 Particles

– Particle charge can be determined theoretically for spherical particles. But, there is no mathematical formula to describe the particle charge for none–spherical particles, therefore experimental methods should be employed to determine the particle charge.

– $W_{Deutsch}$ is the particle drift velocity in Deutsch's one dimensional ESP model. W_b, W_k and W_0 are empirical determined effective particle drift velocity in the models developed by F.L.Smidth company [49], Flakt [48] and Dr.C. Allander [30].

– The gaussian function gives the distribution probability of the particle size. The particle size can be defined either by employing of the mean particle size or by dividing the particles into a certain number of classes in order to be able to calculate the influence of particle size variations in the precipitation process.

– The Cunningham constant C_a is used as a correction parameter for electrical drift velocity [11].

– The sneakage is used as a correction parameter for particle by–pass of the system [11].

– The re–entrainment correction factor accounts for the effect of collected particles at the collector plate falling off and entering the bulk flow. The re–entrainment at the first stage occurs when:
1) the collector plate is rapped in order to collect the precipitated dust in the hoppers.
2) the boundary layer near the ash surface is disturbed by high flow gradients (high turbulence). In this mechanism the aerodynamical inertia forces overcome the electrical body forces at the dust surface layer and release the particles from the surface of the collected dust.
3) the back corona phenomena occurs.
4) particles with relatively high velocity collides the surface of the dust layer and releases the precipitated dust from the surface. This form of re–entrainment occurs under the normal precipitating conditions [53]. The re–entrainment of particles under normal conditions can be modeled by introducing an accumulation parameter in the particle transport equation, Eq.(2.3). This parameter governs the balance of particle transport in the accumulation region near the collecting wall, i.e. the boundary conditions will be changed at the collector plate.

– The "back corona" phenomenon occurs mostly when dealing with high resistive dust. When high resistive dust builds up at the collector plates, it will reduce the electron current to the metallic surface of the plate causing an accumulation of charges within the dust layer and repelling the particles back into the bulk flow. At the same time those particles which have already been precipitated will be forced to detach from the dust layer surface and enter into the bulk flow as well.

– The agglomeration occurs when the suspended particles in submicron size attach together and form bigger particles. The agglomeration depends on the particle surface, particle charge and the surrounding media. The agglomerated particles with higher migration velocity [32] are easier to precipitate, therefore it is always of interest to put the agglomeration process forward in order to improve the efficiency of ESP. The agglomeration of particles in the system is theoretically equivalent to introducing a

source term in the right hand side of the particle transport equation,

$$\nabla\cdot(n\mathbf{v}_p) = S_{agg}\,. \tag{3.1}$$

– The dust electrical resistivity depends on chemical composition, temperature and the humidity. The dust resistivity is usually measured in dry state at a drift temperature between 50 to 400 C^0 [53].

– The parameter D represents the particle diffusion rate in a media. D is modeled the same way as the turbulence diffusivity of momentum (the eddy diffusivity), ν_T [10].

A simple way to model the particle diffusion coefficient is to assume, that D is constant in the whole calculation domain. It has been observed, that this assumption leads to poor results near the boundary. It may therefore be necessary to model the particle diffusivity variations near the boundary [6].

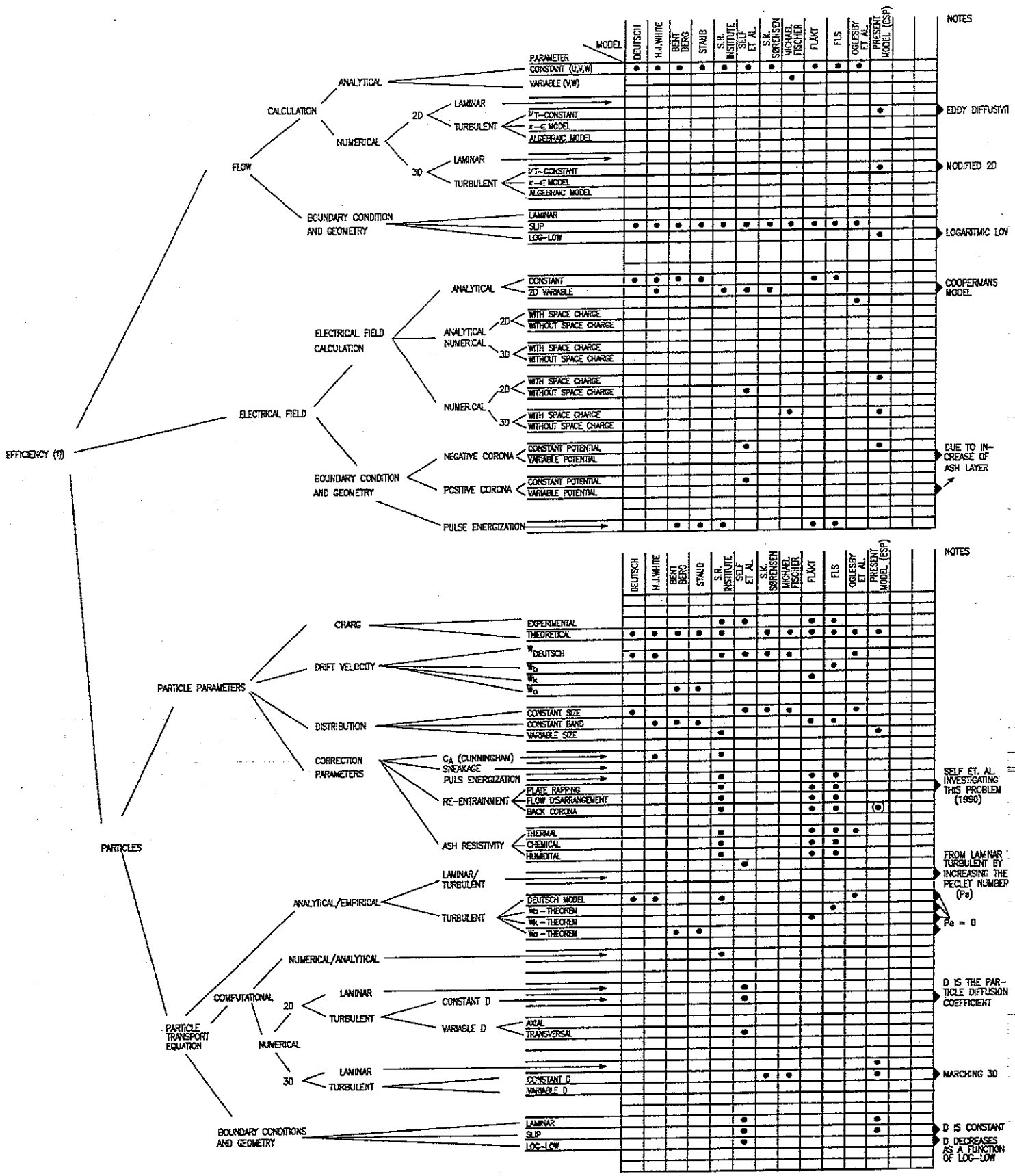

Table 3.1 Summary of parameters influencing the efficiency of different ESP calculation models. The dots indicate the influencing parameters used in a certain ESP model.

4 Previous work

This part describes the basic ideas behind a few predicting models, whose solution methods will be representative for most of the other models.

It begins with the first ESP model developed by Deutsch in the beginning of this century. Deutsch's model is strongly idealized due to physical facts governing the precipitation process. This model is not only idealized but it makes drastic assumptions, namely, turbulent mixing is so strong that a uniform particle concentration profile is maintained transverse to the collector plates [8], particles are monodisperse, flow is one dimensional and the electrical field is uniform transversal to the flow direction [35]. These assumptions simplify the transport equation, Eq.(2.3), to a first order linear differential equation in following form

$$U_0 \frac{dn}{dx} + n \frac{W}{l_y} = 0 \,, \tag{4.1}$$

where U_0 represents a constant bulk velocity, W is the drift velocity, n is the particle concentration and l_y is the distance between the electrodes and the collector plates. Solution to Eq.(4.1) is an exponential decay of the concentration in the axial direction, x, given by

$$n = n_0 \left[1 - \exp\left(-\frac{W}{U_0 l_y} x\right) \right] \,, \tag{4.2}$$

where n_0 is the initial concentration at the inlet. Inserting this equation into Eq.(2.2) and Eq.(2.1), respectively, gives

$$\eta = 1 - \exp\left(-\frac{W}{U_0 l_y} x\right) \,. \tag{4.3}$$

Equation (4.3) is the expression for the ESP's efficiency suggested by Deutsch in 1922. It should be mentioned that this equation, with some empirical modifications, has been used as the basic tool in ESP design since it was presented by Deutsch.

White [31] used Deutsch equation as a predicting model and at the same time he tried to optimize the parameters influencing the precipitation process through simple mathematical considerations and experiments.

In fact the Deutsch equation can always be fitted to a certain kind of ESP by introducing some proper adjusting coefficients in the exponential term. For instance, this is actually the method that Southern Research Institute [32] has used in developing their predicting model (we will call it "semi empirical model"). The main feature of this model is to divide the ESP into some minor increments, in order to decrease the error due to application of calculated and empirical integrated adjusting coefficients. For example, one of the important calculated coefficients stems from a two dimensional electric field calculation for positive corona discharge (here the model assumes that positive corona discharge has the same characteristic as negative corona discharge). The empirical coefficients stand for the adjustment of: flow quality due to turbulence level, geometrical configuration, dust layer thickness, electrode types, plate rapping methods, particle distribution, dust resistivity, sneakage, dust re-entrainment, current voltage characteristic and ash density. Later this type of model was further improved by Lawless from Research Triangle Institute [52,53], who introduced further empirical adjusting parameters in the Deutsch equation.

Now let us look at some "fully empirical models". The main feature in these models is to employ the data from an already existing ESP in the Deutsch model in order to achieve an effective value for the drift velocity in a certain precipitation process. Then, later on this value will be used as the main parameter in dimensioning of other ESPs with same characteristics.

These models employ the statistical relation between the particle loading and the drift velocity in order to cover a wide range of particle loading in an ESP process. These statistical relations were first presented by Dr. C. Allander [30] in the following form

$$W = \left[\frac{d_p}{d_0}\right]^{n_d} W_0 , \tag{4.4}$$

where W_o is the drift velocity for particles with diameter d_0 and n_d is an empirically fund constant ($n_d \approx 0.5$). Later, this relationship changed to a relation between the particle loading and the drift velocity by Flakt [48] in the following form

$$W_k = \left[\frac{S}{S_0}\right]^{0.2} W_0 , \tag{4.5}$$

where W_0 is the drift velocity corresponding to the particle loading S_0, and W_k is the effective drift velocity corresponding to the particle loading S. Flakt has used this model in their ESP design and it is called the W_k–theorem. It should be mentioned that particle loading S is the same as concentration n.

Another ESP model, with the same idea as the W_k–theorem, has been developed by F.L.Smidth Company [49]. This model presents Eq.(4.5) in following form

$$W = \left[\frac{n}{n_0}\right]^{b} W_0 , \tag{4.6}$$

where b is an empirically fund constant ($b = 0.22$ for cement). Inserting W from Eq.(4.6) into Eq.(4.1) results in

$$U_0 \frac{dn}{dx} + n \left[\frac{n}{n_0}\right]^{b} \frac{W_0}{l_y} = 0 . \tag{4.7}$$

Using the term W_b for W_0, the solution of Eq.(4.7) becomes

$$W_b = \frac{U_0 l_y}{l_x} \frac{1}{b} \left[\frac{1}{(1-\eta)^b} - 1\right] , \tag{4.8}$$

where η represents the $(1-\frac{n}{n_0})$ term.

Now, for a given η and n_0 we can find W_b. Using Eq.(4.8) leads to a value for W the so called W_{b-ref}. Hereby W_{b-ref} can be used as the basic tool in dimensioning of the other ESPs with the same characteristics.

As it can be seen, the forgoing models use empiricism, as the fundamental tool in prediction of the ESP efficiency. Therefore in general, they will not be expected to predict the performance of other precipitators with significant difference in operating parameters.

The last model to be mentioned is developed by Self et al, [1]–[10], [37], [41],[51]. This model presents a further development of the transport equation, Eq.(2.3), due to modeling of the particle turbulence diffusion. In this model particle diffusion mixing is modeled by introducing the instaneous velocity and concentration terms in form of their mean and fluctuating values,

$$\mathbf{v}_p = \bar{\mathbf{v}}_p + \mathbf{v}_p' \,, \tag{4.9}$$

$$n = \bar{n} + n' \,, \tag{4.10}$$

in transport equation Eq.(2.3),

$$\nabla\cdot(n\mathbf{v}_p) = \nabla\cdot[(\bar{\mathbf{v}}_p + \mathbf{v}_p')(\bar{n} + n')] \,,$$

which after averaging becomes

$$\nabla\cdot(n\mathbf{v}_p) = \nabla\cdot(\bar{\mathbf{v}}_p\bar{n}) + \nabla\cdot(\overline{\mathbf{v}_p' n'}) = 0 \,. \tag{4.11}$$

Using Fick's law analogy on the fluctuating term leads to

$$\overline{\mathbf{v}_p' n'} = -D\,\nabla n \,, \tag{4.12}$$

where D is the turbulence diffusivity coefficient of particles.

Inserting Eq.(4.12) into Eq.(4.11) and assuming D as a constant will lead to the particle convection–diffusion equation [10],

$$\nabla\cdot(n\mathbf{v}_p) - D\,\nabla^2 n = 0 \,. \tag{4.13}$$

This equation has been solved in two dimensions (axial–transversal) by [10] for positive corona discharge with D and $\mathbf{v}_p$ as constant parameters. The results agree very well with the experimental laboratory data. For the case of negative corona discharge, Eq.(4.13) with D and $\mathbf{v}_p$ as constants do not show comparable results with experiments due to velocity fluctuations, recirculating patterns and strong gradients in the flow. It should be mentioned that the reason for the poor results in this case is due to the nature of negative corona discharge which induces strong electrical vorticity fields [50] and a high level of turbulence in the flow, while in the case with positive corona discharge velocity gradients are weak and turbulence level is low. Kihm [41] recommends to take the flow influence into account in order to achieve closer results to the physical performance of the ESP. This recommendation will be in focus in our further experimental and computational investigations.
Furthermore, it is recommended [52] to investigate the positive corona discharge energization due to its nature of a more uniform electric field and it's low level of turbulence. The positive corona discharge will be investigated in the electric field calculations in chap. 6.

Fischer [35] solved Eq.(4.13) for three–dimensional parabolic case ($D = 0$ in axial direction), with the nonuniform electrical field calculated by Sørensen [36]. He has used his program to investigate the effect of uniform as well as nonuniform electric fields together with a pseudo velocity field on the efficiency. His ESP model does not contain the effect of the real flow pattern, particle size or interacting condition changes.

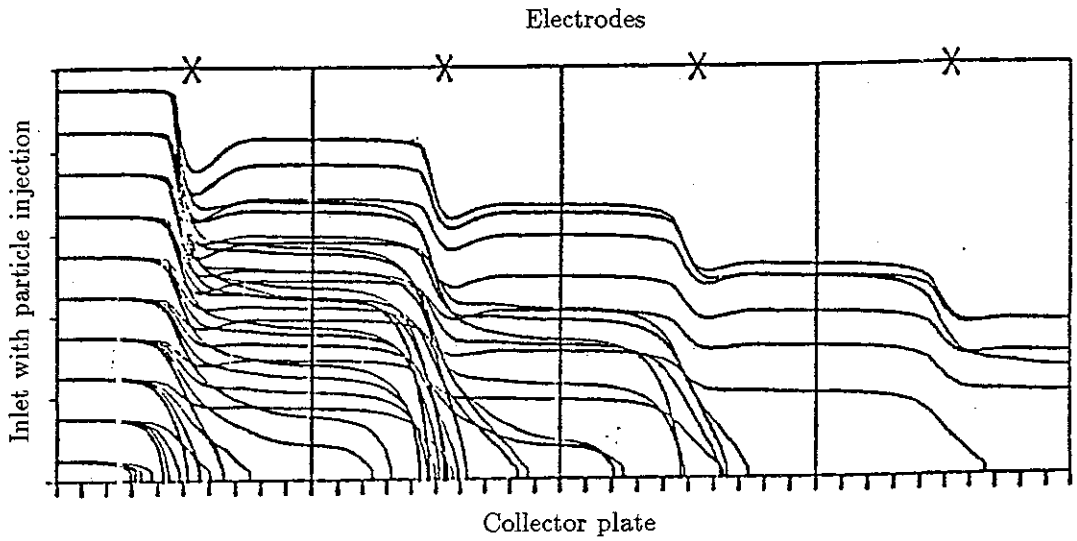

Fig. 5.1 Particle trajectories for different particle size, from [46].

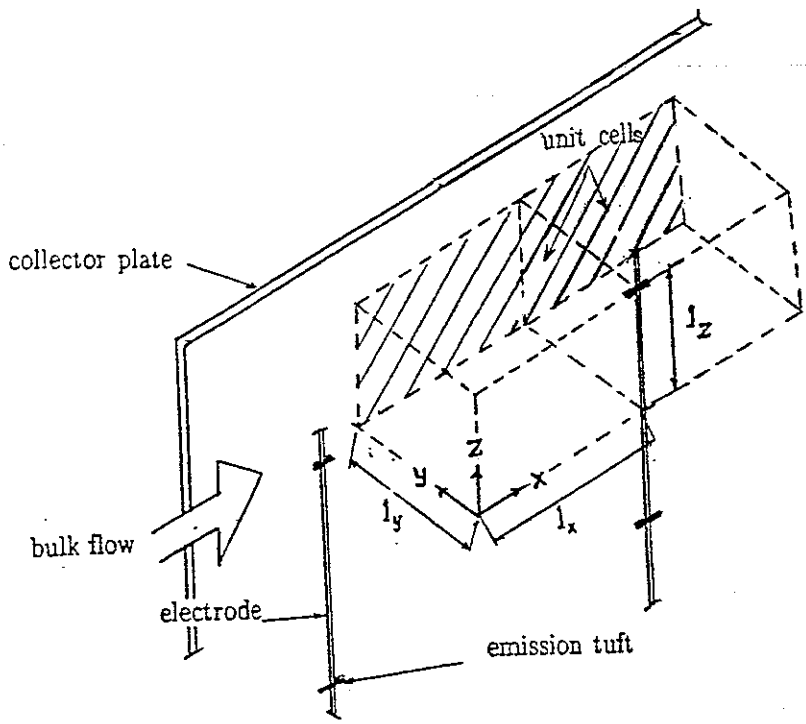

Fig. 5.2 Illustration of symmetrical calculation cells in negative tuft corona ESP.

5 Proposed model

As we saw from the previous work done by different researchers and companies, it will be quite reasonable to improve the models developed by Self et al due to its capability in prediction and optimization of the ESP process in general.

The electrical forces are the main mechanism in the precipitation process. These forces acts on ionized gas and charged particles in form of electrical body forces and Coulomb forces, respectively. Particles under the effect of Coulomb forces migrate toward the collector plate and accumulate in form of dust layer at the plate. The dust layer is kept at the collector by the electrical body forces until the plate is rapped. Furthermore, the ionized gas under the influence of the non–uniform spatial electric field creates recirculating or deformed flow fields between the electrodes and the collector plates. Therefore, it is necessary to solve the governing equations for three–dimensional electric field conditions inside the ESPs of complex geometries.

As we mentioned, the flow field inside the ESP is influenced by the electrical field and the geometrical configurations. The transport of submicron particles is affected by the flow patterns within the electrodes and the collector plates, therefore it is necessary to calculate the flow field inside the ESP. One of the main parts in ESP modeling will be the calculations of the flow field along the ESP.

Particles influence the electrical field, flow field, electrical migration velocity, gas discharge, particle charge and so forth. The variation in particle concentration throughout the ESP changes the forgoing parameters, therefore we will further aim at approaching the physics of commercial ESPs by taking these condition changes, during the precipitation process, into account.

Furthermore, as we discussed in foregoing chap. 2, particles with different size have different migration velocity (see Eq.(2.7)), therefore they will be collected at different places in the ESP, fig. 5.1. In order to model these variations in the particle transport equation, the particles can be divided into a certain number of particle classes. In each class the mean particle size is the representative of particle size in that class. Thereby, the particle transport equation will be solved for each particle class separately and the results will be added together using a weighting function which represents the percentage of the particles in each class.

Since the calculations will be performed for an ESP under the normal operating conditions, the influence of the dust layer resistivity, back corona, agglomeration, and particle re–entrainment will not be included in the calculations. Table 3.1 shows the influencing parameters in the present model.

5.1 Calculation domain

The geometrical configuration of the ESP shows that it is possible to divide the ESP unit into small symmetrical calculation volumes (cells), see fig. 5.2. Since the particle concentration profile is considered to be uniform at the inlet of the ESP, we assume that the precipitation process is identical within each symmetrical cell in vertical direction. It will therefore be sufficient to calculate the efficiency variations in the axially aligned cells. There, we will use a marching solution strategy, which solves the governing equations completely for one symmetrical cell and transfers the results to the next calculation cell. This solution method is explained in details in section 8.4.

6 Electrodynamic of ESP

6.1 Introduction

The efficiency of an ESP is affected by the electrodynamic field, the flow field and the particle concentration field. Of these, the electrical body forces on the particles are the main mechanism in the precipitation processes. Therefore it is important to begin with modeling the electrical conditions in the ESP. The electrical conditions are influenced by geometrical configurations, ionic space charge, electric field and particles. The present chapter deals with theoretical considerations for analytical and numerical calculations of electrical conditions in commercial ESPs.

6.2 Basic governing equations

Maxwell equations for the electromagnetic fields are used to describe the electrical conditions of unipolar corona space charge flow. These equations are valid for all kind of media taking the contribution of electric field, electric induction, magnetic field, magnetic induction, current density and space charge density into account [36]. The magnetic effects are ignorable in relation to the very intense electric field, since the dynamic current is so small in the case of corona discharge. With this assumption the governing equations may be summarized to classical quasi–static electrodynamic equations for the electric field,

$$\nabla \times \mathbf{E} = 0 \,, \tag{6.1}$$

$$\nabla \cdot \mathbf{E} = \frac{\rho}{\epsilon_0} \,, \tag{6.2}$$

and the current density field,

$$\nabla \cdot J = 0 \,, \tag{6.3}$$

where $\mathbf{E}$ is the electric field, J is current density, ρ is total space charge and ϵ_0 is the vacuum permitivity. Equation (6.1) expresses the irrotational nature of the electric field, therefore the $\mathbf{E}$ field may be represented by the gradient of a scalar potential field, φ as

$$\mathbf{E} = -\nabla\varphi \,. \tag{6.4}$$

Inserting this equation into Eq.(6.2) gives the equation for potential field,

$$\nabla^2\varphi = -\frac{\rho}{\epsilon_0} \,. \tag{6.5}$$

Furthermore, the current density may be expressed as the product of the electric conductivity, σ and the electric field $\mathbf{E}$,

$$J = \sigma\,\mathbf{E} \,. \tag{6.6}$$

σ is assumed to vary proportional to the space charge due to considerable variations in the space charge density. So, the electrical conductivity may be expressed as

$$\sigma = b\rho \,, \tag{6.7}$$

where b is the constant mobility of the medium. Inserting Eq.(6.7) and Eq.(6.6) into Eq.(6.3) the result will be

$$\nabla \cdot (b\rho\, \mathbf{E}) = 0 \,. \tag{6.8}$$

Equation (6.8) and Eq.(6.5) are the basic equations in our further considerations.

Equation (6.5) expresses the distribution of the potential field influenced by the boundary conditions and the space charge in the entire region. This is the well known Poisson (boundary value problem) equation with an elliptical and a fully diffusive nature in the solution, while Eq.(6.8) expresses the convection of space charge (initial value problem) in the direction of the electric field, E.

Equation (6.8) in the present representation has a hyperbolic nature in solution. This means that the solution depends on the characteristic [57] lines for the transporting field (E field in our case). These Characteristic lines are the trajectories (transporting direction) for the gas ions (ρ field). Therefore the solution significantly depends on the representation of these characteristic lines. Furthermore, these characteristic line orientations highly depend on the numerical representation of the grid lines, and the solution may not be unique, since the grid lines can be represented in many different forms.

In our further discussion we will present a new method to make it possible to solve Eq.(6.8) in a parabolic way, where the solution would not depend on the characteristic lines of the electric field. Therefore it will be much easier to obtain a unique solution with fewer numerical algorithms and higher accuracy. The description of the method is as follows:
for b = constant Eq.(6.8) becomes

$$\mathbf{E}\cdot\nabla\rho + \rho\, \nabla\cdot\mathbf{E} = 0 \tag{6.9}$$

In Eq.(6.9), the divergence of the electric field is replaced by the term, ρ/ϵ_0 from Eq.(6.9) ,so

$$\mathbf{E}\cdot\nabla\rho + \rho\,(\frac{\rho}{\epsilon_0}) = 0 \,. \tag{6.10}$$

In this equation the first term expresses the continuity of space charge in the entire domain while the second term is a source production term. The second term may be linearized by assuming ρ outside the parentheses as a constant, ρ_c,

$$\rho\,(\frac{\rho}{\epsilon_0}) = \rho_c(\frac{\rho}{\epsilon_0}) \,. \tag{6.11}$$

Then Eq.(6.10) becomes

$$\mathbf{E}\cdot\nabla\rho + \rho_c(\frac{\rho}{\epsilon_0}) = 0 \,. \tag{6.12}$$

As it can be concluded from Eq.(6.5), the term ρ/ϵ_0 equals the fully diffusive Laplacian term for potential distribution. This means that the variable, ρ/ϵ_0 will act as a diffusive source term in Eq.(6.12). Therefore Eq.(6.12) compared to Eq.(6.8) has a parabolic convective–diffusive nature in its solution. Actually this is the main concept behind the solution of the ionic transport equation in a parabolic way.

It should be mentioned that in the numerical solution procedure ρ_c adapts the old value of the space charge from the last iteration. This will be discussed later in section 6.4.

The total space charge, ρ in the physical domain receives contribution from the space charge of free electrons, the ionic space charge and the space charge due to presence of charged particles in the gas,

$$\rho = \rho_i + \rho_e + \rho_p, \tag{6.13}$$

and similar by

$$J = (b_i\rho_i + b_e\rho_e + b_p\rho_p)\,\mathbf{E}\,, \tag{6.14}$$

where the indexes $_i$, $_e$ and $_p$ on ρ and b stand for ionic, electron and particle.

For typical operational conditions the contribution from the free electrons is negligible [36]. Taking the contribution of particles into account, then Eq.(6.2)and Eq.(6.12) change to

$$\nabla^2\varphi = -\frac{\rho_i+\rho_p}{\epsilon_0}\,, \tag{6.15}$$

$$\nabla\cdot\left[(b_i\rho_i + b_p\rho_p)\,\mathbf{E}\right] = 0\,. \tag{6.16}$$

In order to make the numerical computation of Eq.(6.16) less time consuming the following mathematical procedures will be performed: first we define the ratio

$$ck = \frac{b_p}{b_i}\,.$$

So, Eq.(6.16) can be written as

$$\nabla\cdot\left[(\rho_i + ck\,\rho_p)\,\mathbf{E}\right] = 0\,. \tag{6.17}$$

Furthermore, if we assume a pseudo space charge, ρ_s defined as

$$\rho_s = \rho_i + ck\,\rho_p, \tag{6.18}$$

then Eq.(6.17) may be written as

$$\nabla\cdot(\rho_s\mathbf{E}) = 0, \tag{6.19}$$

which is equivalent to Eq.(6.8).
Like before, this equation may be changed to the convective–diffusive parabolic form as,

$$\mathbf{E}\,\nabla\rho_s + (\rho_i + \rho_p)\,\frac{\rho_s}{\epsilon_0} = 0, \tag{6.20}$$

where the term $(\rho_i + \rho_p)$ is equivalent to ρ_c.
It should be mentioned that the amount of ρ_i will be calculated as $\rho_i = \rho_s - ck\,\rho_p$ after each iteration in the numerical calculation procedure.

6.3 Boundary conditions

The boundary conditions for the potential field, the electric field and the space charge distribution depend on the geometrical configuration, the applied potential voltage on emission electrode, the particle charge contribution, the specified potential on collector plate due to resistivity of the precipitated ash on the collector plate and the corona emission of the electrode.

Following boundary conditions are employed in order to transfer the foregoing physical information into the governing equations:

(6.21) $\frac{\partial \varphi}{\partial n} = 0$ at all the symmetry planes,

(6.22) $\varphi = \varphi_0$ at the electrode,

(6.23) $\varphi = \varphi_{\text{wall}}$ at the collector plate,

(6.24) $\frac{\partial \rho}{\partial n} = 0$ at all the symmetry planes inclusive the collector plate,

(6.25) $\rho = \rho_0$ at the corona point,

(6.26) $\mathbf{E} = -\nabla\varphi$ at all the points,

where ρ_0 and φ_0 are the onset space charge and the potential voltage respectively at the corona point.

6.3.1) Boundary conditions approximations

Since there is no simple model to describe the corona discharge process physically and mathematically, we have to find the amount of induced space charge at the corona point empirically. But before this we must try to have a better understanding of the boundary conditions and the electric field at the corona point. As described in the foregoing section, the corona discharge depends on the geometrical configuration and the electric field strength in this region. The corona region has a tendency to be displaced a small distance from the electrode where the critical electric field may be applied. The experimental observations show the corona region displacement is around one millimeter from the electrode surface [36]. The electrical conditions in this region are very complex and must be treated from a microscopic point of view. Therefore in our further consideration the corona discharge region will be concentrated at a source point on the discharge electrode and the amount of space charge emitted from this point will be found empirically using the measured current density at the collector plate. The numerical procedure for determination of the amount of space charge at the corona point will be described in section 6.4.3.

6.3.2) Ion and particle mobility

The mobility of the ions is affected by the humidity of the gas. Lawless et al [61] has measured the influence of water vapour on the ion mobility shown in fig. 6.1. The measurements indicate a strong change in mobility (about 18%) in the range

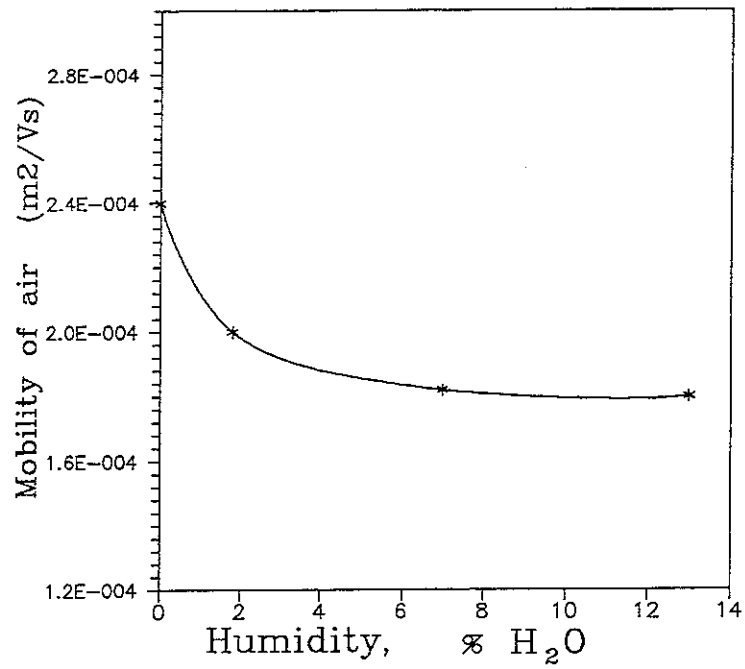

Fig. 6.1 Influence of H_2O Vapour in air on the mobility of ions in air, from [62].

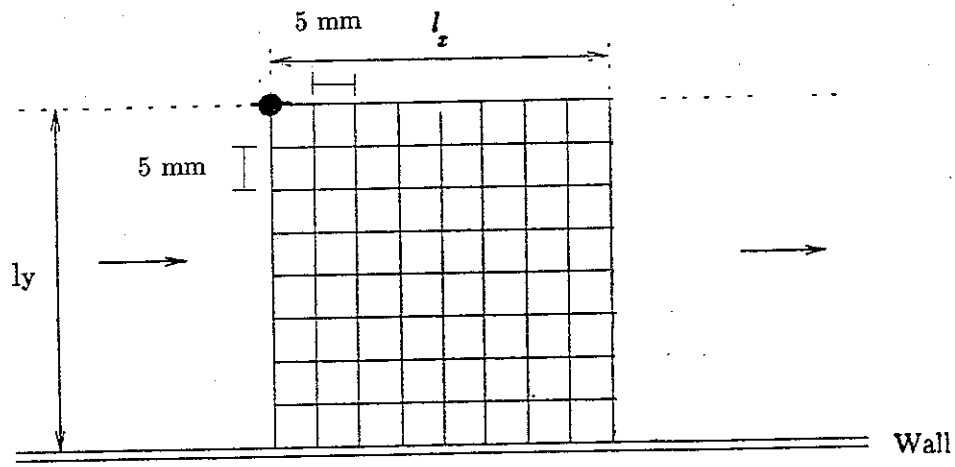

Fig. 6.2 Grid arrangement of numerical calculations in x,y—plane.

0%–1.8% H_2O vapour. However this has not been taken into account in our model, therefore we shall notice a discrepancy between the measured and the calculated properties involving the mobility of gas ions.

The particle mobility is discussed in chapter 2. Particles with a drift velocity of 0.05–0.2 m/s under the effect of a 240 kV/m electric field will have mobilities of 2.1–8.3 × 10^{-7} m^2/Vs.

6.4 Numerical solution method

6.4.1) Grid generation

The numerical calculations are performed on an equidistant constant grid for all the cases, fig. 6.2. The distance between the grid points is 5 mm in x, y and z directions. This means for instance, that a calculation domain of $(l_x,l_y,l_z) = (50,150,50)$ mm will be divided into 11 × 31 × 11 grid points.

6.4.2) Discretization method

The discretization of Eq.(6.15) and Eq.(6.20) for the two dimensional case is shown in appendix A. As mentioned before Eq.(6.15) is the well known Poisson equation with elliptical nature in solution. Therefore the central difference scheme is used in discretization of this equation. In order to model the parabolic nature of the ionic transport equation the first–order upwinding scheme is employed to discretisize Eq.(6.20).

6.4.3) Discretization of boundary conditions

As mentioned before the slope of space charge distribution in y–direction at the collector plate ,Eq.(6.24) equals zero, so the value of ρ_N at the collector plate will depend on ρ_{N-1} and ρ_{N-2} assuming a parabolic distribution, fig. 6.3. Hence, a second order backward difference is employed to fulfill this condition in the following form

$$\rho_N = \frac{4\ \rho_{N-1} - \rho_{N-2}}{3}. \tag{6.27}$$

As mentioned before there is no known physical applicable model describing the corona discharge process. Therefore in our model the corona process and the discharge conditions will be considered as a "black box". From a numerical point of view the interpretation is that the value of the space charge at the corona point concentrates to a source point. By using this approximation, the only thing we must know is the amount of space charge at this point.

The current density of ions from the discharge point toward the collector plate can be measured at the collector plate experimentally. Therefore in the numerical procedure, the amount of space charge at the corona discharge point is adjusted in such a way, that the computed current density at the collector plate becomes equal to the measured value.

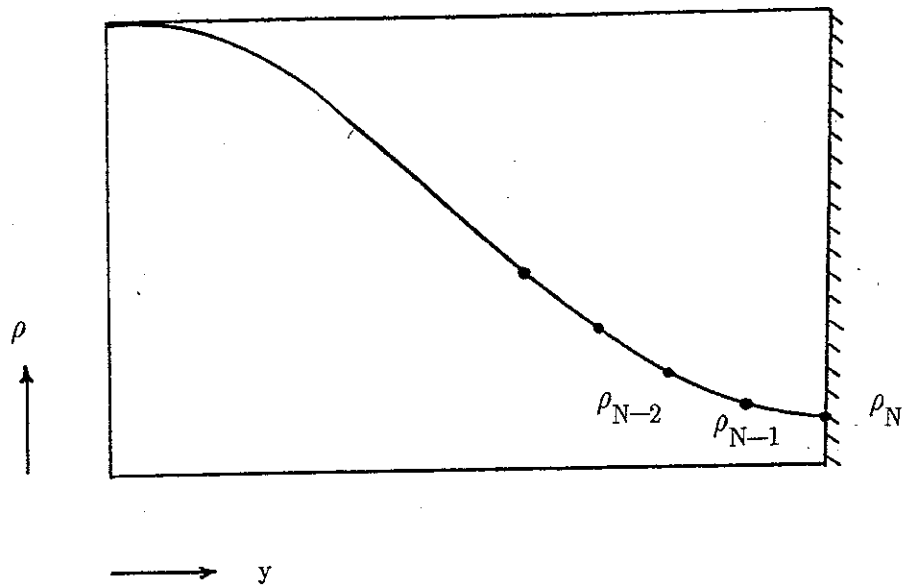

Fig. 6.3 Numerical approximation of compatibility condition for space charge at collector plane.

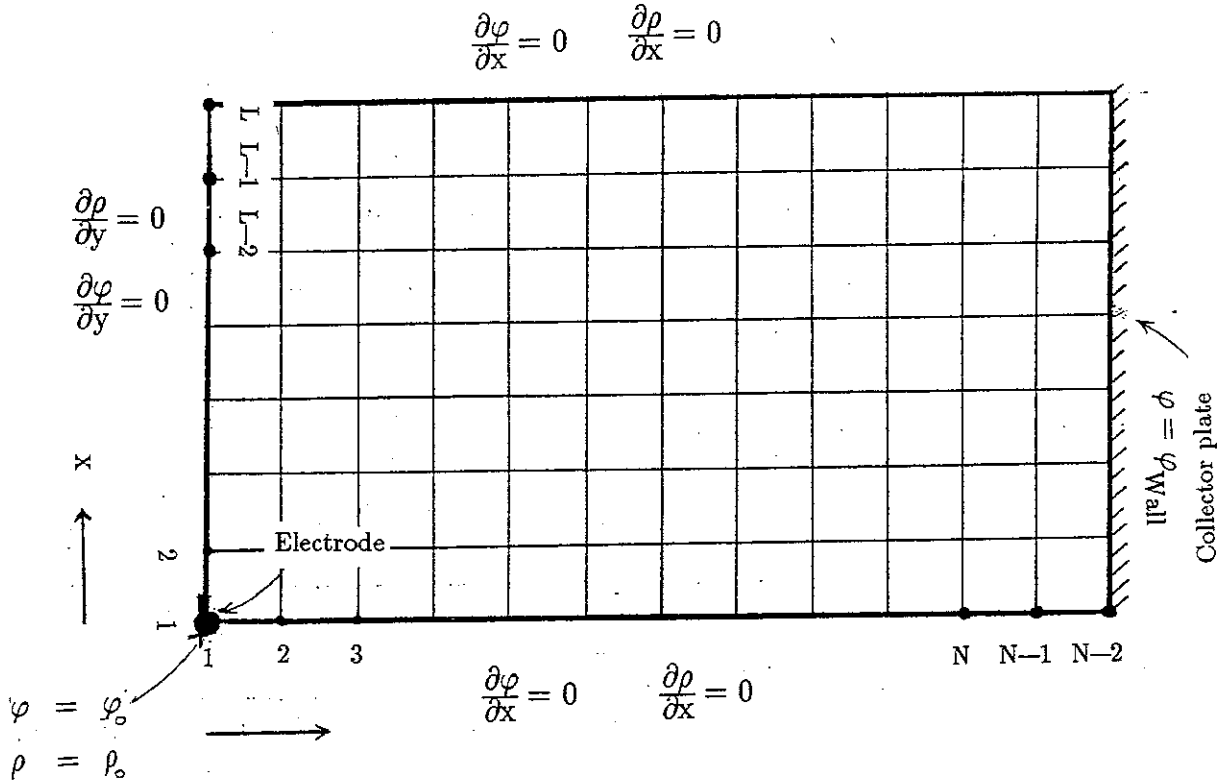

Fig. 6.4 Boundary conditions and grid arrangement for two dimensional electrode—collector geometry.

Furthermore, a second order backward difference discretization of Eq.(6.26) gives the value of the electric field perpendicular to the surface of the collector plate E_{y_N}.

The foregoing descriptions of the boundary condition approximations and the calculation domain, lead to the representation of a grid arrangement for a two dimensional electrode–collector configuration shown in fig. 6.4.

6.4.4) Iterative method of solution

SOR line by line algorithm [56] is selected as the numerical solution method for both Eq.(6.15) and Eq.(6.20). The description of the method is as follows:
The solution of the discretization equations can be obtained by the standard Gaussian elimination method. This is called the TDMA, Three Diagonal–Matrix Algorithm. In this algorithm the discretization of a system of linear algebraic equation for points placed on the grid line in the calculation domain (see fig. 6.5) is presented by

$$\underline{\underline{A}} \cdot \underline{X} = \underline{b} \tag{6.28}$$

where $\underline{\underline{A}}$ is the coefficient matrix containing the information from neighboring points on the grid line, $\underline{X}$ is the unknown values and $\underline{b}$ defines the source terms.

Under–relaxation is a very useful device for nonlinear problems. Therefore under–relaxation is employed to handle the nonlinearity of Eq.(6.20). Furthermore over–relaxation is used to speed up the calculation of the Poisson equation, Eq.(6.15).

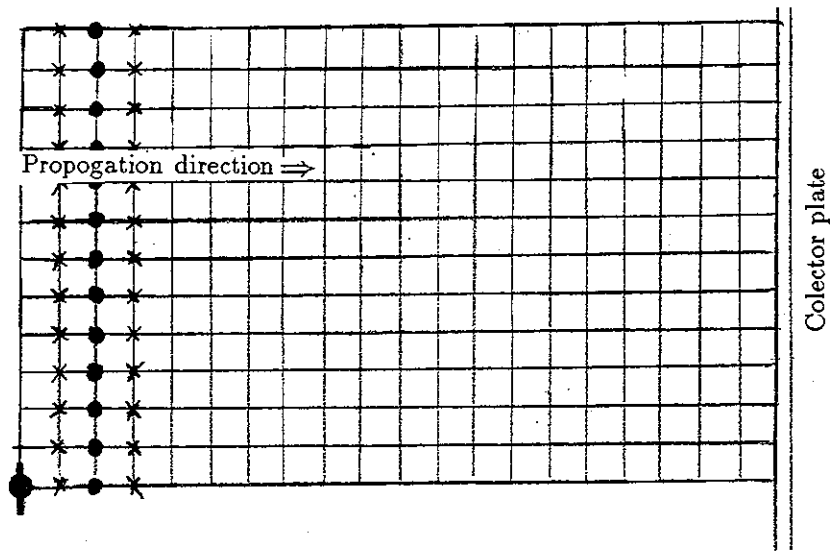

Fig. 6.5 SOR Line by Line method for TDMA numerical algorithm.

In order to reduce the computation time for the calculation of residuals, it is preferred to look at the maximum variations in the solution changes, MAXV as a measure of convergence. This value defines as

$$\text{MAXV} = \text{MAX}\left[\frac{|x_i^o - x_i|}{x_i^o}\right] \tag{6.29}$$

here x_i is the value from the present iteration and x_i^o is the value from the previous iteration.

The iteration procedure for Eq.(6.15) and Eq.(6.20) is coupled so that the result and the computation time is optimized. First it solves Eq.(6.15) for the potential field with an initial guess for φ and ρ, together with the boundary conditions, until reasonable potential and electric field are established. Then it uses the electric field to solve the ionic transport equation, Eq.(6.20) until convergence (see fig. 6.6). In the next step, the space charge field, ρ will be the new initial guess in solving the potential field equation.

This numerical procedure may be summarized in the following steps:

1— solve Eq.(6.15) until convergence,
2— compute electric field,
3— solve Eq.(6.20) with $\rho = \rho_0$ at corona point,
4— resolve Eq.(6.15) with new ρ field,
5— begin from step two.

As it can be seen from the iteration history the solution of Eq.(6.15) is not monotonic after each iteration loop. This is because the new iterated field for ρ has not converged to its maximum value still. Therefore the iteration loops will be repeated until the ρ field has its maximum value and Eq.(6.15) has begun to converge monotonically as the iteration loops progress. Physically this means that the electric field subject to a certain level of space charge is established. The initial conditions for the program start are

$$\begin{array}{ll} \varphi = 0 & \text{for the whole domain,} \\ \varphi = \varphi_{\text{wall}} & \text{at the collector plate,} \\ \varphi = \varphi_0 & \text{at the electrode,} \\ \rho = 0 & \text{for the whole domain,} \\ \rho = \rho_0 & \text{at the corona point.} \end{array} \tag{6.30}$$

6.4.6) Typical CPU–time

The program is written in FORTRAN 77 with double precision. If the single precision is used there will be no significant change in the solution.

For a grid size of 11 × 31 × 11 with single precision the program uses 220 kb of RAM memory. A personal computer with mathematical coprocessor (Olivetti M 300) and 640 kb RAM uses 450 seconds to solve the problem.

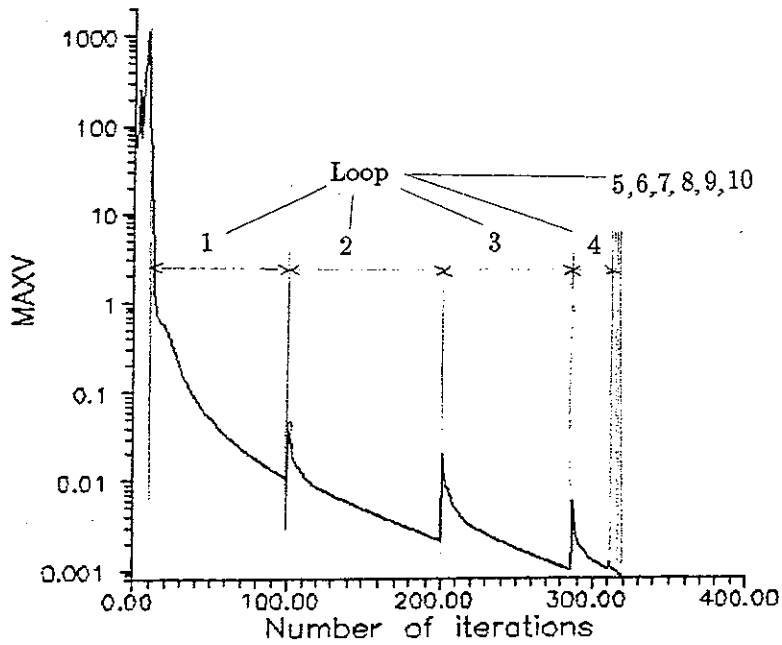

a)

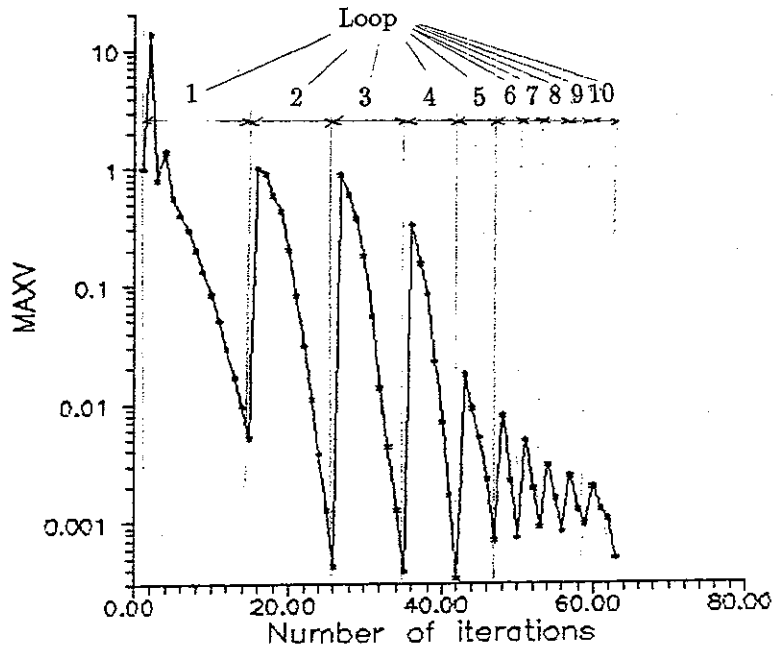

b)

Fig. 6.6 Iteration history of potential field (a) and space charge field (b).

6.5 Numerical results and verifications

6.5.1) Verification of numerical results for one dimensional case

Two parallel plates are placed a distance l_y from each other (see fig. 6.7). One of the plates is grounded and the other one has the potential φ_0 [Volts]. It is assumed that a uniform distributed corona is emitting from the surface of the plate with potential φ_0. With these geometrical and electrical boundary conditions the spatial electrodynamic problem becomes one dimensional with the following analytical solution (see appendix B),

$$\varphi = -\varphi_0 \left(\frac{y}{l_y}\right)^{\frac{3}{2}} + \varphi_0 , \tag{6.31}$$

$$E = \frac{3}{2} \frac{\varphi_0}{l_y} \left(\frac{y}{l_y}\right)^{\frac{1}{2}} , \tag{6.32}$$

$$\rho = \frac{3}{4} \frac{\varphi_0 \, \epsilon_0}{l_y \sqrt{l_y}} \frac{1}{\sqrt{y}} , \tag{6.33}$$

$$J = \frac{9}{8} \frac{\varphi_0^2 \, \epsilon_0 \, b}{l_y^3} , \tag{6.34}$$

for the potential field, electric field, space charge field and the current density field respectively.

In the numerical solution to this problem we will look for the amount of current density at the collector plate ($y = l_y = 150$ mm) for different amount of space charge on the emission electrode (plate). According to Eq.(6.33) the space charge has an unlimited value on the discharge plate, therefore we choose to put the corona discharge next to emission plate at the grid point $y = 1$ mm. The numerical results for different levels of potential are plotted in fig. 6.8. Furthermore, from the analytical solution the amount of current density ($l_y = 150$ mm) for various potential levels are plotted in the same figure, fig.6.8. At the intersection points between the numerical and the analytical results the amount of current density for the numerical solutions equals the amount of current the density for analytical solution.

As it can be concluded from fig. 6.9 and fig. 6.10, there is no significant difference between the numerical and analytical solutions for potential field and the space charge field distributions between the plates ($\varphi_0 = 26$ kV).

6.5.2) Comparison of numerical results with experimental data

The DFM [58] laboratory precipitator facility, shown schematically in fig. 6.11, is designed for investigation of the fundamental processes in a single stage wire–plate precipitator under idealized conditions.

Discharge electrodes can be positioned in the vertical center plane of the duct and with an electrode spacing of $l_x = 100$ mm. The design and the arrangement of the axially–aligned barbed–wire electrodes are specified in fig. 6.12. The pin spacing l_z is 100 mm and the electrode–collector distance l_y is 150 mm. For later references the total

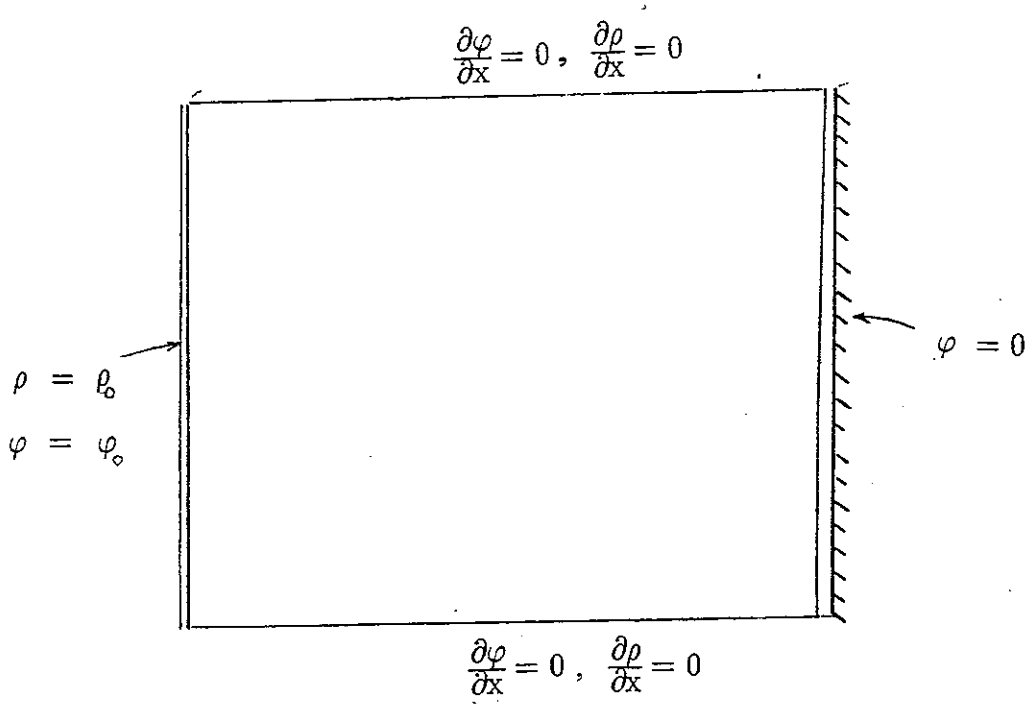

Fig. 6.7 Geometrical configurations and boundary conditions for one dimensional analytical model problem.

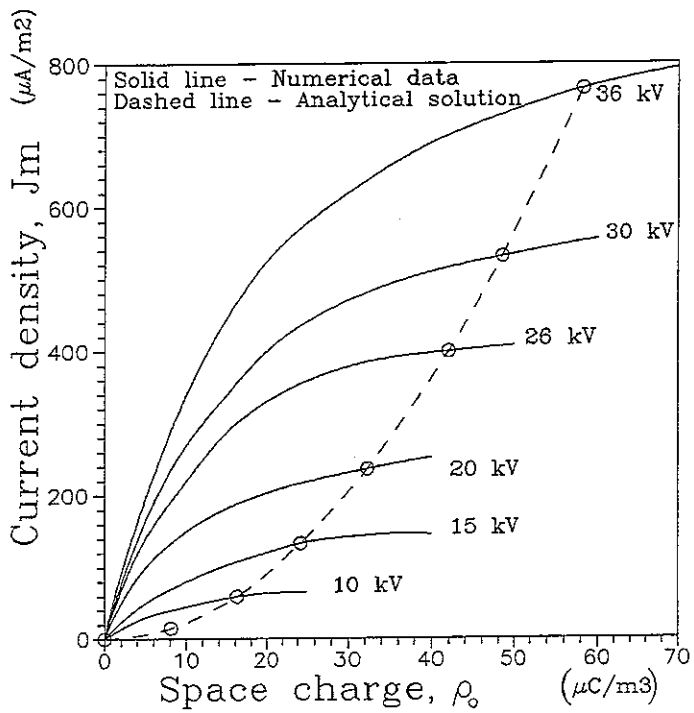

Fig. 6.8 Jm–ρ_0 plot for both numerical and analytical model solution.

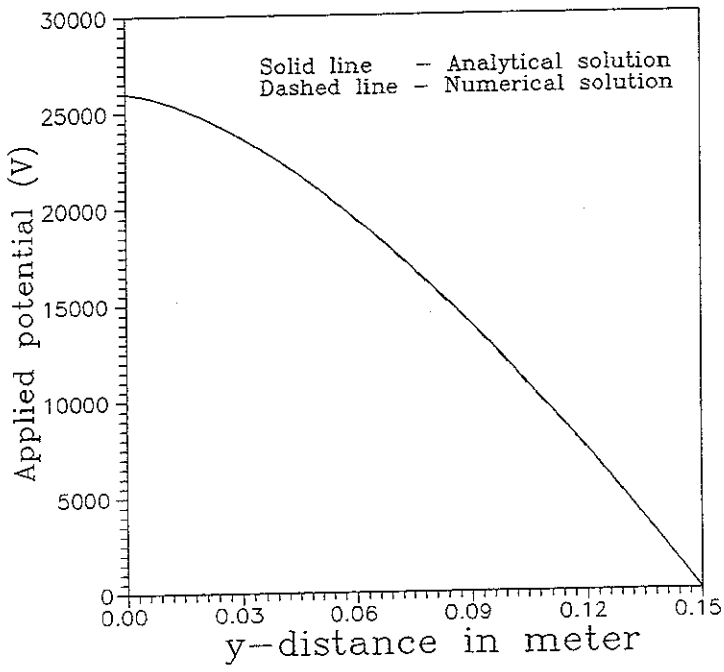

Fig. 6.9 Comparision of analytical and numerical solution of potential field distribution.

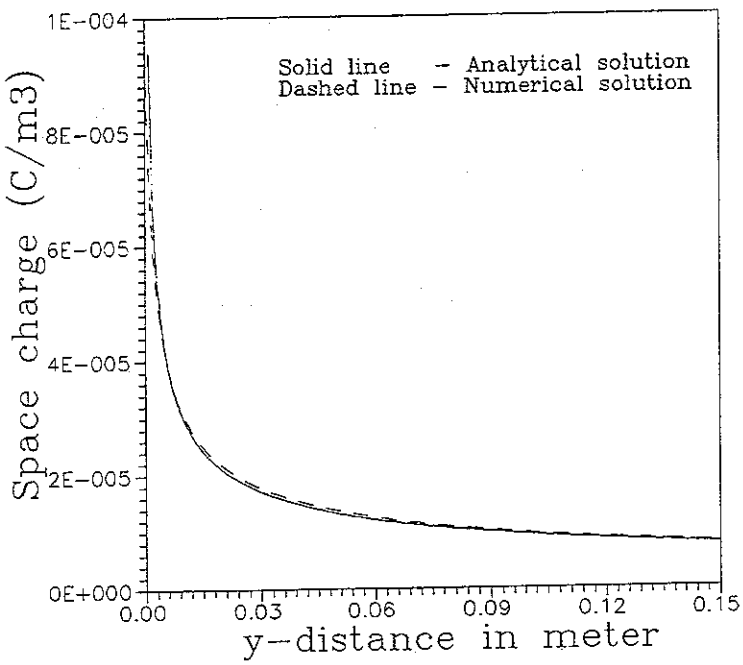

Fig. 6.10 Comparison of analytical and numerical solution of space charge field distribution for one dimentional model problem.

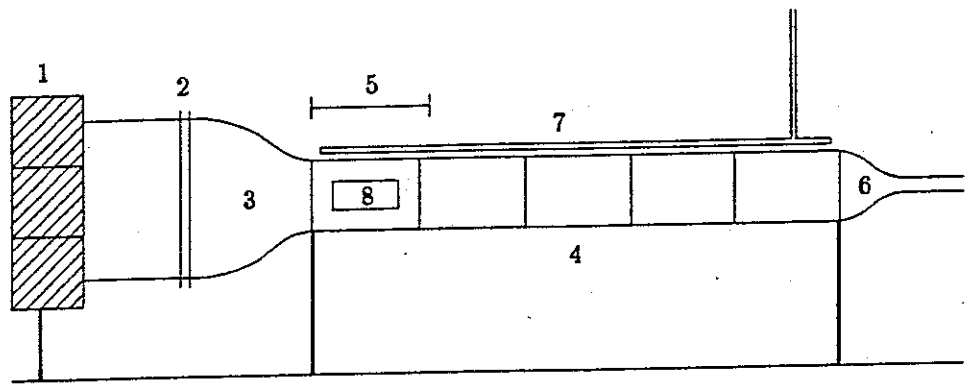

Fig. 6.11 Schematic diagram of the DFM laboratory precipitator facility. 1: Air filter; 2: Screen; 3: Inlet contraction; 4: Test section; 5: Active precipitator test Section; 6: Outlet contraction; 7: High–voltage bus; 8: Mean current density measuring plate, from [36].

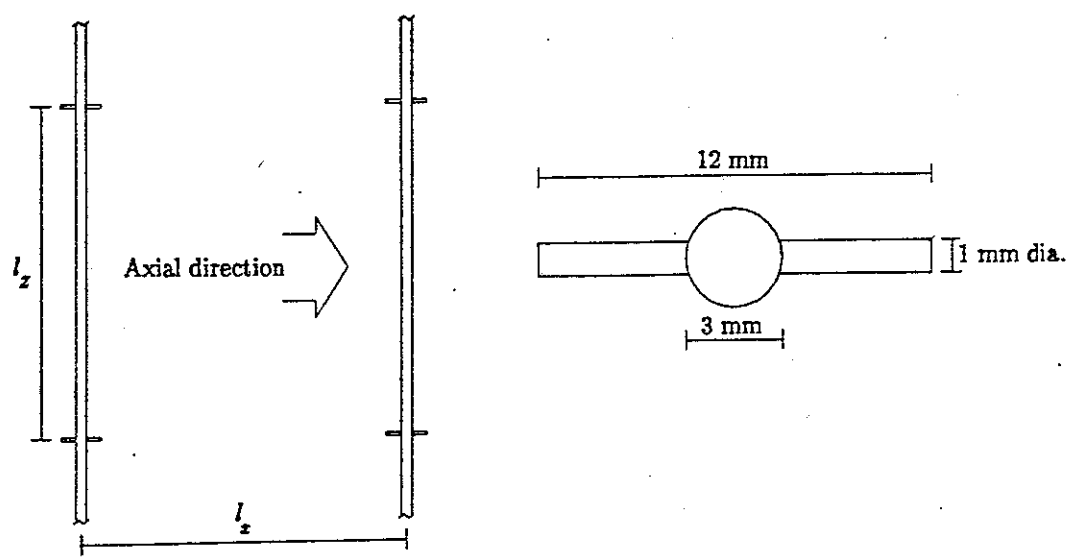

Fig. 6.12 Schematic diagram of design and arrangement of the axially–aligned Ca electrodes, from [36].

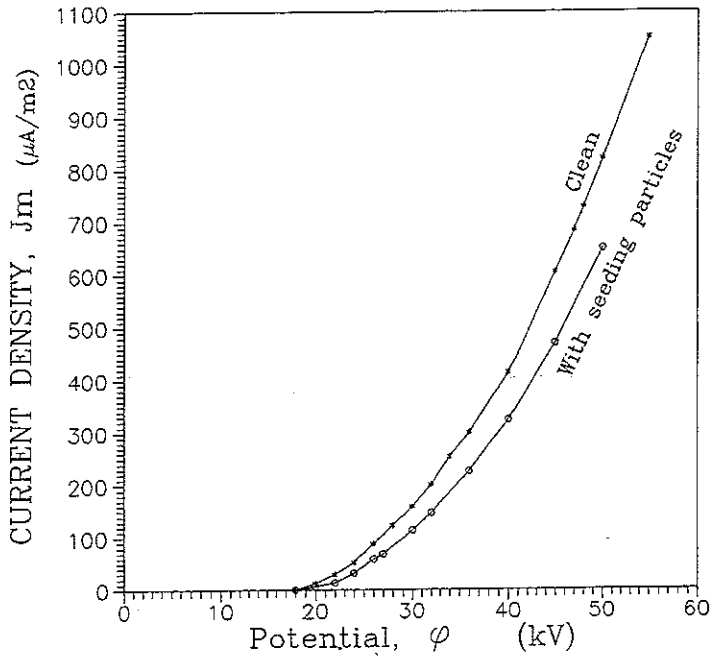

Fig. 6.13 Current–voltage characteristics for Ca–100/100 electrodes.

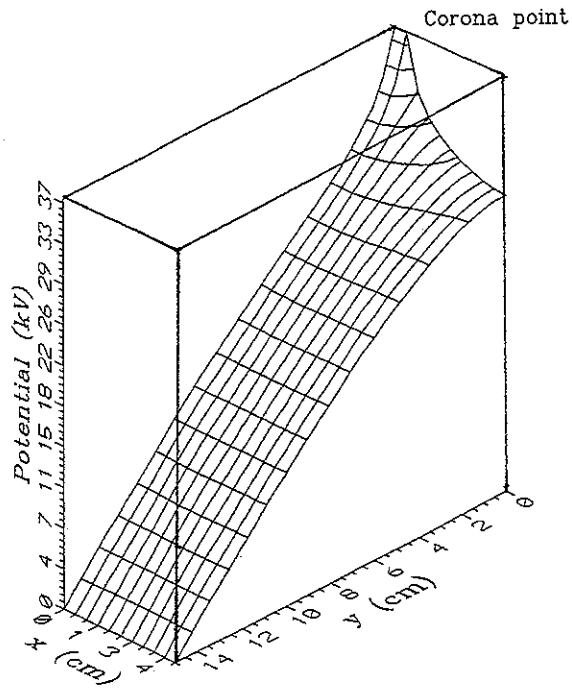

Fig. 6.14 Potential field distribution at the level of corona discharge point for Ca–100/100 electrodes with an applied potential of 37 kV.

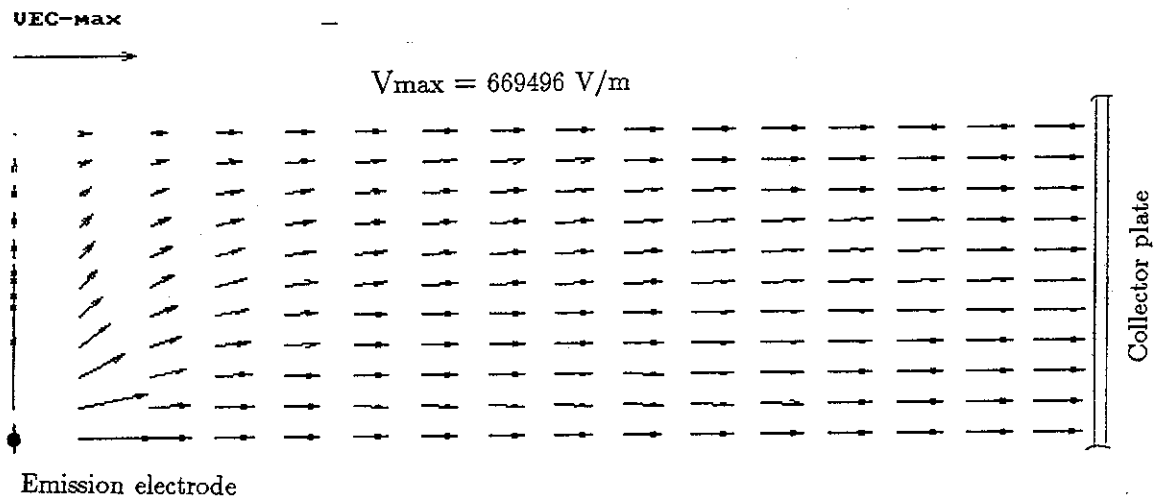

Fig. 6.15 Electric field distribution at the level of corona discharge point for Ca–100/100 electrode with an applied potential of 37 kV.

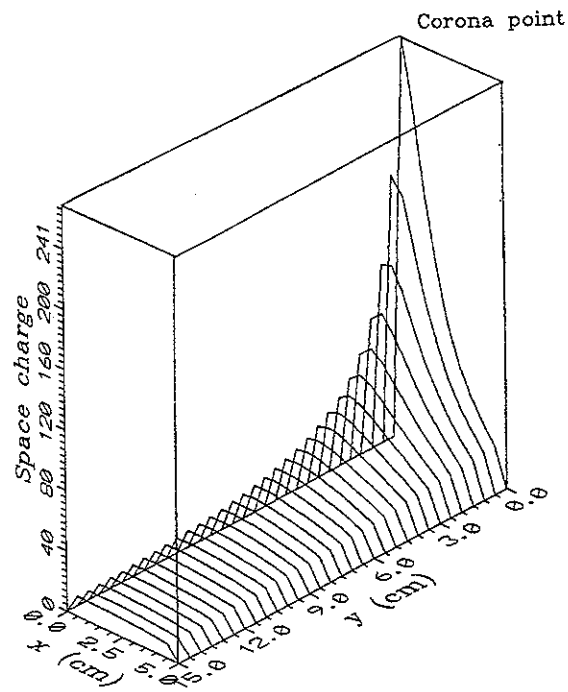

Fig. 6.16 Space charge distribution at the level of corona discharge point for Ca–100/100 electrodes with an applied potential of 37 kV.

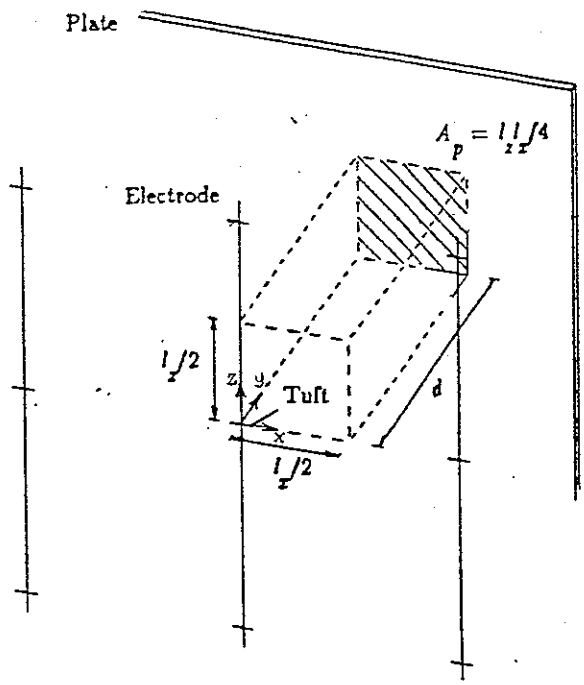

Fig. 6.17 Illustration of geometry of considered problem. The unit of symmetry is indicated by dashed line, from [36].

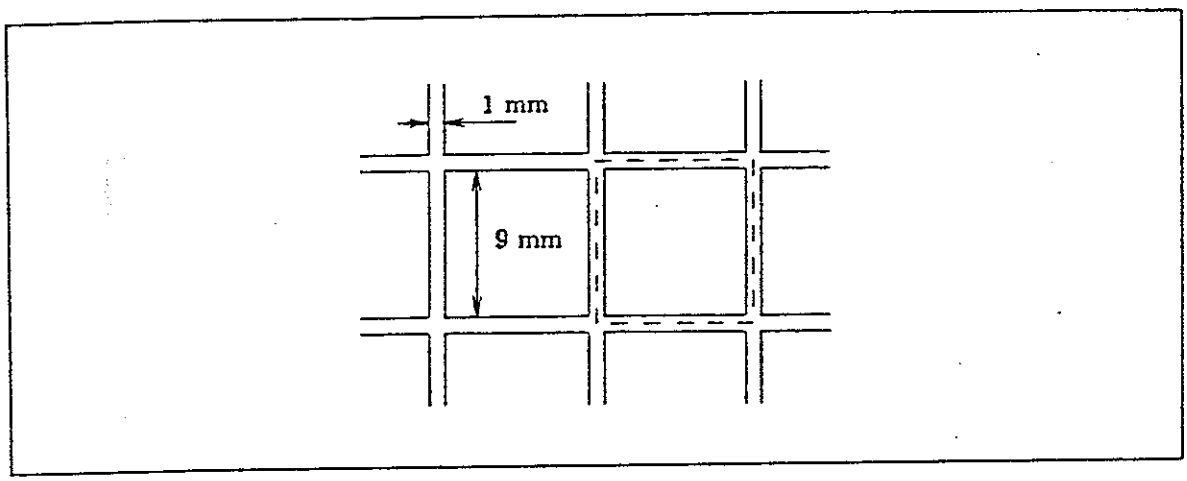

Fig. 6.18 Section of current density measuring plate. The effective probe area is indicated by dashed line, from [36].

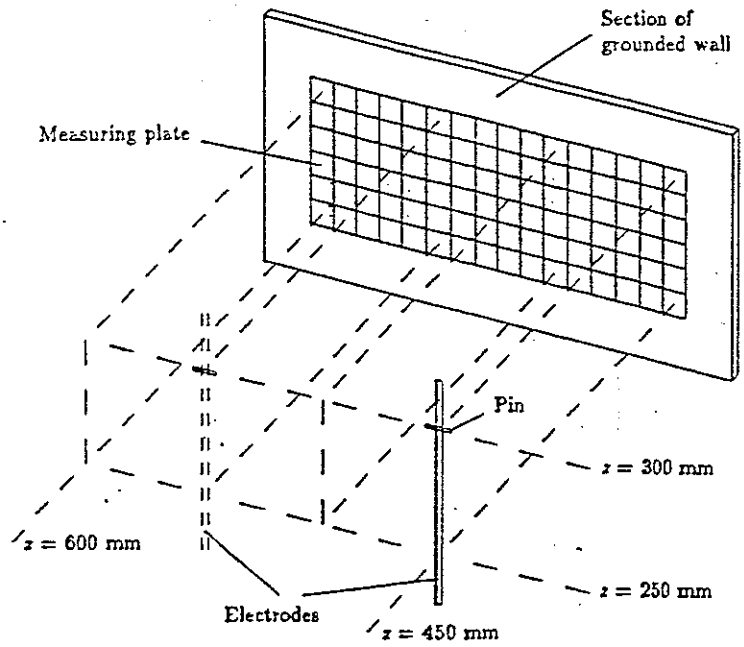

Fig. 6.19 Arrangement diagram for the current density measuring plate. For the Ca–100/100 configuration 10 electrode are positioned at the x = 150,250,350,...,1050 mm, from [36].

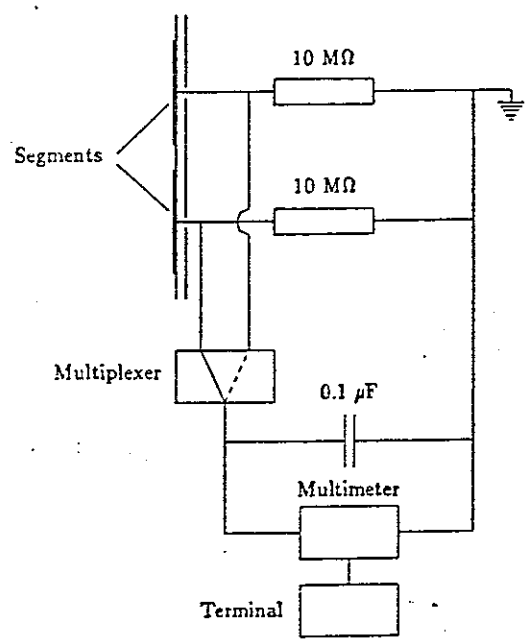

Fig. 6.20 Diagram of the low voltage measuring circuit. The measuring plate is illustrated by two segments, from [36].

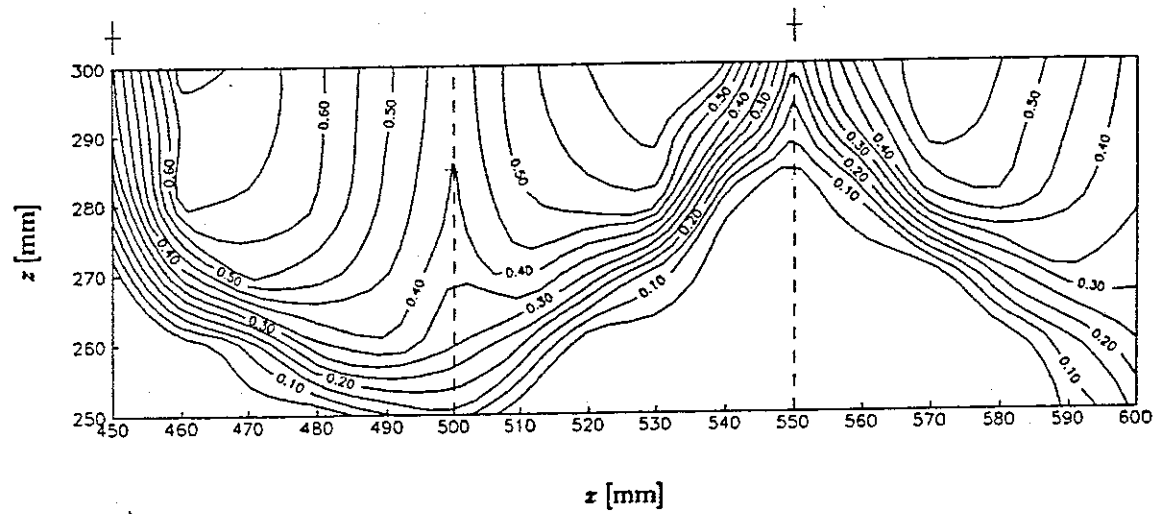

a)

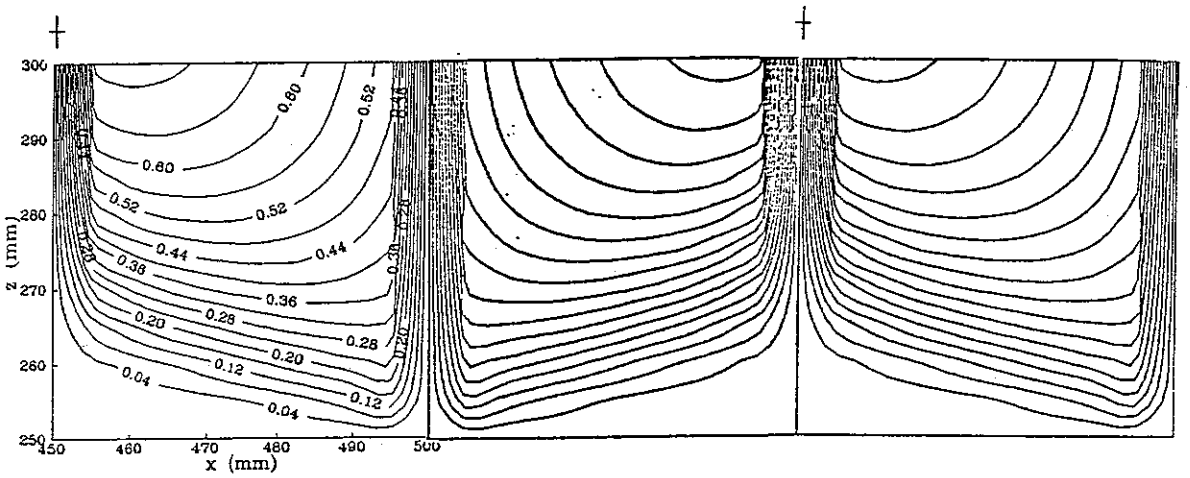

b)

Fig. 6.21 Comparsion between the measured (a) by [36] and the calculated (b) current density at collector plate for three unit of symmetry with an applied potential of 37 kV (electrodes, Ca–100/100). Contours of current density in units of mA/m^2.

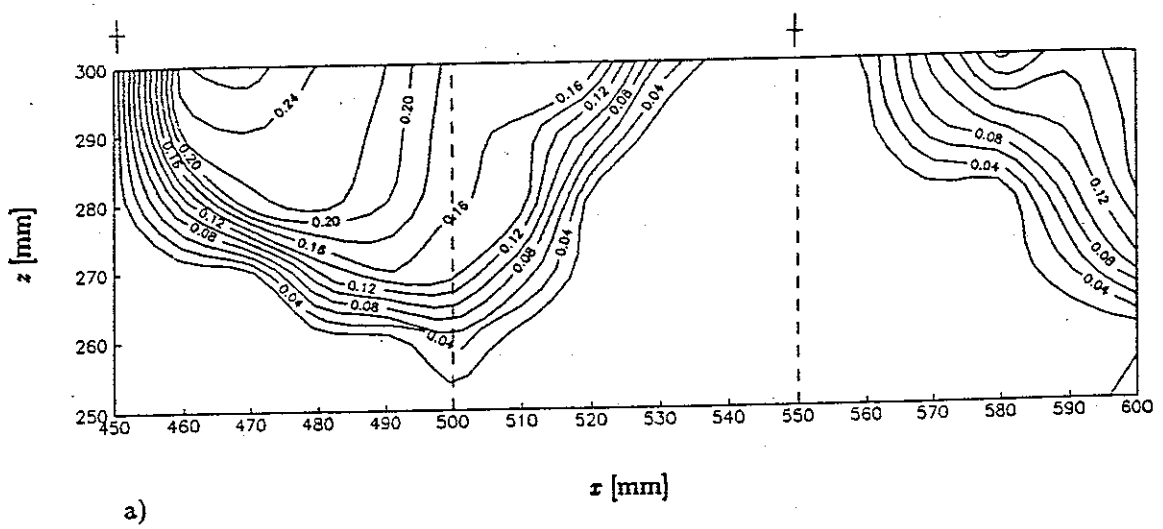

a)

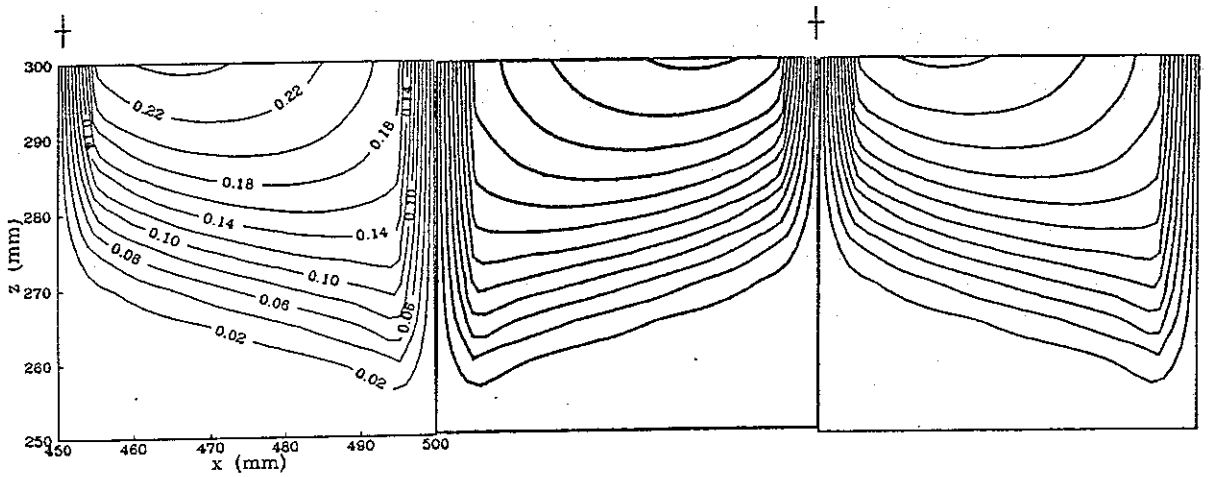

b)

Fig. 6.22 Comparision between the measured (a) by [36] and the calculated (b) current density at collector plate for three unit of symmetry with an applied potential of 27 kV Contours of current density in units of mA/m^2.

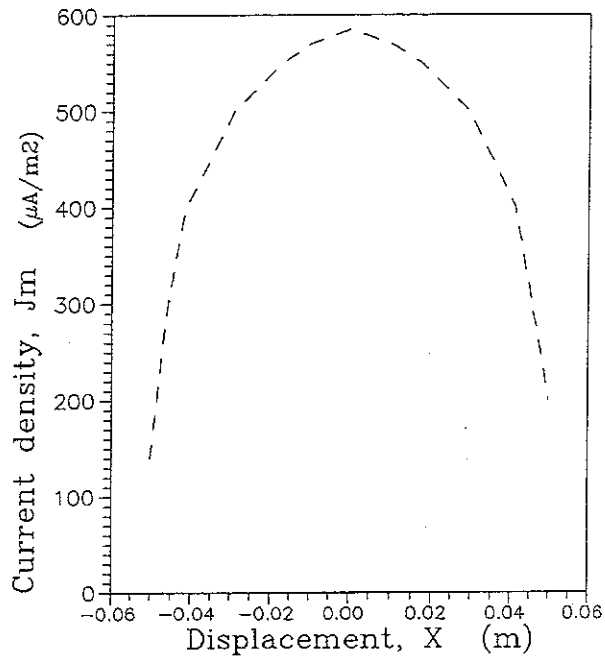

Fig. 6.23 Current density distribution for positive corona discharge measured by [61]. Three axially–aligned wires of 3 mm diameter are placed 100 mm from each other and the electrode collector distance is 115 mm (applied potential 26 kV).

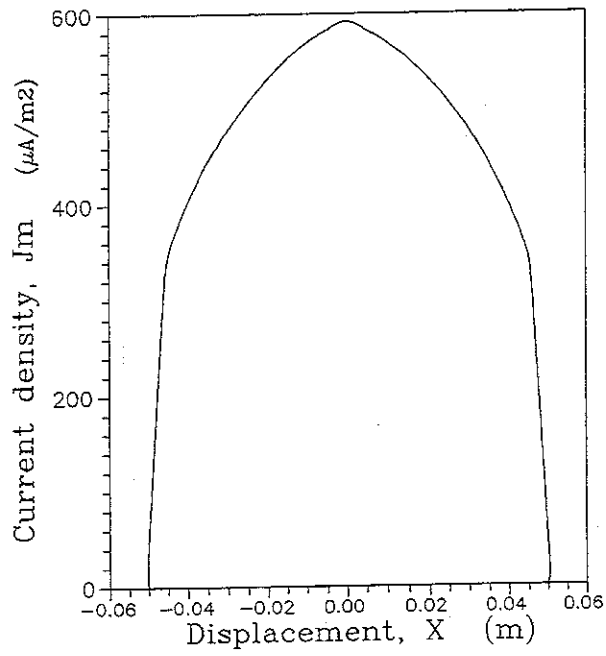

Fig. 6.24 Numerical calculation result for current density distribution based on the experimental data from [61].

geometrical configuration will be denoted as CA–100/100 (Ca–l_z/l_x). The measured current voltage characteristics for the CA–100/100 configuration is shown in fig. 6.13. The numerical calculations for the CA–100/100 electrodes concerning the potential field, the electric field, and the space charge distribution at the level of the discharge point is illustrated in fig. 6.14–6.16. In this calculation the amount of corona space charge is chosen such that the amount of the average current density at the collector plate becomes the same as the measured value.

In order to justify the numerical results it is chosen to look at a measurable quantity like the current density distribution on the collector plate. On the account of the symmetry of the geometrical configurations the measurement is limited to an area of three units of symmetry for the CA–100/100 electrodes (see fig. 6.17 for one unit of symmetry).

The measurements are performed on a copper–clad board used for printed circuits. The board is segmented into a 16 × 6 matrix of 81 mm^2 copper–squares separated by 1 mm wide isolating groves (see fig. 6.18). The positioning of the current density measuring matrix is shown in fig. 6.19.

Each of the segments is grounded through a 10 MΩ resistor and can be connected to a low voltage measuring circuit via a 24–channel multiplexer as shown in fig. 6.20. A Solarton 7151 computing multimeter is used to measure the voltage drop over the effective resistance of each resistor with an input resistance of 10 MΩ of the multimeter. The average current density, assigned to each segment, is calculated by dividing the mean voltage drop by the effective resistance of the measuring circuit and an effective probe area of 100 mm^2.

Figure 6.21–6.22 shows contour plot representing the measurements and the calculated current density distribution on the collector plate for two levels of imposed potential voltage of 27 and 37 kV.

As it can be concluded from these results, there are very good agreement between the measurements and the calculations for both levels and position of the contour lines of the current density distribution except at the symmetry line between two unit areas of symmetry. The mathematical reason for this discrepancy is the supposition of symmetrical boundary condition for the potential field at the yz–plane between two unit cells. Due to this boundary condition the electric field perpendicular to the plane becomes zero, and therefore no space charge can be transported to this region (see fig. 6.15).

In order to reveal, whether the presence of measured current density in this region stems from the unsteady nature of the negative corona discharge it is chosen to look at the experimental data for positive corona discharge [59]. These data also show existence of current density at the symmetry plane between two unit cells (see fig. 6.23–6.24) while the calculations indicate zero current density in this region as expected. The contrast between the experimental data and the numerical solution indicates the fact that there is a space charge in the region between two unit cells of symmetry. The reason for this discrepancy may be explained by a theorem of ionic diffusion.

According to kinetic gas theory the impacts of charged gas molecules with other molecules cause a fluctuating motion of charged gas molecules. The impacts are caused by both molecular motions and the motion due to electric body forces acting on the charged gas molecules, ions and free electrons in the space. Obviously the fluctuations of charged gas molecules will locally change the potential distribution. Therefore due to these changes the electric field becomes locally unsteady and fluctuates with small

amplitudes. These fluctuating motions of charged molecules combined with fluctuations of the electric field causes a weak diffusion of space charge in the whole domain including the region between the unit cells.

Shaughnessy et al, [22] defines the sources of fluctuations to be the instantaneous electric body force and the Trichel pulses. Furthermore [22] explains that with pulsed energization, there is a substantial current density fluctuation which is directly related to fluctuations of electric field and space charge field.

Let us assume that there is a correlation between the fluctuation of the space charge and the electric field. These correlations can be mathematically modeled by decomposing the instantaneous variations of the electric field and the space charge into their mean and fluctuating components as,

$$\mathbf{E} = \overline{\mathbf{E}} + \mathbf{E}', \tag{6.35}$$

$$\rho = \overline{\rho} + \rho', \tag{6.36}$$

where over bars and primes denote time mean and fluctuating components, respectively. Substituting the Eq.(6.35) and Eq.(6.36) into the governing equation, Eq.(6.8) and taking the time average gives

$$\nabla\cdot(b\overline{\mathbf{E}}\,\overline{\rho}) + \nabla\cdot(\overline{b\ \mathbf{E}'\rho'}) = 0\,. \tag{6.37}$$

It is seen that Eq.(6.37) is influenced by the fluctuations through the last term. By using Fick's law analogy the fluctuating term may be modeled as

$$\overline{b\mathbf{E}'\rho'} = -D_i\cdot\nabla\overline{\rho}\,, \tag{6.38}$$

where D_i is the diffusivity coefficient. Inserting Eq.(6.38), with D_i = constant, into Eq.(6.37) results in a new form for the space charge transport equation which contains the contribution of fluctuations of the space charge,

$$\nabla\cdot(b\overline{\mathbf{E}}\,\overline{\rho}) = D_i\cdot\nabla^2\overline{\rho}\,. \tag{6.39}$$

By taking the divergence of the left hand side of this equation and including the contribution of particle space charge as we did in section 6.2, we have

$$b\mathbf{E}\cdot\nabla\overline{\rho} + b(\rho_i + \rho_p)\frac{\overline{\rho}}{\epsilon_0} = D_i\cdot\nabla^2\overline{\rho} \tag{6.40}$$

Equation 6.40 is solved numerically for the CA–100/100 electrode–plate configuration (φ_0 = 37 kV) with different values for D_i where the result for $D_i = 10^{-3}$ m^2/s is illustrated in fig. 6.25.

This figure shows very good agreement with the experimental data. It should be mentioned that this improvement of the numerical results, has no significant influence on the amount of average current density at the collector plate. Now it will be interesting to find out, if this value for D_i can be justified by physical interpretation. First let us look at the most convenient description of D_i through the theorem of molecular diffusion. According to this theorem the diffusion coefficient may be defined

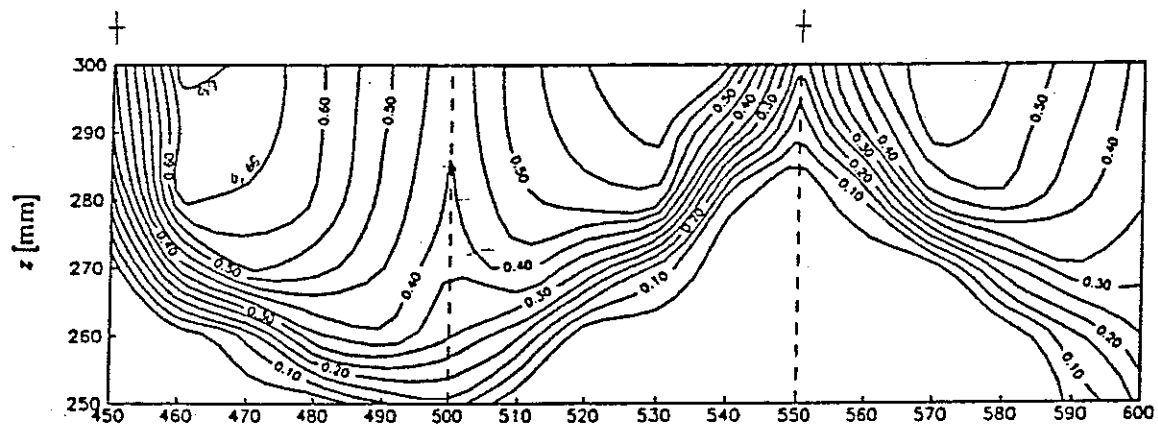

a)

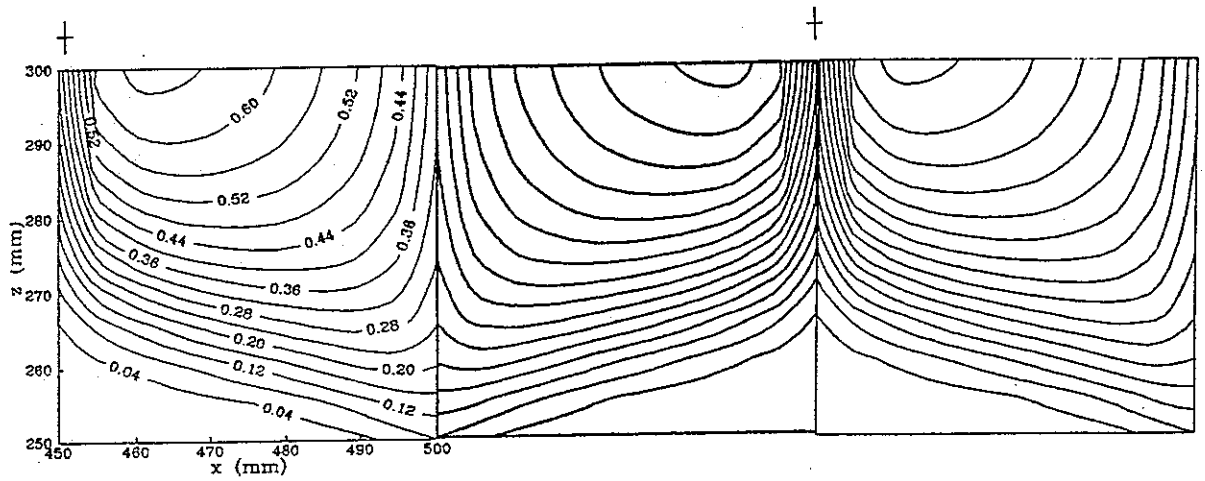

b)

Fig. 6.25 Comparision between the measured (a) by [36] and the improved numerical results for current density at collector plate for three unit of symmetry with an applied potential of 37 kV (electrodes Ca—100/100). Contours of current density in units of mA/m^2.

as

$$D_i = \frac{1}{3} v \cdot \lambda \,, \tag{6.41}$$

where v is the collision velocity of charge carriers, and λ is the collision path. The collision path is the average distance between the gas molecules and it is a function of the state of the gas. λ for air at normal conditions is about 137×10^{-9} m. The charge carrier velocity under the effect of an electric field is given by

$$v = bE \,, \tag{6.42}$$

where b is the charge carriers mobility and E is the mean electric field between the electrodes and the collector plate.

Using the gas ions mobility for air, $b_i = 2.0 \times 10^{-4}$ m^2/Vs, with $E = 2.4 \times 10^5$ V/m, then D_i becomes 2.25×10^{-6} m^2/s and using the mobility for electrons, $b_e = 6.6 \times 10^{-2}$ m^2/Vs, D_i becomes 0.75×10^{-3} m^2/s.

It seems that D_i for electron diffusion is in close agreement with the numerically estimated value. This agreement may be explained through the fact that electrons due to their low mass may be the only particles following the high frequency fluctuations of the electric field.

Furthermore, this concept of ionic and electron fluctuation/diffusion may be used in the case with a pulse energization technique, where the pulsing current induces additionally fluctuations in the electric field and in the space charge. For this case the level of D_i may become higher.

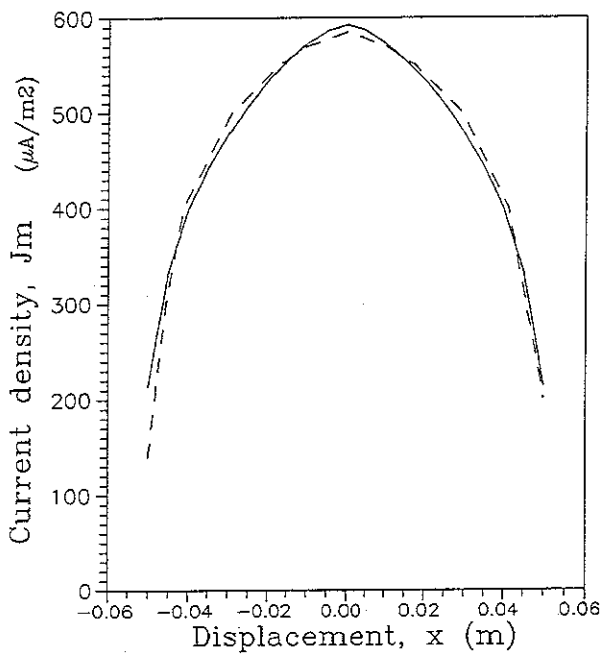

Fig. 6.26 Comparision of Numerical result (solid line) for current density with measured data (dashed line) from [59,61].

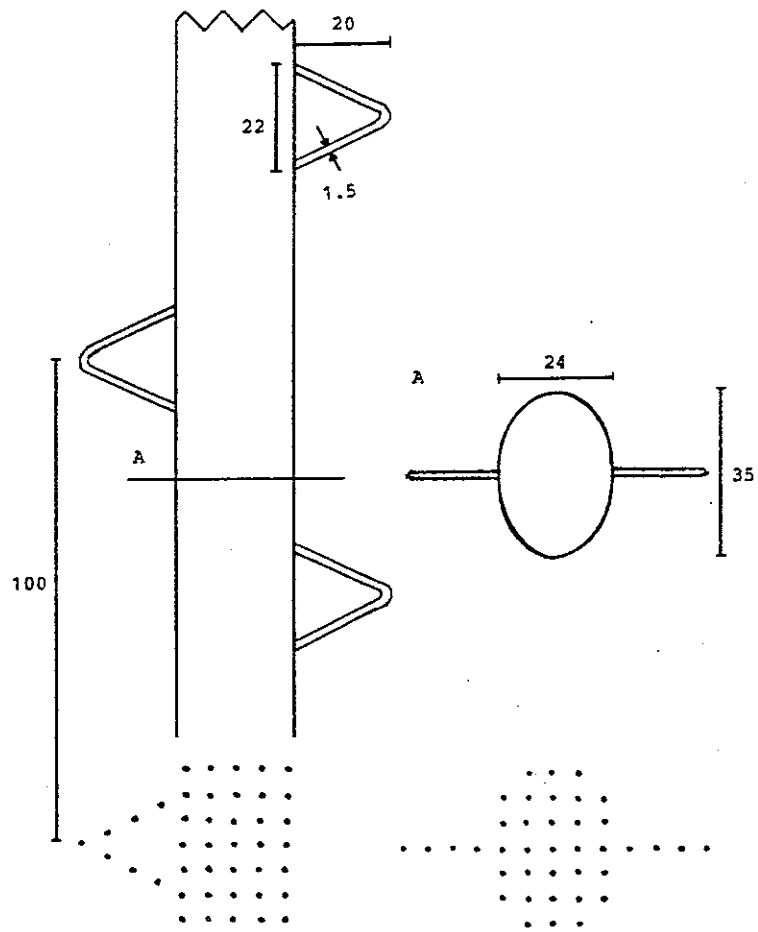

Fig. 6.27 Geometry and numerical grid approximation of fibulax electrodes.

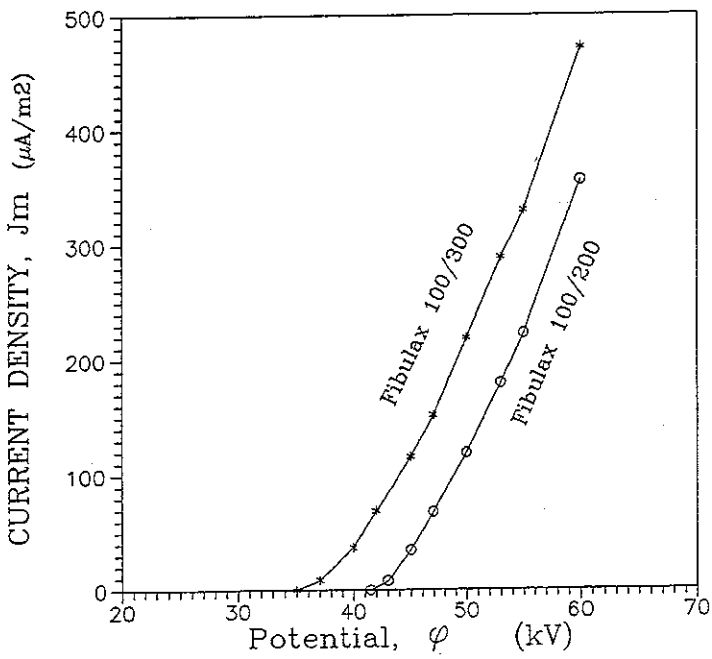

Fig. 6.28 Current–voltage characteristic of Fibulax electrodes for two different electrode spacing.

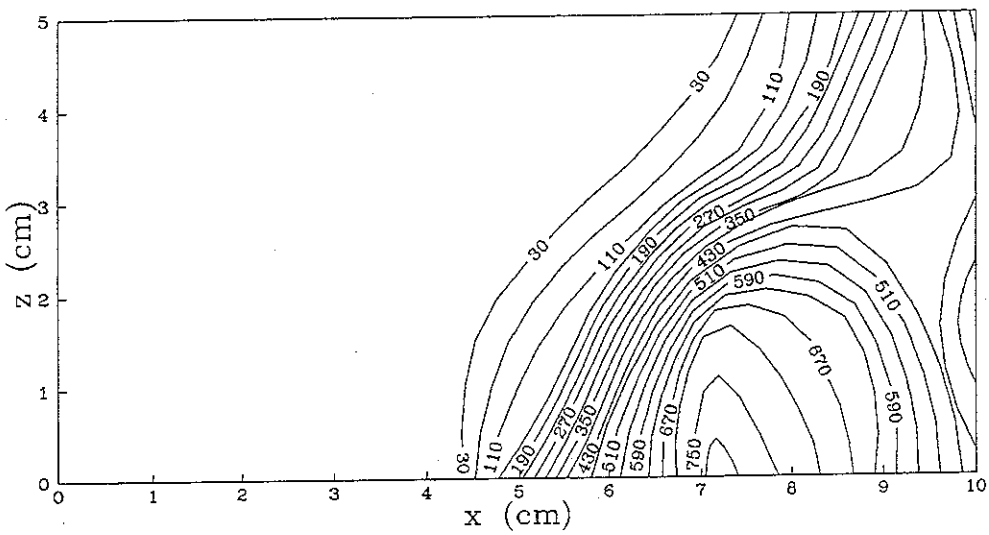

a)

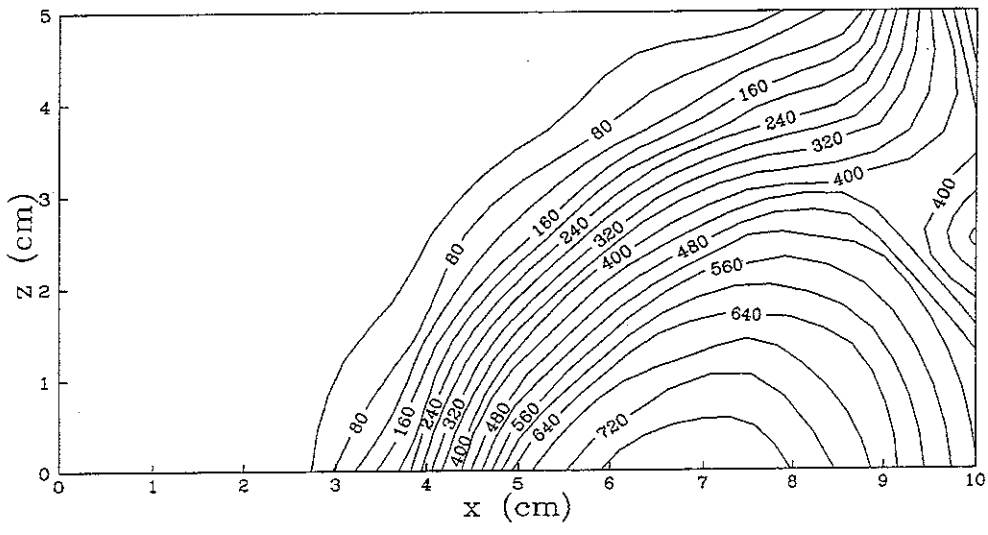

b)

Fig. 6.29 Comparision between the measured (a) in present study and the calculated (b) current density distribution at collector plate for one unit of symmetry with an applied potential of 50 kV (electrodes, Fibulax 100/200). Contours of current density in units of $\mu A/m^2$.

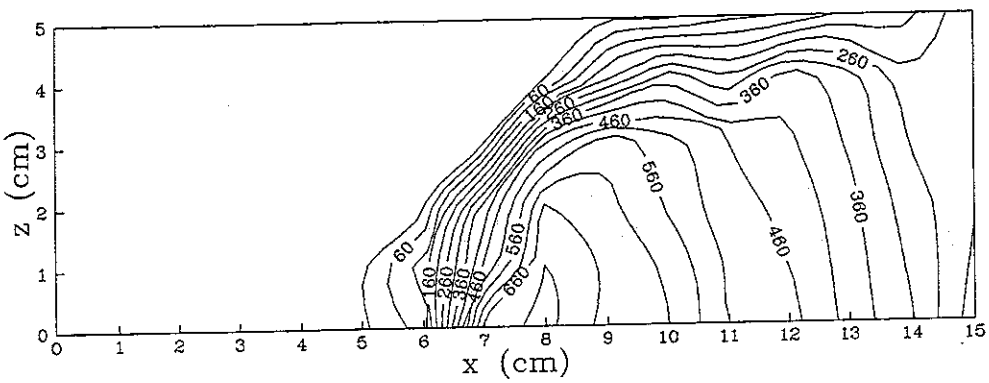

a)

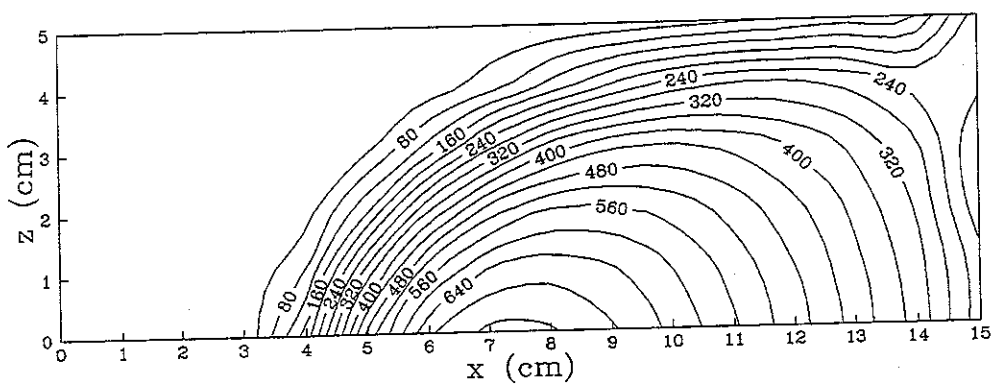

b)

Fig. 6.30 Comparision between the measured (a) in present study and the calculated (b) current density distribution at collector plate for one unit of symmetry with an applied potential of 50 kV (electrodes, Fibulax 100/300). Contours of current density in units of $\mu A/m^2$.

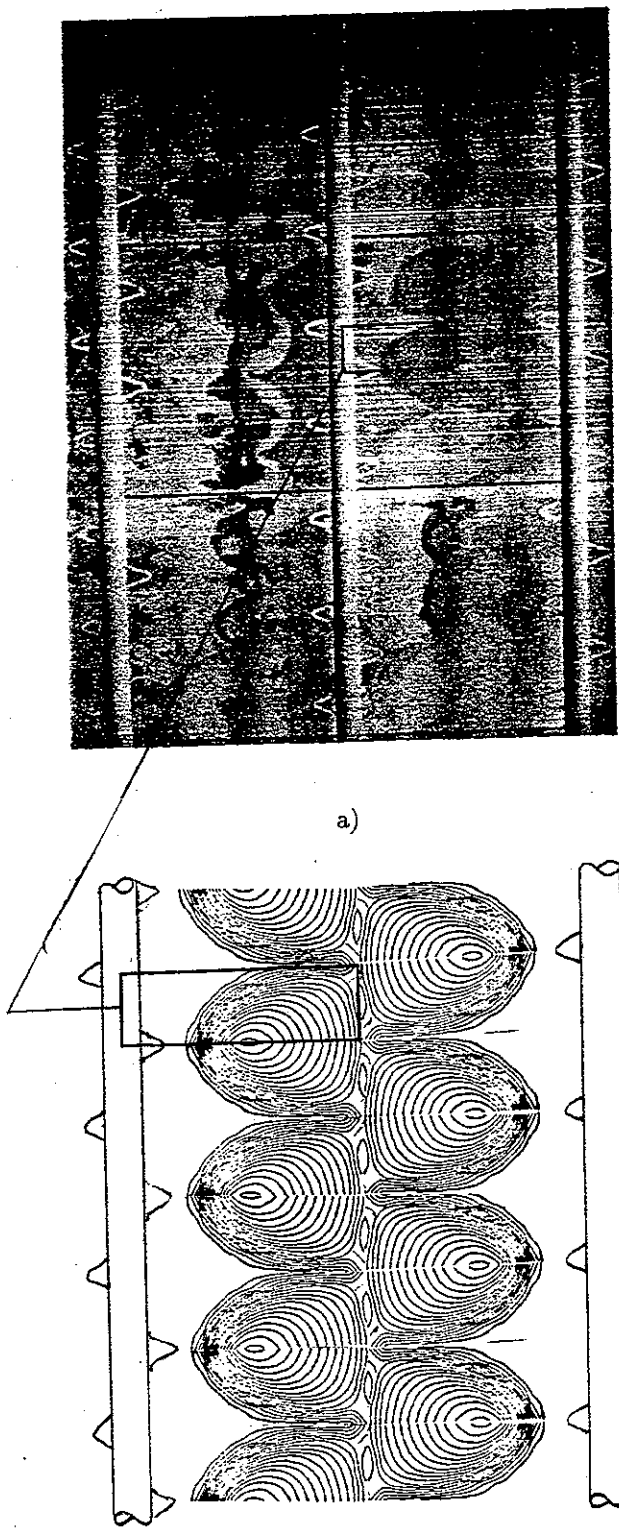

Fig. 6.31 The patterns of collected dust at collector plate with Fibulax electrodes (a). The dust patterns show the regions where the electric forces acts equivalent to the current density patterns (b).

6.5.3) Comparision to other data

For further justification of numerical results the following comparisions with experimental data are performed:

1) *Comparision with two dimensional electrode plate geometry for positive corona discharge*

Figure 6.26 shows the numerical results of current density distribution on collector plate compared to experimental data for positive corona discharge, performed by [59].

As it can be seen, the level of current density between two electrodes is improved to a value identical to experimental measurements on fig. 6.24.

2) *Comparision with three–dimensional tuft corona discharge with Fibulax electrodes*

In order to examine the numerical program for a more complicated form of electrode–collector geometry , it is chosen to verify the numerical results with different electrode spacing of the " Fibulax " electrodes. The geometry of this electrode and the current–voltage characteristics for two different electrode spacing is shown in fig. 6.27 and fig. 6.28, respectively.

The comparision of both the patterns and the levels of current density distribution show good agreement between the experimental meassurements and numerical results, fig. 6.29 and fig. 6.30. This good agreement may further be supported by comparision with the photographic picture of the patterns of precipitated particles on the collector plate, fig. 6.31. These patterns show the regions, where the electric body forces act. These forces are proportional to the current density, and the particle density in these regions are proportional to the strength of electric forces.

6.5.4) Effect of particle space charge

From the experimental data for current–voltage characteristics fig. 6.13, we realize that the particle loading in an ESP, reduces the current density at the collector plate. This is caused by the increase of potential in the region near the emission electrode surface due to increase of the total space charge. The presence of charged particles near the emission electrode, lowers the corona onset at the emission point. In order to estimate the change of corona onset due to increase of particle space charge, the following perturbation may be performed.

Let us assume that the over all changes in ionic space charge density, ρ_i, electric field, E, and current density, J, due to presence of particle space charge, ρ_p, are:

$$\rho_i = \rho_i + \delta\rho_i \,,$$

$$\mathbf{E} = \mathbf{E} + \delta\mathbf{E} \,,$$

$$J = J + \delta J \,.$$

Employing these equations in Eq.(6.14), it becomes

$$J + \delta J = [(\rho_i + \delta\rho_i)b_i + \rho_p b_p]\,(\mathbf{E} + \delta\mathbf{E}) \,.$$

Using the balances $\nabla.\mathbf{E} = \rho_i/\epsilon_0$, $J = \rho_i b_i \mathbf{E}$, and ignoring the contribution of the particle current density due to their low mobility, this equation may be simplified to

$$\delta J = \rho_i b_i \delta\mathbf{E} + \delta\rho_i b_i \mathbf{E} \,. \tag{6.43}$$

From Eq.(6.2) we may write

$$\nabla.(\mathbf{E} + \delta\mathbf{E}) = (\rho_i + \delta\rho_i + \rho_p)/\epsilon_0$$

or

$$\nabla.\delta\mathbf{E} = (\delta\rho_i + \rho_p)/\epsilon_0 \,.$$

Hence, by rearranging Eq.(6.43) in term of $\delta\mathbf{E}$, we may write

$$\nabla.\frac{\delta J - \delta\rho_i b_i \mathbf{E}}{\rho_i b_i} = (\delta\rho_i + \rho_p)/\epsilon_0 \,. \tag{6.44}$$

Now, at the corona emission point the electric field equals the breakdown field, the maximum attainable electric field in the whole region. According to section 6.6.3, (when the potential is above corona start) the variation of the potential at the emission electrode does not show any influence on the level of this breackdown electric field. Therefore, since the particle space charge also changes the potential level (relative to the emission electrode), we may conclude that particle space charge does not influence the electric field at the corona emission point as well. So, if we assume $\mathbf{E} = \mathbf{E}_0$ at this point, then the perturbation due to changes in current density and space charge density gives

$$\delta J = \delta\rho_i b_i \mathbf{E}_0. \tag{6.45}$$

Inserting this equation for δJ into Eq.(6.44) with $\mathbf{E} = \mathbf{E}_0$, then it becomes

$$\frac{\delta\rho_i + \rho_p}{\epsilon_0} = 0$$

or

$$\delta\rho_i = -\rho_p \,. \tag{6.46}$$

Similar to the experimental data, the numerical results also show decreasing mean current density J_m, for increasing particle space charge, see fig.6.32 (applied voltage 36 kV). As can be seen from this figure, a particle space charge of $\rho_p = 7.0 \times 10^{-6}$ C/m^3 will decrease the amount of average current density from 300 to 225 μA/m^2 ($b_p = 5.0 \times 10^{-7}$ m^2/Vs). This is equivalent to the experimental data in fig. 6.13, which comes from measurements on the DFM's Laboratory ESP with seeding particles of 1.2 μm in diameter, an approximate average charge of 52.0×10^{-18} C [60] and an average number density of 6.4×10^{10} m^{-3}, which calculates to a particle space charge of 3.3×10^{-6} C/m^3. This value is about 2 times lower than the estimated value by the numerical calculations. The discrepancy may come from the uncertainty in the measurements of the number of particle density or the charge of the particles.

The number of particle density is measured by counting the number of LDA doppler signals compared to the flow velocity within the measuring volume ($U_0 = 1$ m/s), fig. 6.33.

6.5.5) Back corona due to high resistive dust layer at collector plate

Through many years the precipitation of high resistive dust has been one the main problem for the industry and the ESP manufactures. The high resistive dust at the collector plate interupts the charge flux to the metallic surface of the plate causing an accumulation of free electrons within the dust layer. The charge accumulation within the dust layer appears as corona glow in this region, known as "back corona". This creates a local electric field repellig the precipitated dust from the surface of the dust layer into the gas.

The dust layer formation at the collector plate isolates the conducting metallic surface of the collector plate from the gas. This condition may be estimated numerically by dividing the calculation domain into two zones where the first zone contains the gas phase, while the second zone contains the dust layer phase. Now, from a physical point of view, the only difference between these phases may come from the difference between the material conductivity of these phases. Equation (6.7) for material electric conductivity with considerable variations in the space charge, yields

$$\sigma = b\rho \,,$$

where b is the mobility of the charge carrier and ρ is the total space charge. According to the definition, the electric conductivity of the materials has the following relationship with the materials resistivity, $\mathbb{R}$,

$$\sigma = \frac{1}{\mathbb{R}} \,. \tag{6.47}$$

Employing Eq.(6.3) and Eq.(6.6), then conservation of current for the interface between the gas phase and the dust face yields, assuming steady state,

$$b_{\mathrm{i}}\rho_{\mathrm{i}}\mathbf{E} = \frac{1}{\mathbb{R}_{\mathrm{dust}}}\,\mathbf{E}_{\mathrm{dust}}$$

or

$$b_{\mathrm{i}} = \frac{1}{\mathbb{R}_{\mathrm{dust}}\rho_{\mathrm{i}}}\frac{\mathbf{E}_{\mathrm{dust}}}{\mathbf{E}} \,. \tag{6.49}$$

And the mobility inside the dust layer ($\mathbf{E} = \mathbf{E}_{\mathrm{dust}}$) becomes

$$b_{\mathrm{dust}} = \frac{1}{\mathbb{R}_{\mathrm{dust}}\rho_{\mathrm{i}}} \,. \tag{6.50}$$

If the dust conductivity were the same as the gas conductivity, then there would be no difference between the mobility of the dust phase and the mobility of the gas phase. This situation refers to the case where the collector plates are clean. But, if the dust layer becomes less conductive (higher resistivity) than the gas phase, then according to Eq.(6.50) the dust phase mobility becomes lower than the gas mobility. This situation is simulated numerically using Eq.(6.49) and Eq.(6.50) for an axisymmetrical wire–cylinder ESP. The results for the electric field and the space charge field variations are shown in fig. 6.34a and 6.34b, respectively. As it can be seen from these figures, the amount of space charge and the electric field strength increases dramatically at the interface zone causing a high concentration of ions in this region (back corona).

Further numerical simulations show how the main parameters affecting the back corona phenomena are the current density and the dust resistivity. The increase of

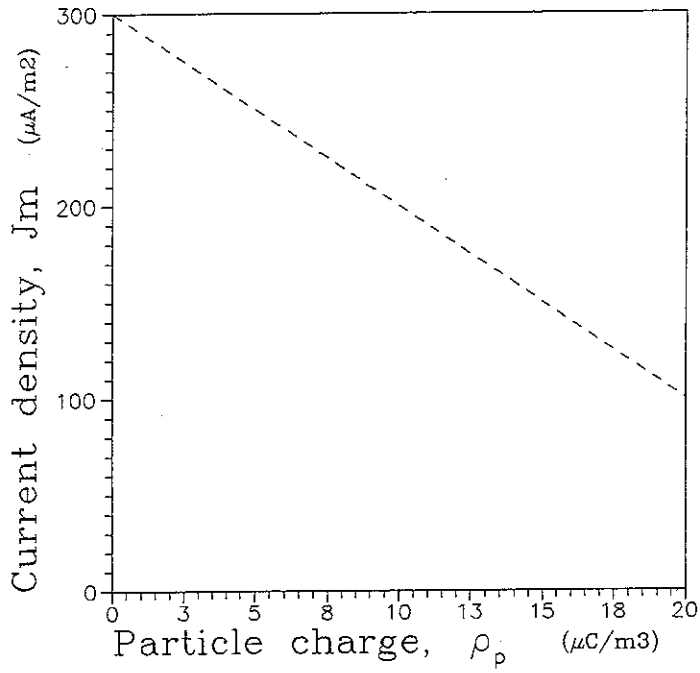

Fig. 6.32 Average current density versus particle space charge for CA—100/100 electrodes with an applied potential of 36 kV (the corona space charge, ρ_0 is 210 $\mu C/m^3$).

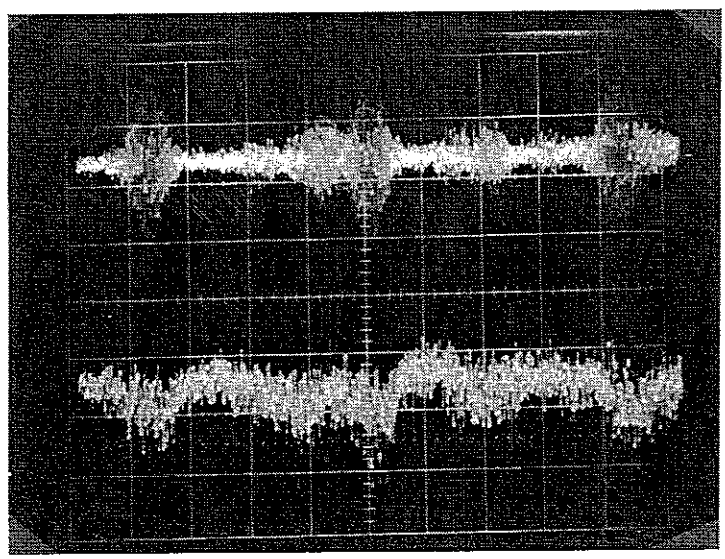

Fig. 6.33 Doppler signals from LDA measurements. The scope is 0.2 ms per division.

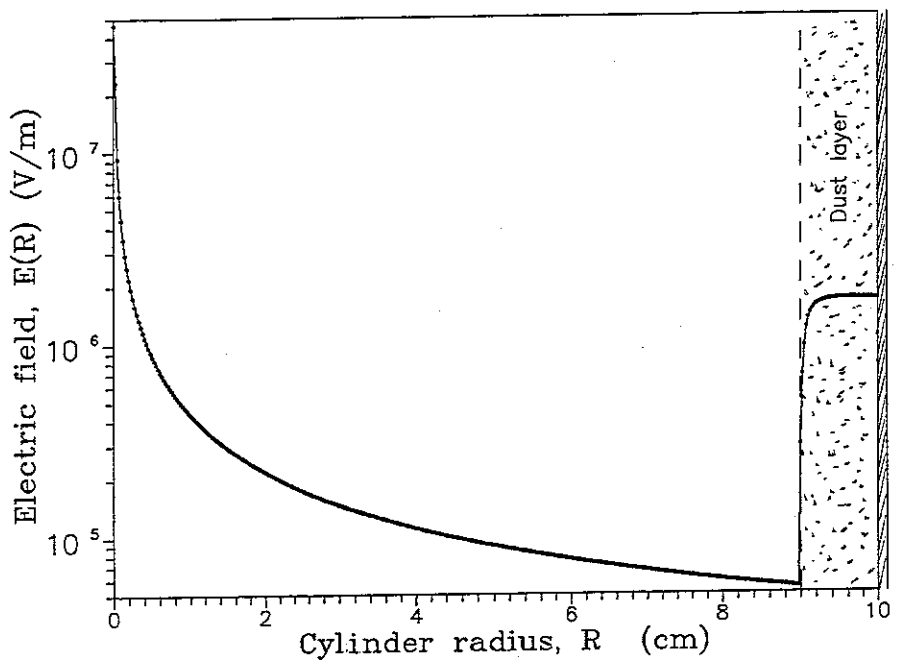

a)

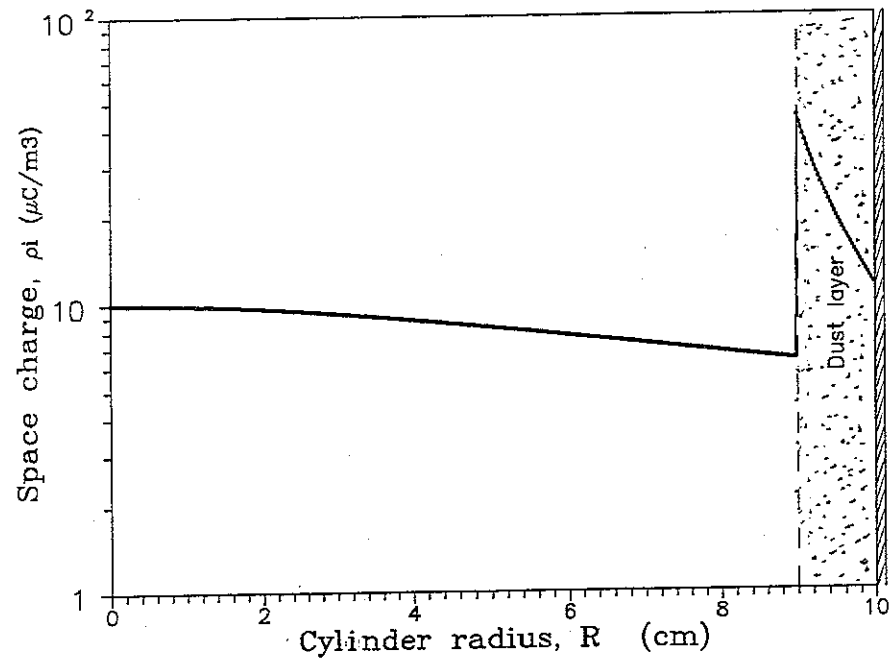

b)

Fig. 6.34 Variation of the electric field (a) and the space charge field (b) in a wire—cylinder ESP with high resistive dust.

current density increases the amount of the ionic space charge which in turn will increase the gas phase conductivity. The back corona occurs as soon as the gas phase conductivity becomes larger than that of the dust phase. Similar to this mechanism, the increase of dust layer resistivity shows the same effect as the increase of current density does. In this, the high dust resistivity lowers the dust phase conductivity relative to the gas phase which leads to the back corona.

The last thing to mention is that the dust layer thickness does not show any influence on the back corona phenomenon. This claim may be supported by the fact that the dust conductivity only depends on the dust chemical compositions. But the contradition between this result and the experimental data published by different authors may be explained by the following words: when the particles accumulate at the collector plate, the gas molecules are captured between the dust particles making a porous two component dust–gas phase. The conductivity of this dust–gas phase is more and more dominated by the dust phase as the number of particles in dust layer increases, which leads to the back corona in the case with high resistive dust.

Since the back corona is a complex area in electrostatics, a more basic investigation of this phenomenon may be necessary to insure the results. Therefore the numerical model of this problem will not be included in the present work.

6.6 Current–charge and potential–charge relations

6.6.1) Current density–corona space charge characteristics

It is interesting to see the relationship between the average current density at collector plate J_m, and the amount of space charge at the corona point ρ_0. In this connection the following experimental data are examined:

1) Negative corona discharge with tufts

Numerical results for the J_m–ρ_0 characteristics for the CA–100/100 and the Fibulax electrodes for different levels of potential is shown in fig. 6.35 and fig. 6.36 respectively.

By plotting the amounts of current density for each potential level (taken from experimental date for current–voltage characteristics, fig. 6.13 and fig. 6.28) on the numerical results for the J_m–ρ_0 characteristic curves, a linear relationship between the corona space charge and current density at the collector plate is observed. Furthermore, as can be seen from fig. 6.35, the slope of the line becomes steeper with decreasing electrode to electrode spacing.

2) Negative and positive corona discharge for barbed wires

These experiments were made by [8] for a wire–plate geometry of $l_x = 0.05$ m and $l_y = 0.025$ m. The current–voltage characteristic for both negative and positive corona is shown in fig. 6.37. Plotting these experimental data on the numerical results for the J_m–ρ_0 characteristics (fig. 6.38) the results indicate a linear relationship between the current density and the space charge for the negative corona discharge, while this relationship becomes nonlinear for positive corona discharge.

Furthermore, the experimental data made by [32] for positive corona discharge for a wire–plate geometry of $l_x = l_y = 0.1143$ m are examined. Plotting the current–voltage characteristics (fig. 6.39) on the numerical results for the J_m–ρ_0 characteristics (fig. 6.40), the result indicate a nonlinear J_m–ρ_0 relationship.

6.6.2) Space charge–potential characteristics

The relationship between ρ_0 and φ_0 for all the cases in section 6.6.1 are shown in fig. 6.41–6.43. The results indicate a linear relation between the corona space charge and potential in those cases with positive corona discharge, while this relationship becomes nonlinear for negative corona discharge regardless whether tuft electrodes or barbed wires are used.

6.6.3) Implication of observations

In the cases with negative corona discharge, there is a linear relationship between the current density and the corona space charge, which may be expressed as

$$J_m = \alpha \cdot \rho_0 , \tag{6.51}$$

where α is the slope of the line.

According to Eq.(6.8) the amount of current density from electrode to collector plate remains constant. Therefore we may write

$$J_m = b_i \cdot E_0 \cdot \rho_0 , \tag{6.52}$$

so

$$\alpha = b_i \cdot E_0 , \tag{6.53}$$

where E_0 is the corona electric field, $(\frac{\partial \varphi}{\partial n})_0$ and b_i is the ion mobility at the corona point. Assuming $b_i \simeq$ constant will limit the electric field to $E_0 \simeq$ constant. This means, that there will be no changes in the level of E_0 by going from one level of potential to another. A possible explanation may be that the level of the electric field at the electrode depends on the amount of the induced space charge around the electrode. When the potential is raised, the amount of the space charge around the electrode will also increase. The increase of the space charge around the electrode, may cause the increase of potential in this region, which in turn may limit the electric field and hold it constant at the electrode.

For the cases with positive corona discharge there is no linear relationship between the current density and corona space charge, but instead the relationship between the corona space charge, ρ_0, and the applied potential, φ_0, becomes linear,

$$\rho_0 = \beta (\varphi_0 - \varphi_s) \tag{6.54}$$

where β is the slope of the line and φ_s is the corona start potential. It should be mentioned that this linear relationship occurs, when the discharge electrodes are thin. In this case the assumption of point–form corona discharge in the numerical discretization, becomes physically correct due to electrode geometry. For thick electrodes this linear relationship is not valid any more (see fig. 6.43). Notice that Eq.(6.54) is equivalent to Eq.(6.33) for the one dimensional analytical model in the plate to plate configuration.

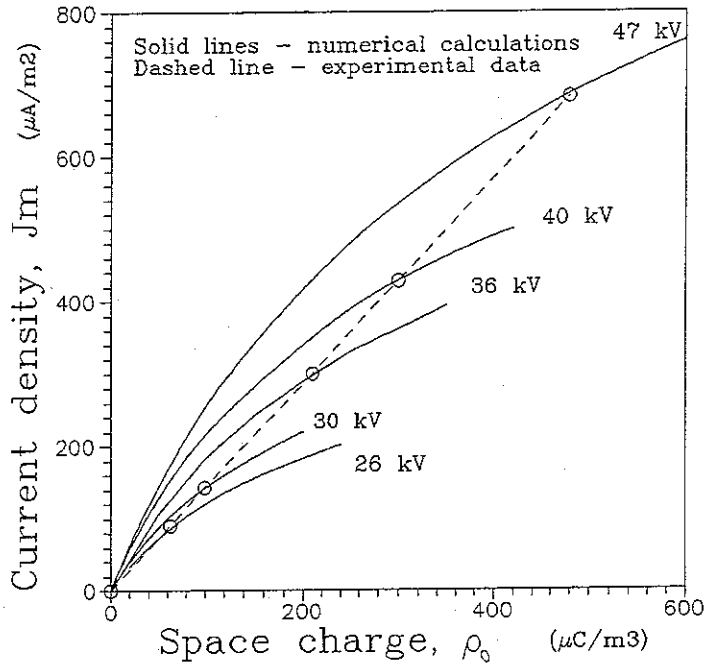

Fig. 6.35 J_m–ρ_0 characteristics for Ca–100/100 electrodes.

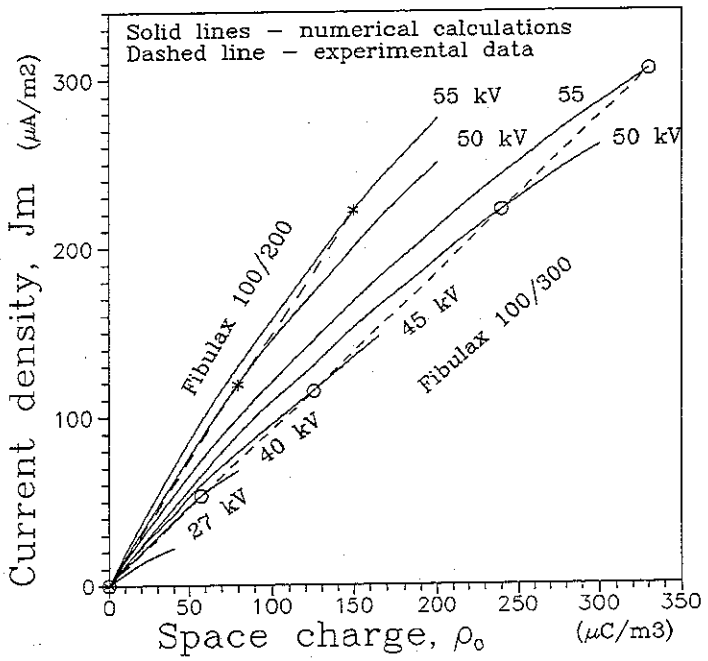

Fig. 6.36 J_m–ρ_0 characteristics for Fibulax electrodes.

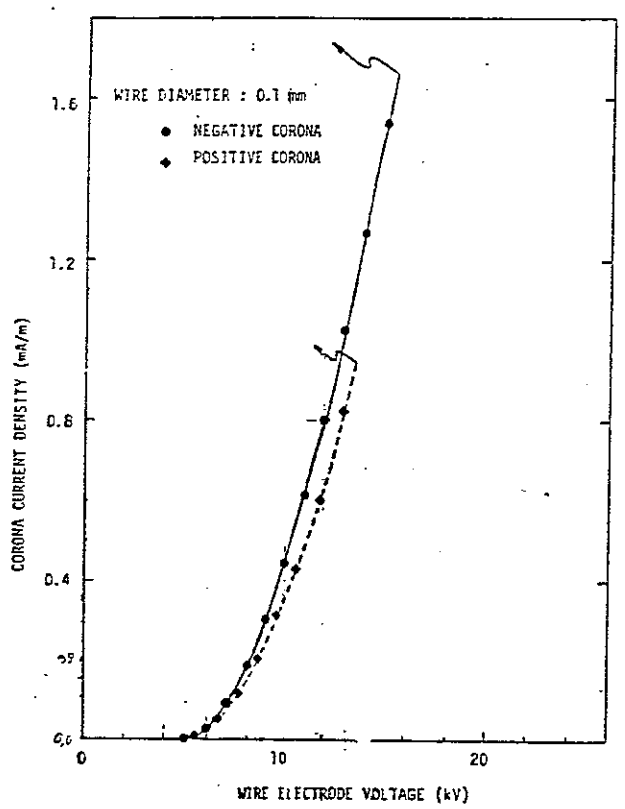

Fig. 6.37 Current—voltage characteristics for the 10—wires and plate precipitator, from [8].

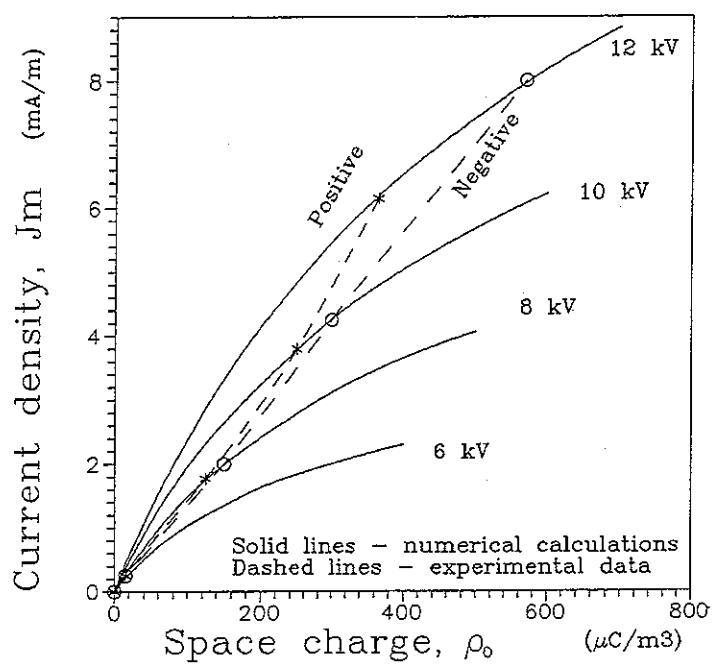

Fig. 6.38 J_m–ρ_0 characteristics for both positive and negative corona discharge based on data [8].

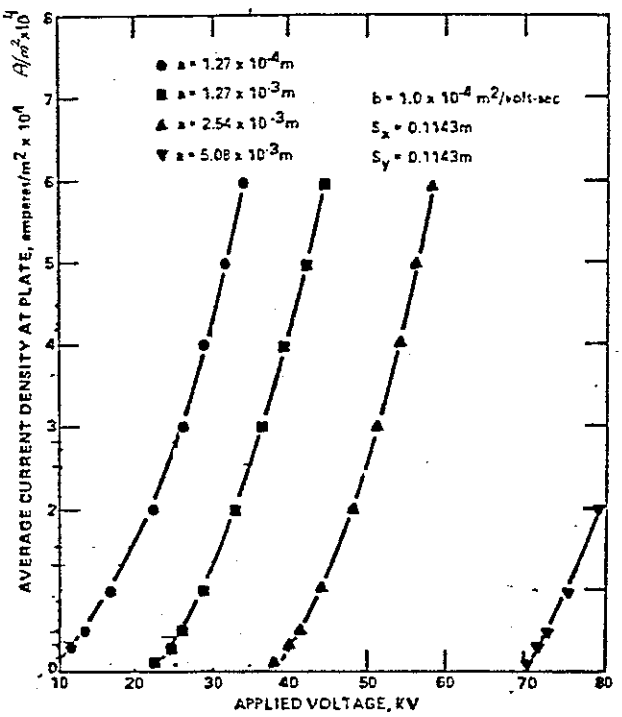

Fig. 6.39 Variation of current–voltage characteristics with changing corona electrode diameter, from [32].

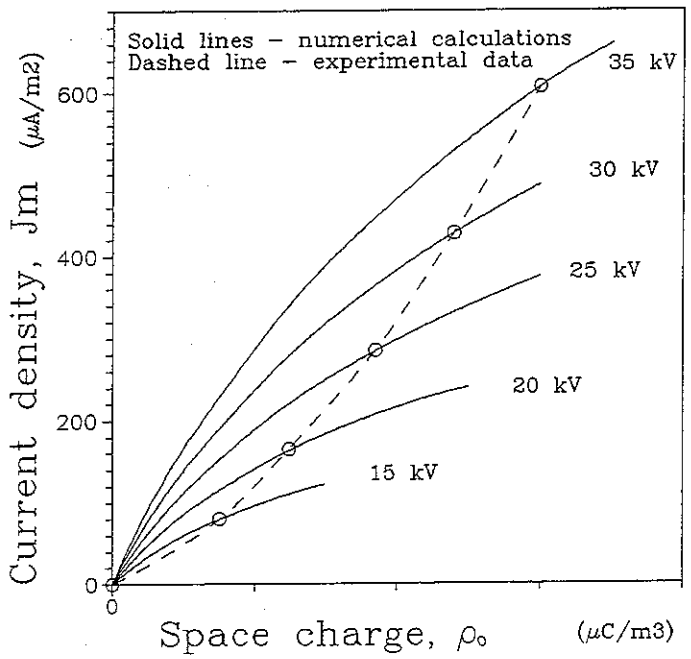

Fig. 6.40 J_m–ρ_0 characteristics of positive corona discharge based on data from [32].

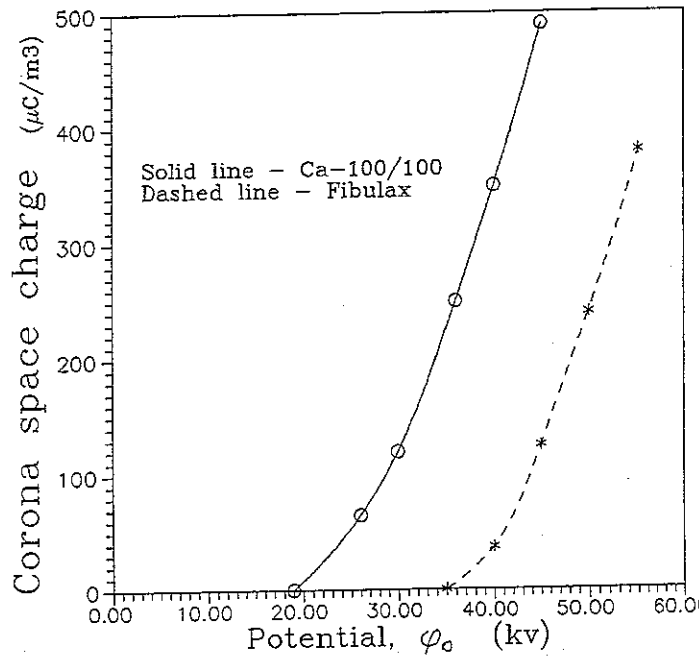

Fig. 6.41 ρ_0–φ_0 characteristics for Ca–100/100 and Fibulax 100/300 electrodes.

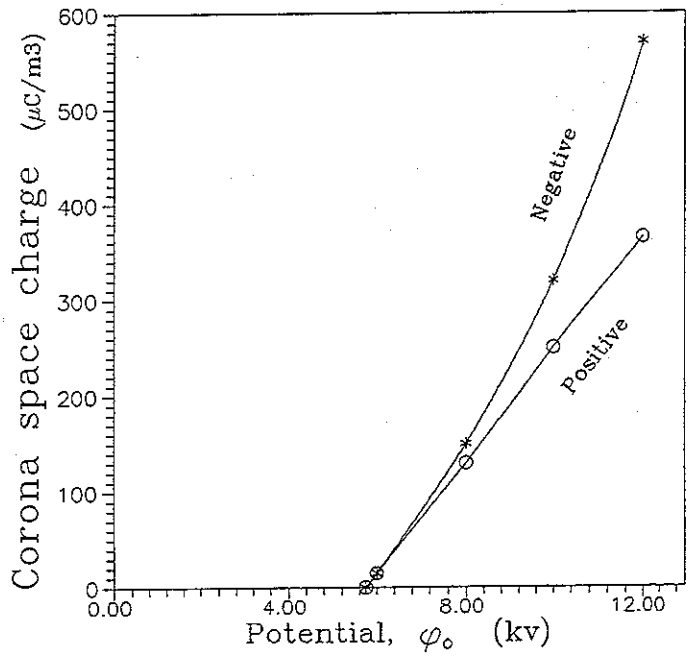

Fig. 6.42 ρ_0–φ_0 characteristics for both positive and negative corona discharge for wire electrodes based on data data from [8].

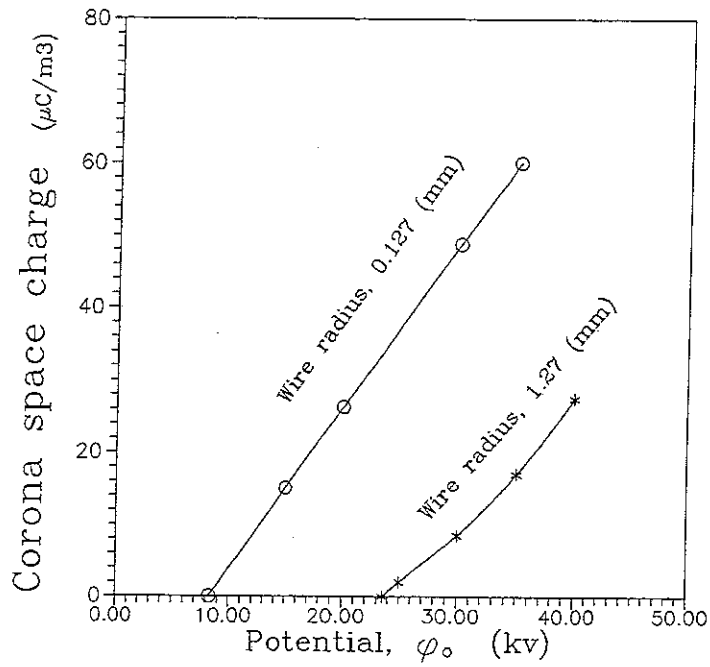

Fig. 6.43 ρ_0–φ_0 characteristics of positive corona discharge with different wire radius based on data from [32].

6.7 Conclusion and recommendations

The main mechanism in electrostatic precipitation of particulate matters in industrial gases is the electrical forces in the system. Therefore, it is necessary to have an accurate calculation of the electrical conditions in order to determine the efficiency. The electric field in a commercial ESP is three–dimensional and is strongly affected by the geometrical configuration and the variable boundary conditions due to presence of charged particles in the gas or dust layer at the collector plate. Therefore, a useful predicting model must include these parameters and should be able to handle the variation of them. A simple numerical method is developed to calculate the three–dimensional electrodynamic conditions, able to take the contribution of the spatial particle space charge variation along the ESP into account. In chapter *8* we will show that the contribution of the particle space charge has strong influence on the current density and the efficiency. This numerical method has made it possible to obtain accurate numerical solutions for complex physical and geometrical problems. All the existing models ignore the particle space charge effects and most of them treat the positive corona discharge due to simple well defined mathematical problems of two–dimensional "wire to plate" or "point to plate" electrode–collector geometries.

The model is able to calculate the electrical conditions where the pulse energization technique may be applied. Here, the microscopic fluctuation of the electric field and the space charge field are molded as the ionic diffusion flux. Beside this, the calculations indicate that the ionic diffusion as a natural phenomenon changes the electrical conditions at the interface between the symmetrical cells. This has been examined through comparison of the measured current density with the numerical calculation results.

Using simple numerical algorithms on an equidistant grid has made it possible to reduces the calculation time and numerical operations which in turn minimize the numerical errors and maximize the accuracy of the results.

In the lack of a convenient mathematical model in calculation of corona–space charge condition, the model uses the experimental data for current–voltage characteristics in order to calculate the amount of space charge at the corona point. The current–voltage characteristics are taken from laboratory measurements for different electrode–plate geometrical configurations. It should be mentioned that the amount of corona discharge changes by changing any parameters in the system, therefore as long as there is not a convenient model for prediction of the corona discharge, it is limited to investigate the other parameters' influence on the system independently of experimental data.
An analytical model problem for a plate to plate geometry is developed to verify the numerical results. Furthermore, the meassurements of current density distribution at collector plate supports the verification of the numerical results for both two and three–dimentional cases. The measurements for two dimensional wire–plate ESPs are taken from [8,32,61]. The verifications show very good agreement with the analytical model problem and the experimental data.

The particle–space charge reduces the ionic space charge and hence the current density at the collector plate. This is the general behavior of the system with strong influence on the ESPs efficiency. Through laboratory LDA meassurements, an estimated particle–space charge is used to verify the numerical results. The comparison between the numerical results and the measurements shows close agreement.

A numerical method is developed to investigate the back corona phenomena. The back corona phenomena occur when the dust layer–phase conductivity becomes lower than the gas phase conductivity and causing an accumulation of charges at the surface of the dust layer. The numerical results show a qualitative agreement with the predicted physical behavior. Furthermore, the calculations show that the dust layer thickness does not have any influence on the back corona, but this may also be examined for the case when the dust layer assumes to be porous of a gas–dust phase composition.

As it is mentioned before, the amount of the corona onset in numerical calculations must be determined from experimental data for current–voltage characteristics. In order to make the calculations independent of experimental data, the following relationships for balance between the imposed potential, the current density, and the corona discharge at the emission electrode are established:
There is a linear relation between the corona space charge and the current density at collector plate for negative corona discharge and there is another linear relation between the corona space charge and the onset potential for positive corona discharge. Furthermore, assuming the gas mobility to be constant at the corona point, the linear relationship between the corona space charge and current density for negative discharge will limit the electric field at the discharge point.
Since these linear relationships for the negative as well as the positive corona discharge have not been known before, further investigation is needed from a microscopic point of view to explain their origin.

The influence of electrode spacing on corona space charge is examined on the "Fibulax" electrodes. The results show decreasing corona discharge and current density at the collector plate with decreasing electrode spacing. But, this result may not be the general behavior of the system, since the experimental data for current–voltage characteristics indicates that there is an optimum electrode spacing for which the current density at collector plate becomes maximum.

For further improvement of this numerical program the following activities should be performed:

1— In order to make the calculations independent of experimental data, the corona discharge and corona start potential may be modeled mathematically from a microscopic point of view. This should refer to further investigations on the relations between the corona space charge, current density and applied potential for both positive and negative corona discharge.

2— Investigation of the gas mobility variations due to temperature, humidity, chemical compositions, plasma state, etc.

3— Further investigation of the back corona phenomena in relation to dust resistivity and current density.

4— Investigation of the influence of electrode spacing, tuft corona spacing, collector plate with baffles, and other geometrical configurations on the induced current density.

7 Electro–fluid–dynamics of ESP

The transport of particles inside the ESP is governed by both the gas flow and the electrical forces on charged particles. These are the main mechanisms in precipitation processes and should be given particular attention.

The flow field inside ESP is influenced by both the electrodynamics of ionized gas under the effect of electric field and the geometrical configurations. The nonuniform electric field between the emission electrodes and the collector plate acts on ionized gas causing deformation of the flow field, inducing secondary flows and turbulence in the bulk.

The creation and the stability of electrodynamic flows depends on the electrical Froude number, the ratio of fluid inertia to electrical forces, [8] and [62],

$$\mathrm{Fe} = \frac{1/2\ \rho_f\ U_0^2}{(J_m/b_i)\,d}\,. \tag{7.1}$$

Here, ρ_f is the gas density, U_0 the axial bulk velocity, J_m the mean current density, b_i is the ion mobility, and d the electrode to collector distance.

It is found that the appearance of secondary flows depends strongly on the magnitude of this number and becomes significant when the Froude number is less than 2.0, [8]. Larsen [62] has investigated the nature of secondary flows in negative tuft corona discharge with CA–100/100 electrode collector geometry (fig. 6.12 and 7.1) concluding that the ordered secondary flows of axial vorticity depends on the polarity and the geometry of wire electrodes. Furthermore [50] has investigated the development of axial rolls analytically, numerically and experimentally concluding that the ordered axial rolls will break down after getting fully developed and after the kinetic energy associated with rolls dissipates in form of turbulent velocity fluctuations. The secondary flows and the induced turbulence due to these have a strong influence on particle transport in ESP (see [1] to [10] and [35]), hence the influencing parameters must be investigated.

The following sections concern experimental and numerical investigations of the electric field influence on the ionized gas flow, the turbulence production, and the charged particle motion using a model ESP of laboratory scale.

The measurments are performed on CA–100/100 and Fibulax electrodes with geometrical configurations shown in fig. 7.1 and fig. 7.2.

It should be mentioned that, the CA–100/100 electrodes have been used only in laboratory investigations [62], [64], and [66] while Fibulax electrodes are widely being used in commercial ESPs [53].

7.1 Measurements on laboratory scale ESP

The experimental facilities concerning the channel construction and flow characteristics has already been explained in chap. 6, therefore it will be sufficient to give a short explanation on LDA–facilities.

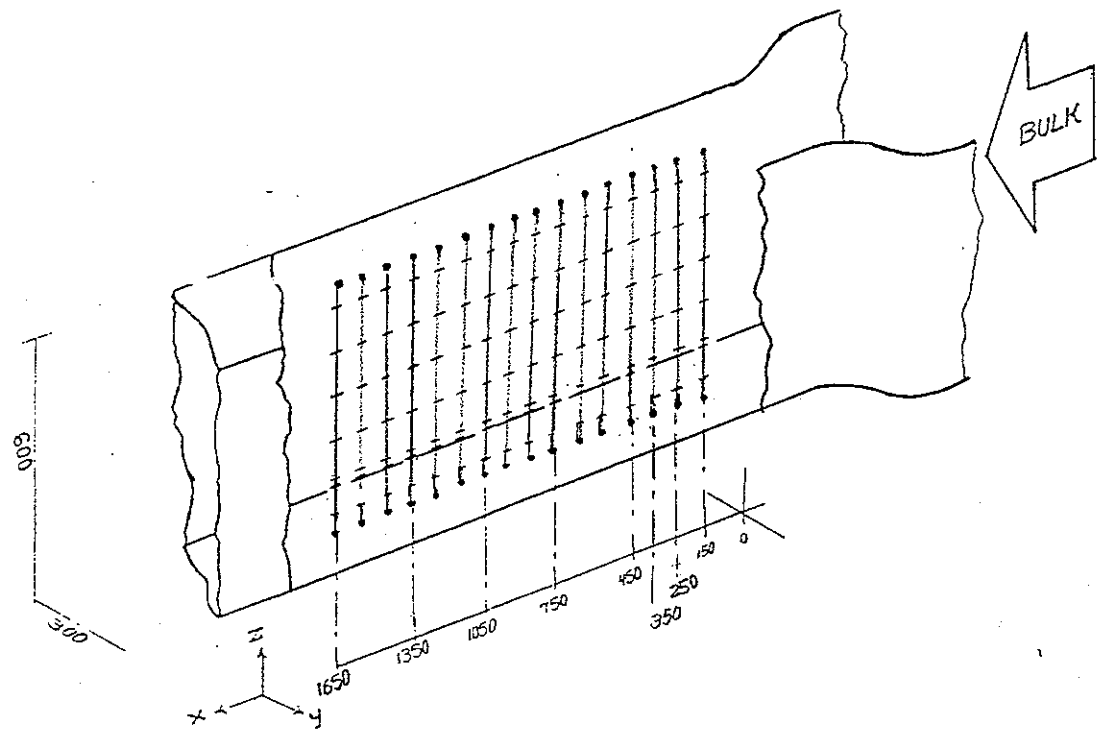

Fig. 7.1 The electrode—collector configuration in labratory scale ESP for CA—100/100 electrodes.

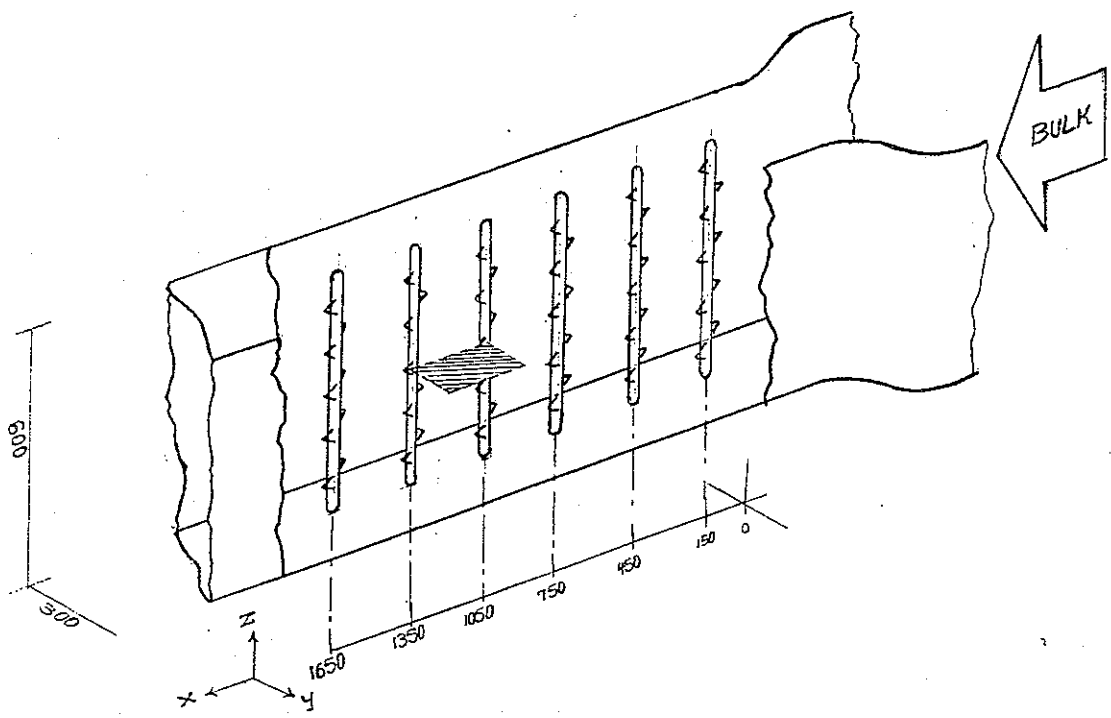

Fig. 7.2 The electrode—collector configuration in labratory scale ESP for Fibulax electrodes.

7.1.1) LDA–facilities

An LDA–system, including a two–color spectra physics 165–03 argon–ion laser and a DISA 55x modular optical unit, is used to obtain axial and transversal velocity components of seeding particles. A frequency shifter combined with a 40 MHz Bragg cell allows for measurement of both negative and positive velocities. Bias–free residence–time averaged first and second moments of velocities with an estimated uncertainty of 2% and 5%, respectively, are calculated. The LDA–optics are placed on a rigid traversing bench, allowing for three–dimensional positioning of the measuring volume. Aerosol particles generated by atomizing glycerin serve as seeding particles. Mean aerodynamic diameters of 1.2 μm for the aerosol particles are found using an INSITEC Particle Conter Sizer Velocimeter, see App.C.

7.1.2) Measurements with CA–100/100 electrodes

The LDA measurements with CA–100/100 electrode geometry reveal secondary flow of axial rolls when the Froude number becomes smaller than the critical value ($Fe < 2.0$), fig. 7.3. The secondary flows of axial rolls may be detected by traversing in vertical direction in between the electrodes and the collector plate. Figure 7.4 shows the variation of axial roll strength in flow direction at the level of corona tufts. Due to geometrical symmetry conditions, the axial rolls are periodic in vertical direction with alternating vorticity direction. As it can be seen from fig. 7.4 the roll strength (maximum transversal velocity component) decreases after it becomes fully developed and at the same time the turbulence level begin to rise. The turbulence level reaches maximum after the roll strength begins to break down and it becomes constant while the rolls strength undulates to a lower value.

Figure 7.5 shows the vertical traversing in six different axial positions. As it can be seen, the flow continuity will be satisfied within each roll if the zero line were moved to the right by about 0.1 m/s for all the cases. This discrepancy in flow continuity is caused by the particle electrical drift velocity toward the collector plate which will be discussed later.

7.1.3) Measurements with Fibulax electrodes

The measurements with Fibulax electrodes are performed downstream after the fourth electrode at the plane shown cross–hatched in fig. 7.2.

Figure 7.6a and 7.6b show the velocity vector plot for Fibulax electrodes at zero and 50 kV potential levels with a bulk flow of 1.0 m/s. Comparision of these figures indicates a deformation of the flow field due to electric forces which act on the ionized gas and the charged particles.

The vertical traversing in two different axial positions shown in fig. 7.7 indicates that the axial vorticity field of electrical forces does not generate regular axial rolls of secondary flows. But, there are some transversal deformations of the flow field which may have a spatial three dimentional patterns. These three dimensional patterns are discussed by [18], [63] and [64], and will be discussed in the next section.

The turbulence sources in ESP are discussed by [19], [46], and [50], where [50] concludes that the space charge fluctuations have minor influence on generation of turbulence compared to what velocity gradients due to secondary flows generates. Furthermore, [50] concludes that the flow turbulence in absence of secondary flows stem from the electrical production and the vorticity due to boundary layer formation at the

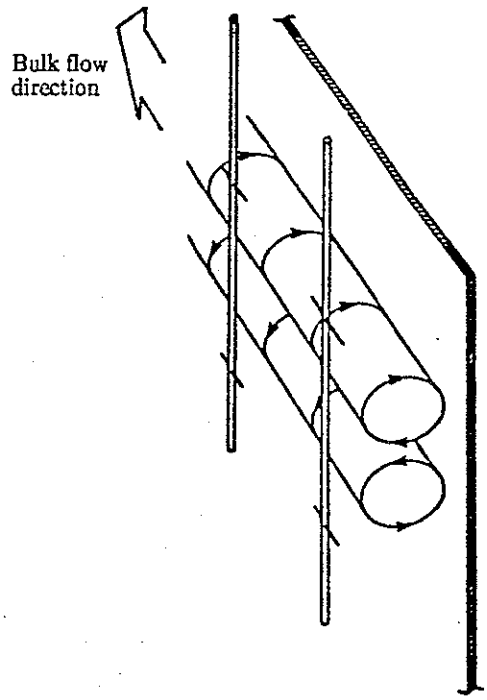

Fig. 7.3 Illustration of axial rolls generated by CA—100/100 electrodes with alternating sign. The gas moves toward the plates at level of pins and away from the plates between pins.

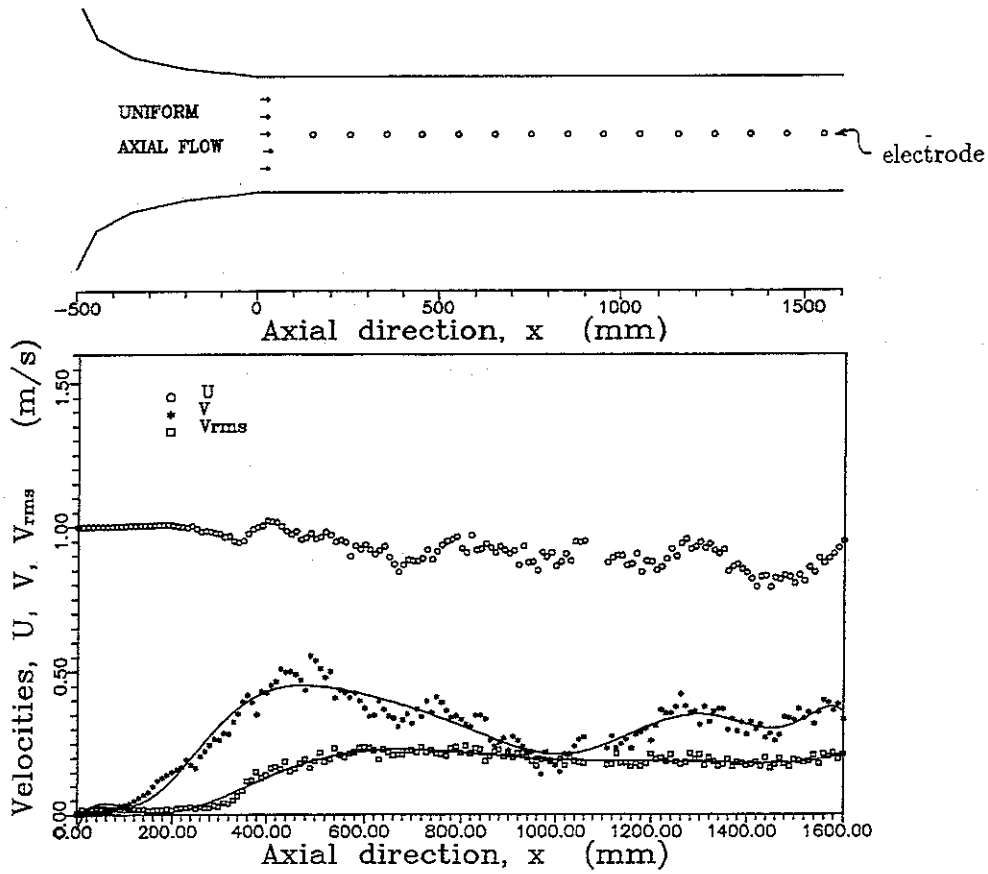

Fig. 7.4 The axial roll strength and the generated turbulence intensity history (lower figure) with CA—100/100 electrode—collector configuration (upper figure).

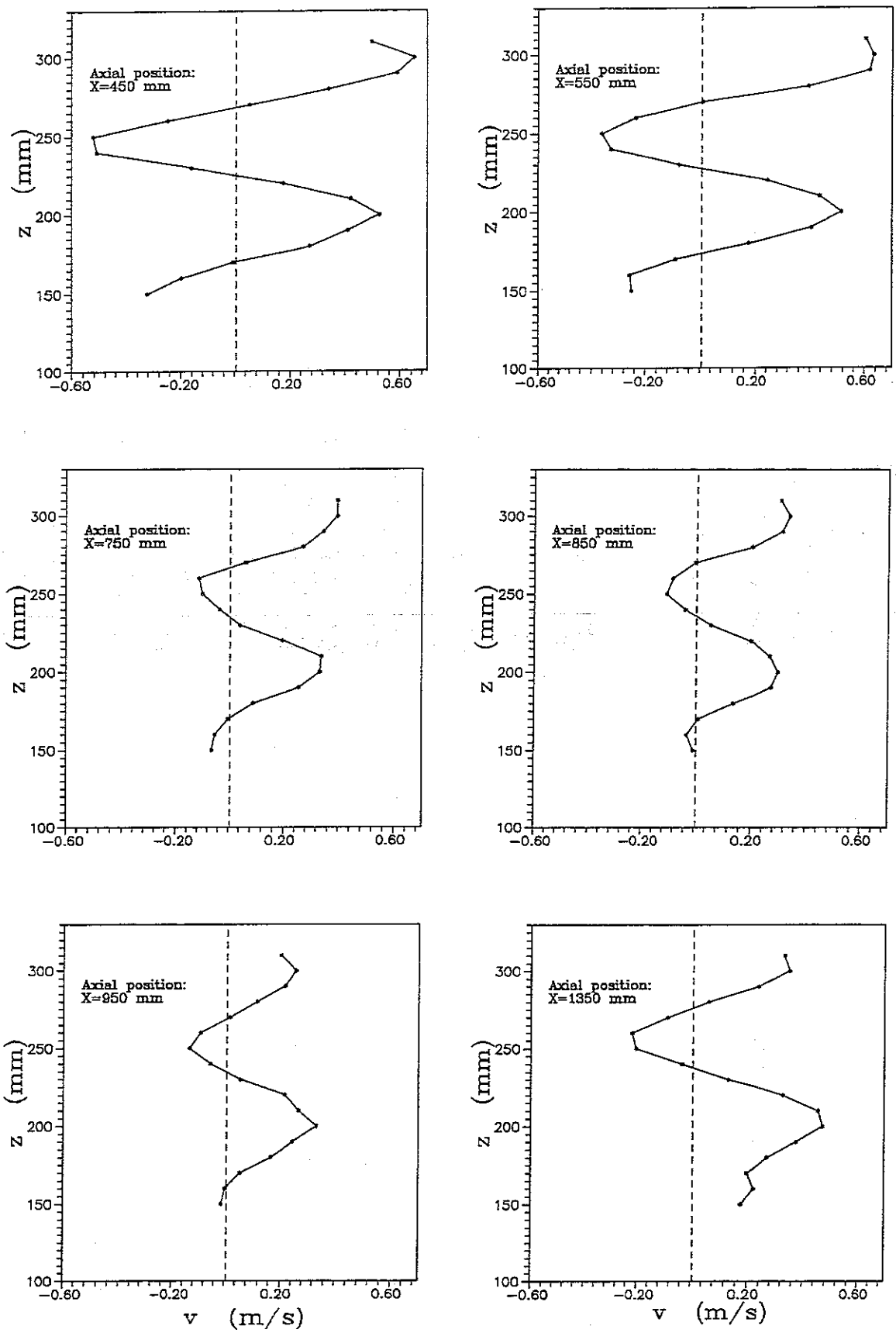

Fig. 7.5 The vertical veriation of axial roll strength within three unit of symmetry in six different axial posisions.

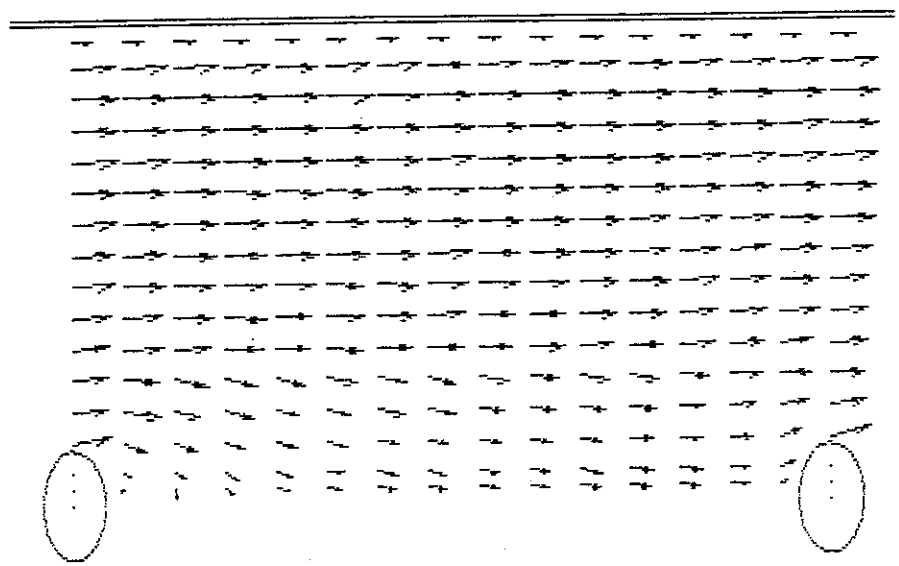

a)

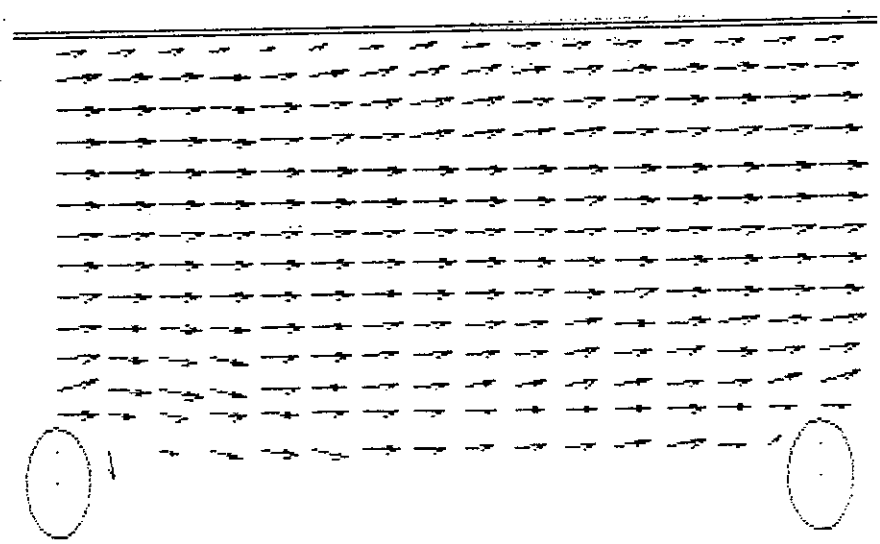

b)

Fig. 7.6 Illustration of measured velocity field for Fibulax electrodes at the horizotal plane indicated cross–hatched in fig.7.2. The imposed voltage on electrodes, a) 0 kV, b) 50 kV.

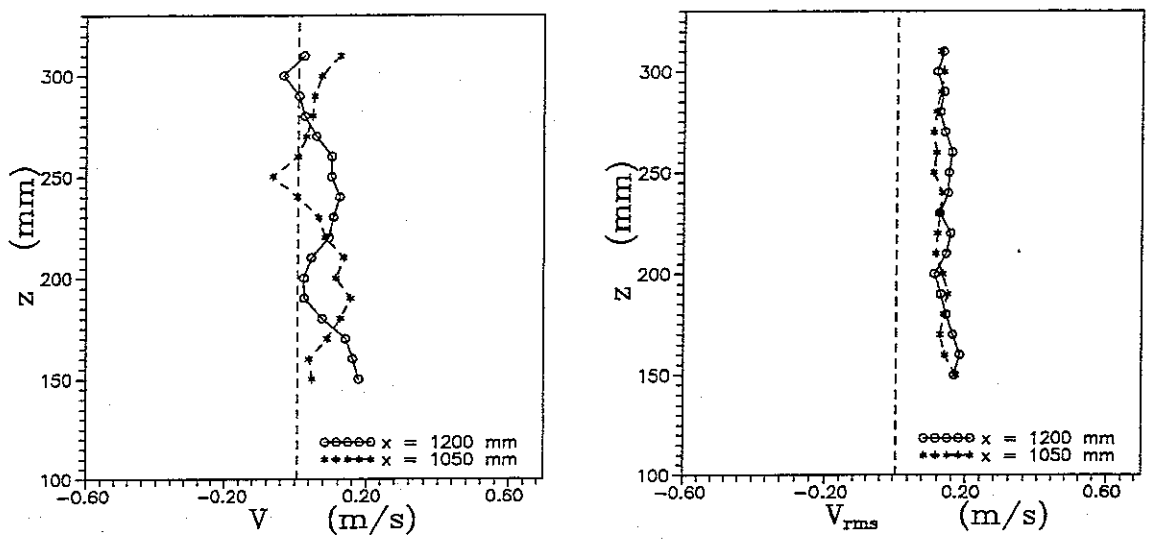

Fig. 7.7 The vertical variation in transversal velocity and turbulence intensity for Fibulax electrode (U_0 = 1.0 m/s , φ_0 = 50 kV) within three vertical units of symetry in two different axial positions, x = 1050 mm and x = 1200 mm (y = 75 mm). This positions are indicated in fig. 7.2.

collectig wall and the wake behind the electrode body.

Figure 7.8 shows the turbulence levels associated with particle velocity fluctuations between the electrodes and the collector plate for two cases with zero and 50 kV imposed voltage. According to these experiments there is no significant increase in the turbulence level when the system is imposed by a potential of 50 kV. This may be explained by the fact that the Fibulax electrodes do not generate any significant form of secondary flows which may induce vorticity sources in the bulk, and therefore the turbulence level keeps low. Furthermore, these figures show that the turbulence is not homogeneous for u and v–momentum and, as it is expected, the level of turbulence is maximum behind the electrodes for both cases.

The turbulence level for u–momentum becomes quite low at a distance of 30 mm from the collecting wall and then begin to rise as it nears the wall due to growth of the boundary layer in the mean flow.

Figure 7.9 shows the measurements of probability density distribution of transversal velocity fluctuations of particles at three different distance from the collecting wall. The purpose of this experimet is to detect the negative particle flux from the wall back into the bulk flow. The negative particle flux occurs when precipitated particles re–enter into the mean flow. However, these measurements do not indicated any negative flux for liquid seeding particles. The re–entrainment of solid particles due to back corona and other electrical phenomena is an actual problem which has been reported [53].

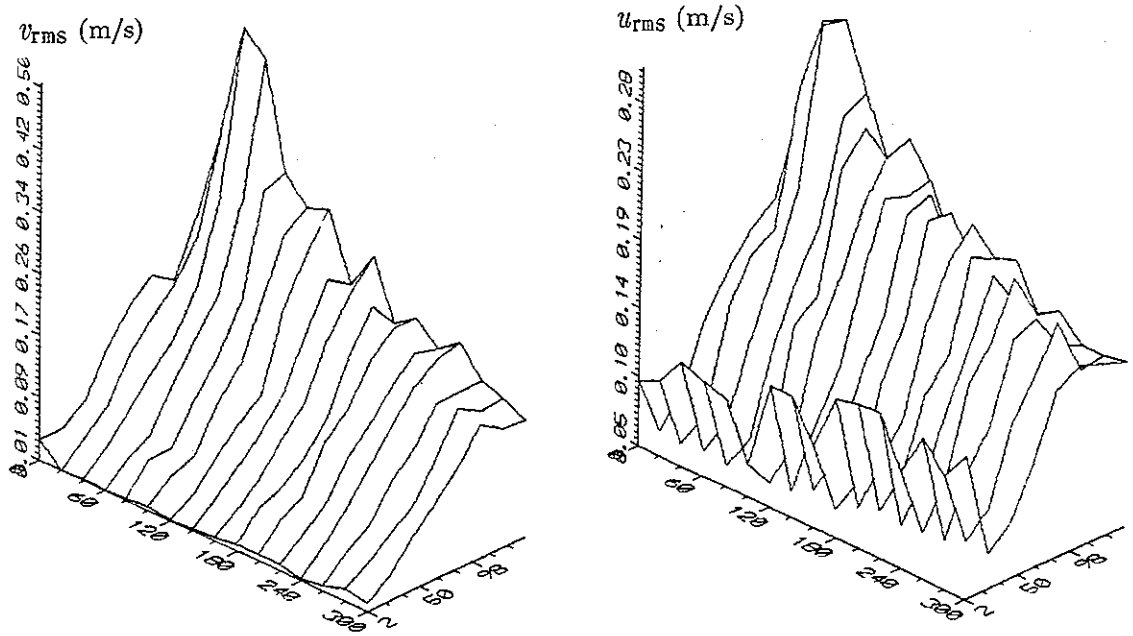

a)

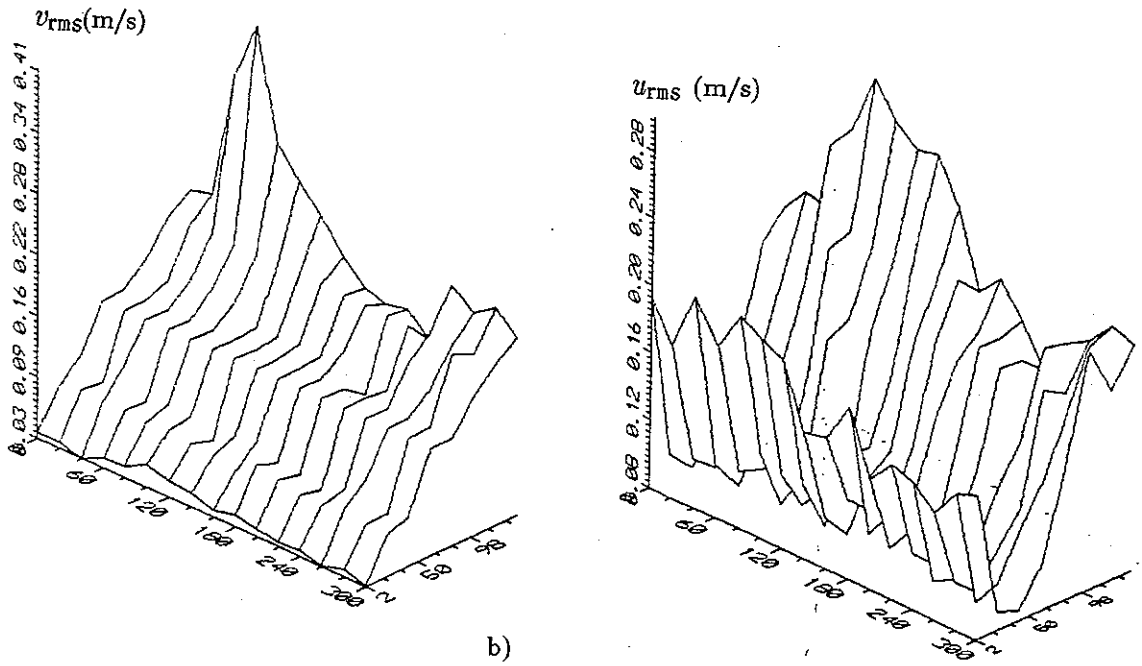

b)

Fig. 7.8 The turbulence intensity variations between two electrodes at the horisontal plane indicated cross–hatched in fig.7.2. a) 0 kV, b) 50 kV.

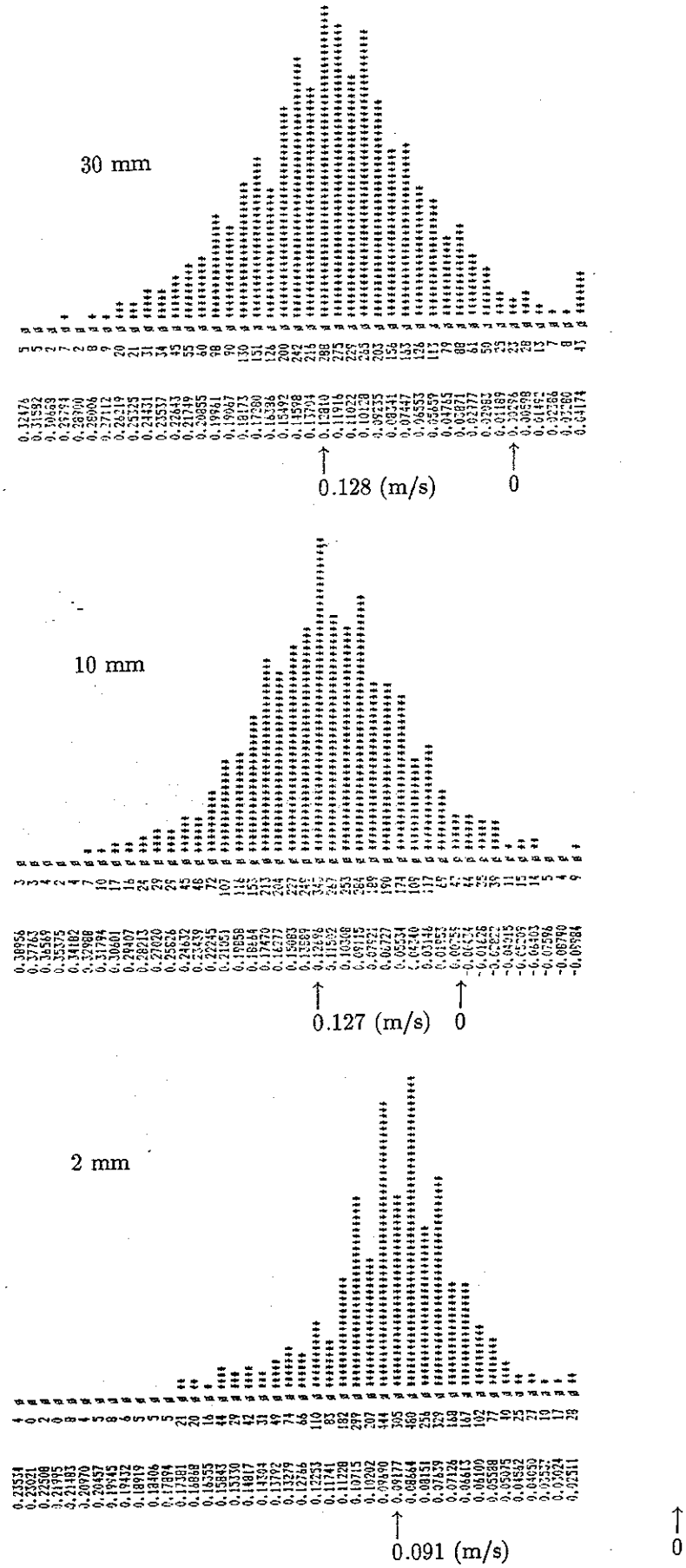

Fig. 7.9 The measured probability density distributions of particle transversal velocity at three different distances, 30, 10, and 2 mm from the collecting wall.

7.1.3) Interpretation of LDA–data

A) Velocity

Particle motion inside the ESP is dominated by both the particle inertial, viscous forces, and the electrical Coulomb forces between the charged particles and the induced electric field,

$$\mathbf{v}_p = \mathbf{v}_f + \mathbf{v}_e \,, \tag{7.2}$$

where $\mathbf{v}_p$ is the particle velocity, $\mathbf{v}_f$ is the fluid velocity and $\mathbf{v}_e$ is the electrical drift velocity of the particle relative to the fluid, assuming the turbulent diffusion velocity to be negligible.

Since the LDA–data represents the velocity of seeding particles, the electrical drift velocity of particles must be subtracted from the LDA–data to obtain the fluid velocity field, $\mathbf{v}_f$.

The particle electric drift velocity is defined as

$$\mathbf{v}_e = b_p \mathbf{E} \,, \tag{7.3}$$

the production of particle mobility b_p (which depends on particle size and charge [60], see also Chap. 8) and the local electric field, **E**. Furthermore, as it was defined in chap.1 the particle mobility can be calculated from

$$b_p = \frac{q}{3\pi \cdot \mu \cdot d_p} \,, \tag{7.4}$$

where q is the particle charge, μ the gas viscosity, and d_p the particle diameter.

The saturation charge measurements at 215 $\mu A/m^2$ averaged current density of particles of submicron size performed by [60] leads to the following approximation for q as a function of particle diameter,

$$q = 1.2 \times 10^{-6} \, (d_p)^{1.75} \quad [C] \,, \tag{7.5}$$

where d_p is in meter. Inserting this equation into Eq.(7.4), then (for $\mu = 18.5 \times 10^{-6}$ kg/ms) follows

$$b_p = 6.8 \times 10^{-3} \, (d_p)^{0.75} \quad [m^2/Vs], \tag{7.6}$$

By inserting the measured particle mean diameter of 1.2 μm into Eq.(7.6), the particle mean mobility, $\bar{b}_p$, becomes 2.5×10^{-7} m^2/Vs. Inserting this value into Eq.(7.3) and employing the electric field of fibulax electrodes from the calculations in the foregoing chapter, then the result will be the electrical migration velocity field for a particles of 1.2 μm in diameter shown in fig.7.10a. Now, it is possible to obtain the fluid velocity field from $\mathbf{v}_f = \mathbf{v}_p + \mathbf{v}_e$.

Fig.7.10b (same as fig.7.6b) shows the velocity vector plot of LDA–data of seeding particles (at the plane shown cross–hatched in fig. 7.2), and fig. 7.10c shows the resulting fluid velocity field $\mathbf{v}_f$ of the same plane, obtained by subtracting data of fig. 7.10a from those of fig. 7.10b.

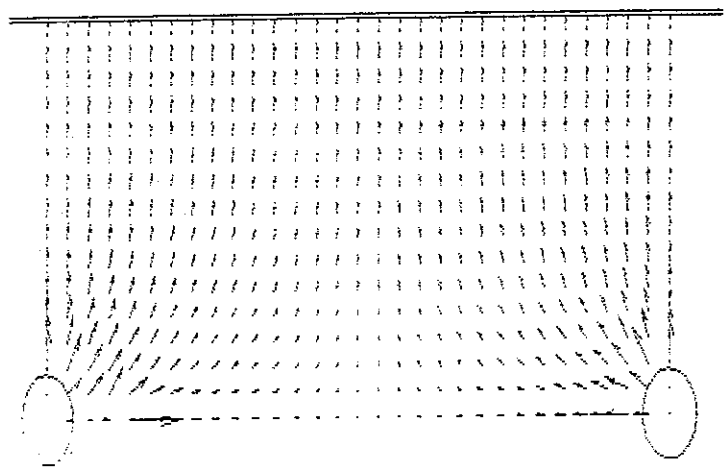

a)

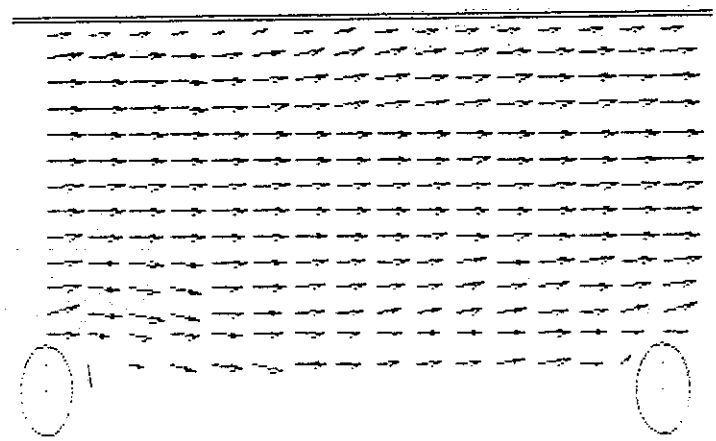

b)

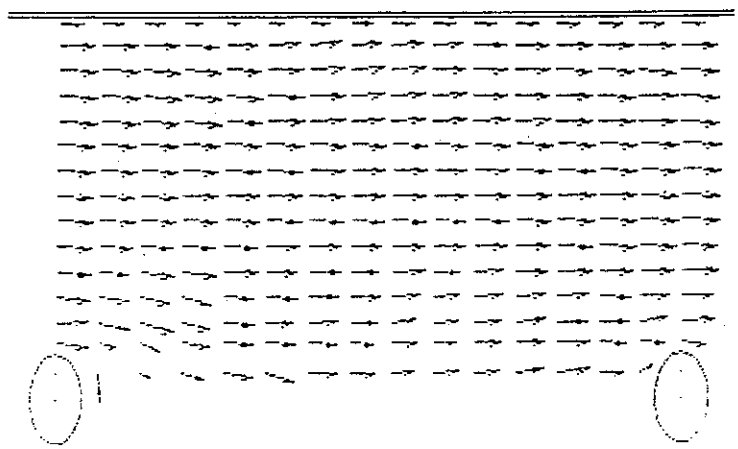

c)

Fig. 7.10 Result for periodic unit cell of horizontal cross–hatched plate shown in fig.7.2. Case of 50 kV.
a) Particle derift velocity vector field v_e (largest arrow equals 0.5 m/s), computed from electric field for 2.5 μm dia. particle.
b) Experimental velocity vector field of seeding particles by LDA.
c) Resulting velocity vector field of gas motion, from (b)–(a), (largest arrow in b and c equals 1.17 m/s).

B) Turbulence

The turbulence fluctuations of particles of submicron size stem from the fluctuating motion of the fluid and the fluctuating electric drift velocity due to changes in particle mobility,

$$\mathbf{v}'_p = \mathbf{v}'_f + \mathbf{v}'_e \,, \tag{7.7}$$

where $\mathbf{v}'_p$, $\mathbf{v}'_f$, and $\mathbf{v}'_e$ denote the fluctuating parts of the mean values.

The changes in particle mobility depend on particle diameter (Eq.(7.6)), therefore particles with different size have different electrical drift velocity in the measuring volume and these velocity fluctuations will be precived as turbulence by the LDA–system [51]. This is a kind of false turbulence additional to the turbulence due to the fluid velocity fluctuation. In order to find the magnitude of it, the following estimation can be performed:
statistically the rms velocity may be defined as,

$$\mathbf{v}'_e = | \, \overline{\mathbf{v}}_e - \mathbf{v}_{ej} | \quad , \tag{7.8}$$

where $\mathbf{v}_{ej}$ is the insantaneous value of velocity.

Inserting Eq.(7.6) and Eq.(7.3) into Eq.(7.8), then gives

$$\mathbf{v}'_e = | \, 6.8 \times 10^{-3} E_y \, (\overline{d}_p^{\,0.75} - d_{pj}^{0.75}) \, | \,. \tag{7.9}$$

here $\overline{d}_p$ and d_{pj} are the mean value and an arbitrary value of particle diameter in the measuring volume. Furthermore, the particle diameter statistically may be defined [31] as,

$$d_{pj} = \overline{d}_p \pm \sigma_s \,, \tag{7.10}$$

where σ_s is the square root of the variance of particle size distribution function. Assuming that the size of particles are Gaussian distributed, σ_s is defined as

$$\sigma_s^2 = \int_0^\infty (d_{pj} - \overline{d}_p)^2 \, \frac{1}{\sqrt{2\pi}\,\sigma_g} \, e^{-(d_{pj} - \overline{d}_p)^2 / 2\sigma_g^2} \, d d_{pj}, \tag{7.11}$$

which is the "erf" distribution function with following solution

$$\sigma_s^2 = 0.5 \, \sigma_g^2 \,, \tag{7.12}$$

where σ_g is the geometric standard deviation of the particle size distribution.

According to measurements in appendix C, the particle mean diameter, $d_{50\%}$ is 1.20 μm and $d_{84.1\%}$ is 1.45 μm where the geometric standard deviation may be found as

$$\sigma_g = \frac{d_{84\,.\,1\%}}{d_{50\%}} = \frac{1.45}{1.20} = 1.208 \,. \tag{7.13}$$

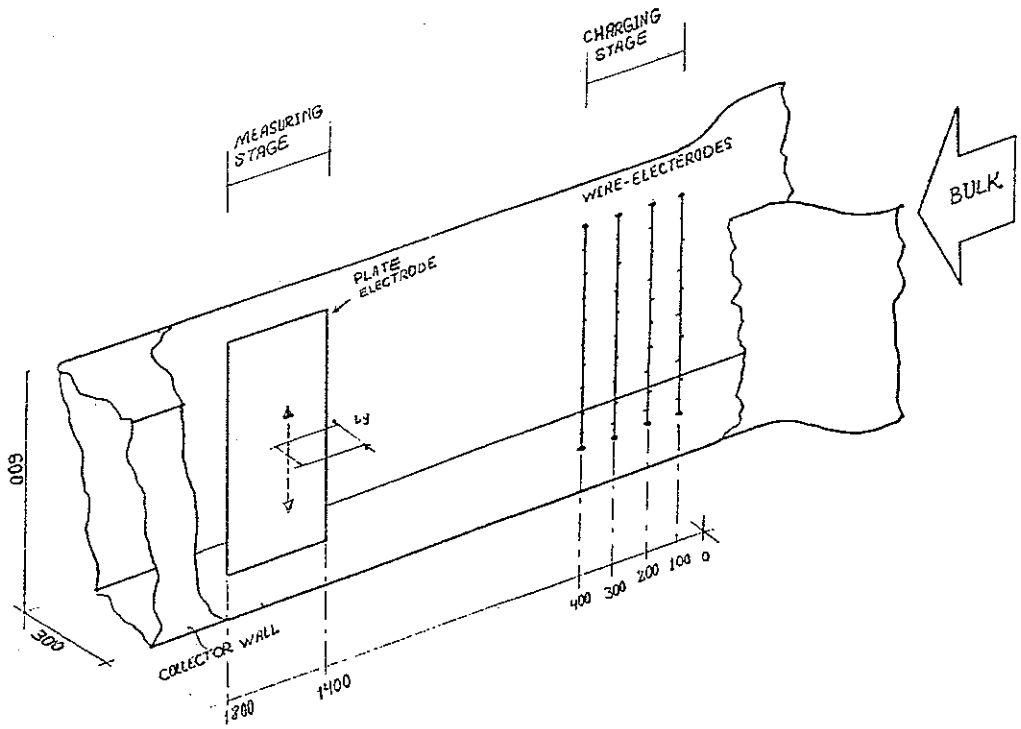

Fig. 7.11 Two stage precipitator with four charging electrodes spaced 100 mm apart a distance of 1000 mm upstream and a smooth plate–electrode parallel to the collector wall. These two stages are kept at the same D.C. potential and the bulk flow is 1.0 m/s.

Inserting this value into Eq.(7.12 to 7.9), the false velocity fluctuation becomes, $v'_e = 0.029$ and 0.041 m/s, for uniform fields of 2.4 and 3.3 kV/cm respectively. Hence, the false turbulence due to particle size has small influence on turbulence level and this may also be confirmed by experiments. To demonstrate this fact, it is arranged a two stages ESP consisting of a charging field by the inlet of the channel and a known uniform electric field between a plate–electrode parallel to collecting wall, 1.0 meter downstream for the charging stage, see fig. 7.11. These two stages are connected to the same energy source, so if there will be any increase in turbulence intensity at the second stage with the uniform electric field, then it may be detected by removing the plate electrode and doing the measurements at the same place again.
The measurements are made exactly at $l_y/2$, between the plate–electrode and the collector wall, since simple analytical analysis (appendix.D) shows that at this region the influence of space charge due to particle charge on the electric field is eliminated and the electric field equals the ratio of imposed potential to the distance between collecting wall and the plate, φ_0/l_y. Furthermore, the measurements are performed in different vertical positions in order to eliminate the influence of any transversal deformation of the flow field downstream of the charging stage. Referring to these measurements shown in fig. 7.12, then it can be concluded that there is no significant change in turbulence level caused by particle size changes in the measuring volume of the LDA–system. Figure (7.13) shows the measured electrical drift velocity of particles in the uniform electric field. The result of these measurements suggests a mean particle mobility of $\overline{b}_p = 4.17 \times 10^{-7}$ m^2/Vs. Inserting the experimentally found value for $\overline{b}_p$ into Eq.(7.6), the mean particle diameter may be estimated to $\overline{d}_p = 2.4$ μm. The discrepancy between the estimated and the measured particle middle diameter may be explained by the fact that the present LDA–system is not able to detect the signals coming from the particles under a certain size, hence the distribution function for the measured particles by LDA–system is not gaussian distributed and therefore the mean particle diameter becomes larger since the contribution of small particles is not detected.

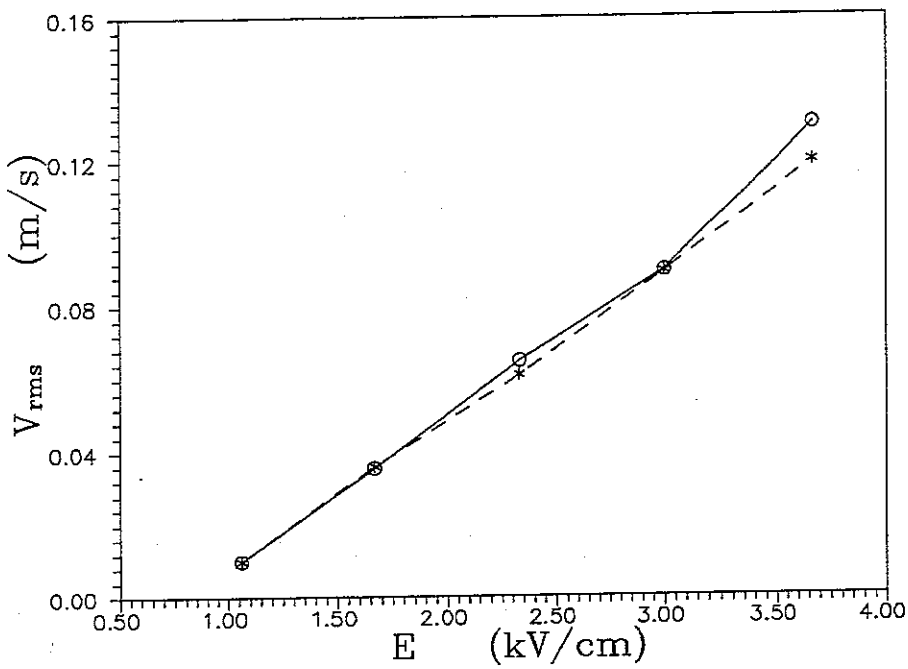

Fig. 7.12 Rms of transversal component of velocity of seeding particles versus field strength measured by LDA in the uniform electric field at the line of symmetry midway between 0.4 m long electrode—plate at centerline and side wall.
Particles charged by corona discharge from barbed wire electrodes upstream, at same voltage as plate. Corona ignition at 1.08 kV/cm. — — — — with plate,———— without plate.

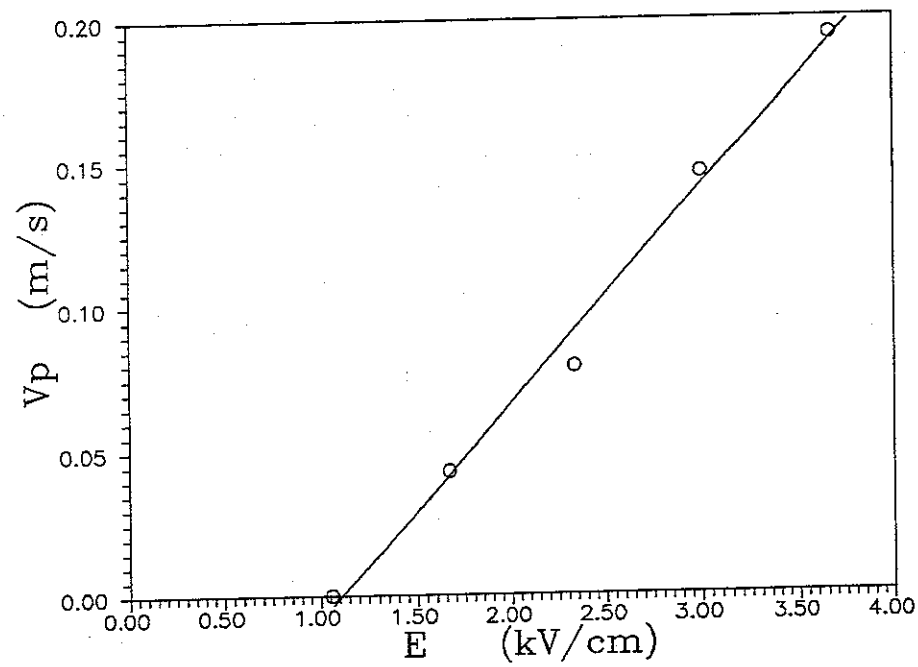

Fig. 7.13 Drift velocity of seeding particles versus field strength measured by LDA in the uniform electric field at line of symmetry illustrated in fig.7.12. Particles charged by corona discharge from barbed wire electrodes upstream, at same voltage as plate. Corona ignition at 1.08 kV/cm.

7.2 Numerical calculation of flow arrangement

The flow field in negative tuft corona discharge may have three dimensional patterns due to the nonuniform electric field inducing vorticity sources of complex three dimensional structures. In this part the numerical calculations of the flow field for CA–100/100 and Fibulax electrodes will be explained and the results will be discussed and compared to the measurements from the foregoing section.

7.2.1) Calculations on CA–100/100 electrodes

[64] considers an approximated three dimensional harmonic distribution of electrical body forces for CA–100/100 electrode–collector configuration in order to investigate the resulting three dimensional flow field due to these forces. These calculations indicate that the spatial structure of the flow field within a symmetrical cell (fig. 7.14 and fig. 7.15) strongly depends on the imposed bulk flow, and hence the magnitude of Froude number, Fe.

The vortex structure at zero bulk is illustrated in fig. 7.16. As it has been discussed by [50], the turbulence level directly depends on the surviving and the stability of these vortex structures in bulk flow. This may be supported by the experiments shown in fig. 7.17 where the turbulence level depends on both bulk flow and the imposed voltage on the system. The Froude number increases by increasing the bulk flow, hence the secondary flows disappear and the turbulence level decreases.

7.2.2) Two dimensional flow solver (TEACH–Z)

At Fe >> 1, the three–dimensional numerical simulations show a regular pattern of secondary flow in form of axial rolls identical to experimental data in fig. 7.3 and fig. 7.4. These regular rolls of axial vorticity have also been reported by [65] and [50] and many others at AFM, Technical University of Denmark. Furthermore, the calculations of vorticity fields of electrical body forces indicate that the axial component is the strongest ($\Omega_x = 72$, $\Omega_y = -39$, $\Omega_z = 42$ N/m^4). Therefore, for further investigations, a two dimensional flow solver computer–code (Teach–Z) has been adopted to verify the influence of axial vorticity on the development of axial rolls.

The code solves the incompressible time–averaged Navier–Stokes equations using finite volume discretization method [68] where the PISO algorithm relates the mass conservation to the pressure correction equation in determination of the pressure field [69].

The electrical body forces in yz–plane (the plane containing the recirculating region) come from the three dimensional calculations of the electric field and the space charge field for CA–100/100 electrodes from the foregoing chapter. These forces are integrated in axial direction and then the averaged values have been used. There is fully slip conditions at the collecting wall and symmetry conditions at the other boundaries. This has been justified elsewhere [62].

Figure 7.18 shows the calculated results for the recirculating flow field of axial vorticity with maximum roll strength of 0.33 m/s estimated through assumption of constant eddy diffusivity, $\nu_\tau = 50 \times \nu$. This magnitude of roll strength is the same as measured value for fully developed rolls 1.5 m downstream of the channel (see fig. 7.4).

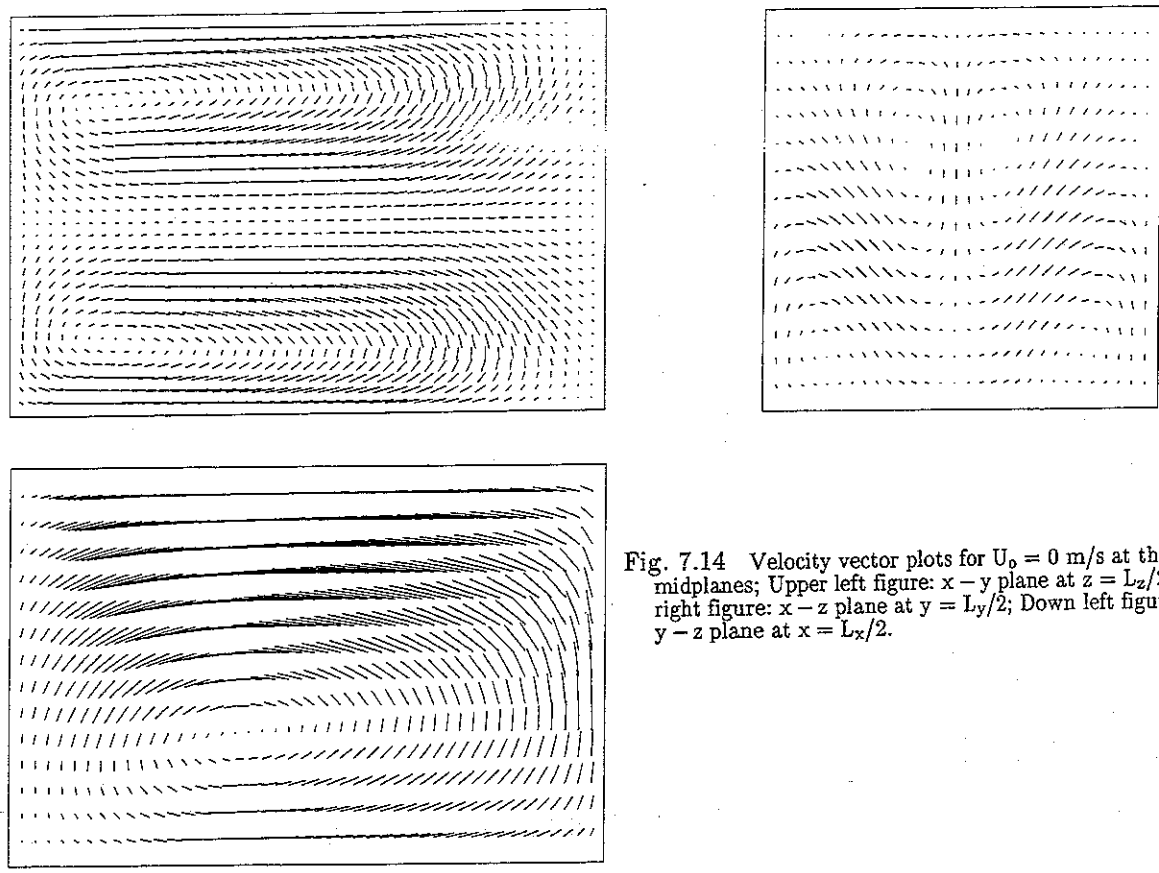

Fig. 7.14 Velocity vector plots for $U_o = 0$ m/s at the three midplanes; Upper left figure: $x - y$ plane at $z = L_z/2$; Upper right figure: $x - z$ plane at $y = L_y/2$; Down left figure: $y - z$ plane at $x = L_x/2$.

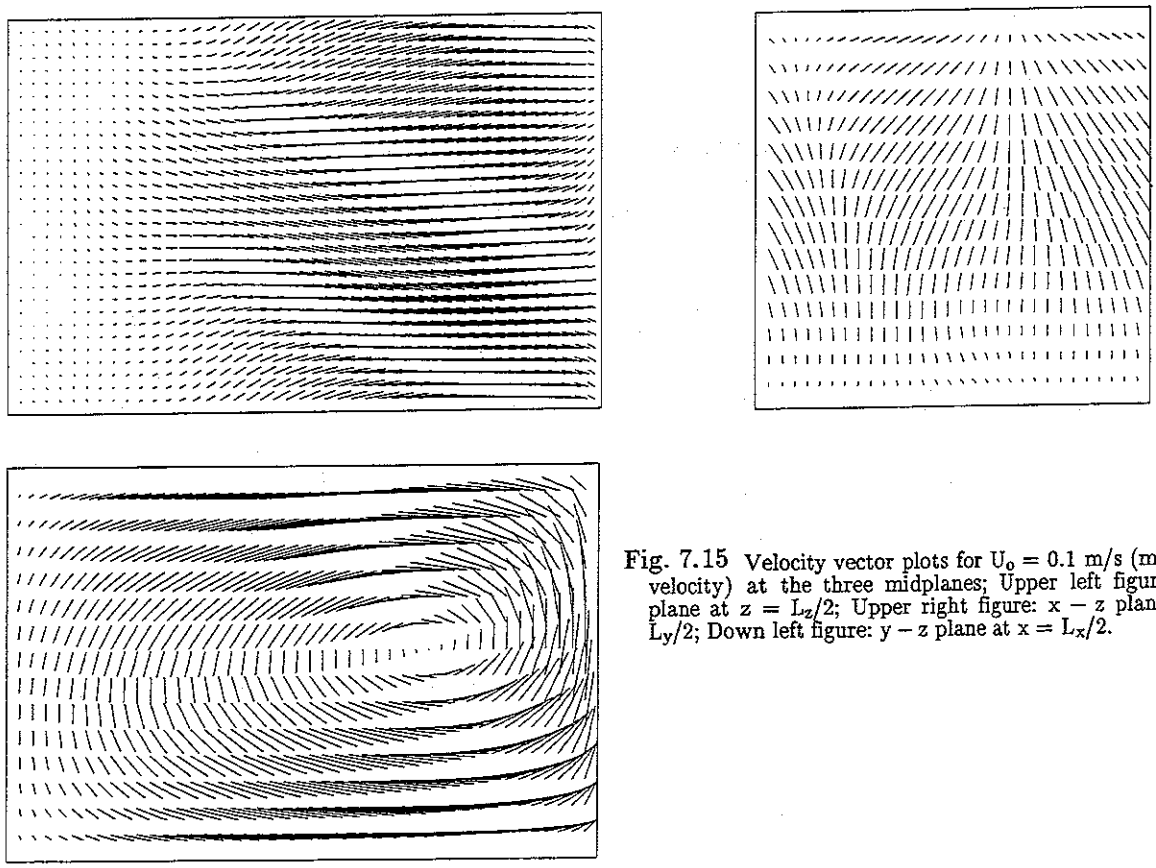

Fig. 7.15 Velocity vector plots for $U_o = 0.1$ m/s (minus bulk velocity) at the three midplanes; Upper left figure: $x - y$ plane at $z = L_z/2$; Upper right figure: $x - z$ plane at $y = L_y/2$; Down left figure: $y - z$ plane at $x = L_x/2$.

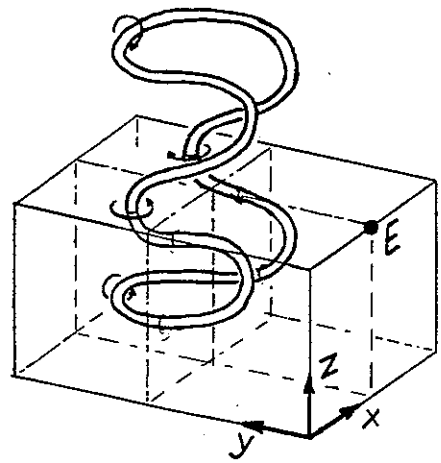

Fig. 7.16 Inferred topology of vortex structure at Uo = 0 m/s. Electrode at E.

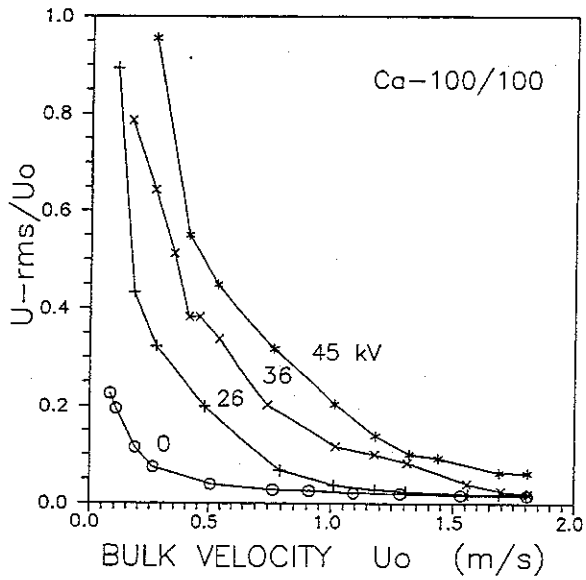

Fig. 7.17 Axial Component of rms—velocity, normalzed by bulk velocity, versus bulk velocity. All data from same point inthe flow, at four values of electrical field, 0, 26, 36, 45 kV.

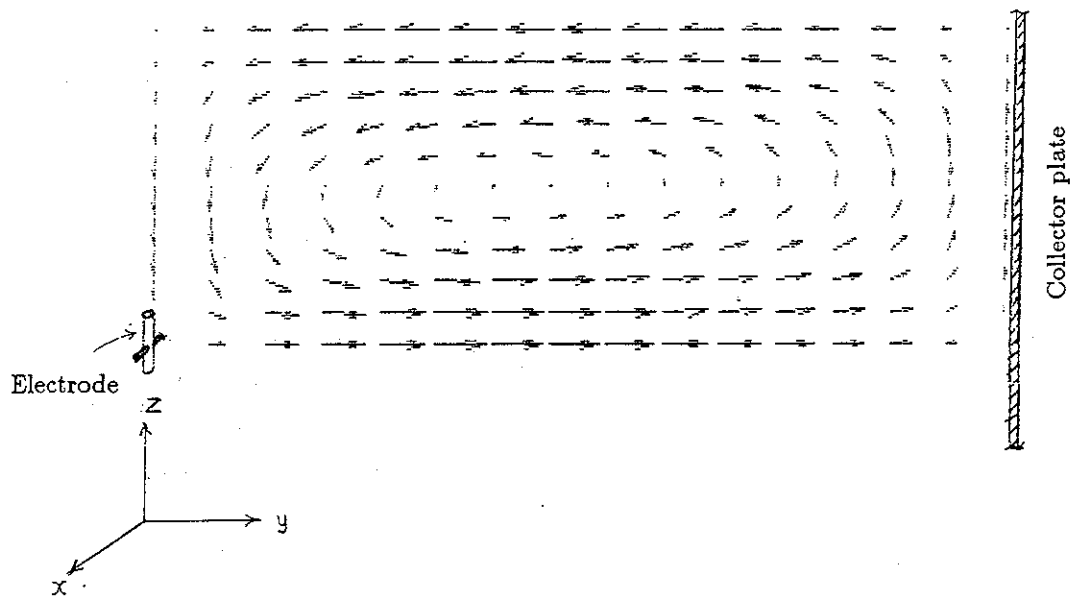

Fig. 7.18 Velocity vector plot from two dimentional calculation of flow field due to axial vorticity sources in one unit of symmetry ilustrated in fig. 5.2 and 7.1.

7.2.2) Calculations on Fibulax electrodes

The Fibulax electrodes have been used in precipitation of cement dust in industrial ESPs. Therefore, it is the aim of the present study to investigate the flow arrangement and later the particle transport in ESP using the Fibulax electrodes as the emission device.

The flow measurements with Fibulax electrodes indicates that the nonuniform electric field of axial vorticity does not induce any form of axial rolls except some weak deformations of the velocity field in vertical direction. However, the calculations of vorticity fields of electrical body forces indicate that the axial and the transversal components are stronger than the vertical component, ($\Omega_x = 43$, $\Omega_y = -45$, $\Omega_z = 35$ N/m^4). The bulky electrodes generate wide wakes with significant amount of z–vorticity. This may explain why electrical vorticity sources in x and y do not derive regular secondary flows. Also, it justifies fucusing attention on the two dimensional flow field in xy–pane. So, it is enough to calculate the flow field in two dimensions at the plane containing the electrodes body and the collector plate where the electrodes body will be approximated by square profile. Furthermore, the logarithmic wall law [33] is employed to model the slip velocity near the collecting plate and the electrode body. According to this law the slip velocity near the wall may be approximated by the following equation,

$$u_{slip} = y^+ \cdot u_\tau \qquad \text{for } y^+ \leq 5 \ , \tag{7.14}$$

where $y^+ = y_w \cdot u_\tau / \nu$, y_w is the distance from the wall, and u_τ is the friction velocity defined as

$$u_\tau = \left(\frac{\tau_w}{\rho} \right)^{1/2} \ . \tag{7.15}$$

Here τ_w is the shear force at the wall defined as

$$\tau_w = \mu \cdot \frac{\partial u}{\partial n} \quad , \tag{7.16}$$

where μ is the dynamic viscosity of the fluid and n is the normal to the wall.

In order to have an estimate for y^+ the magnitude of τ_w may be found through adoption of the empirical relationship [33] between the friction factor f_m, and Reynolds number, R_e $(= U_0 d/\nu)$, where

$$f_m = 0.3164\, R_e^{-1/4} \quad , \quad 5 \times 10^3 < R_e < 3 \times 10^4 \, . \tag{7.17}$$

For $U_0 = 1.0$ m/s, $\nu = 15.7 \times 10^{-6}$ m^2/s ,and $d = 0.15$ m ,hence the Reynolds number becomes 10^4, so $f_m = 0.032$. This factor has the following relation with u_τ,

$$u_\tau = U_0 \left(\frac{f_m}{8}\right)^{1/2} \, . \tag{7.18}$$

Inserting the empirically found value of f_m into Eq.(7.18) leads to $u_\tau = 6.3 \times 10^2$ m/s hence, $y^+ = 4.0$ at a distance of 1.0 mm from the wall.

Furthermore, it is possible to employ periodic boundary conditions since both the geometrical configurations and the electric field are periodic in axial direction. When periodic boundary conditions are needed, a grid as illustrated by the cross–sectional view in fig. 7.19 is employed. This grid contains an extra plane of cells adjoining the outflow boundary which are identical with the plane adjoining the inflow boundary. The cyclic conditions are implemented in each integration by transferring the calculated values at the plane *OO* to the inflow plane *I* and those at plane *II* to the outflow plane *O*. Uniqueness of the solution is produced by adjusting the inflow and outflow velocities to a given prespecified mean velocity. Figure 7.20 shows the calculation results which may be compared with experimental data from fig. 7.6a with zero potential at the electrodes. As it can be seen from comparison of these figures, there is a reasonable agreement between the calculated and the experimental data. However the discrepancy in the magnitude of the velocities at the region between the electrodes may stem from the turbulence behind the electrode body.

Figure 7.21a to 7.21d show the calculated results for an imposed potential of 50 kV on the electrodes with $U_0 = 0.0$, $U_0 = 0.3$, $U_0 = 0.6$, and $U_0 = 1.0$ m/s. It should be mentioned that, this time, the electrical body forces are integrated in vertical direction in order to concentrate the spatial effect of the electric field at the calculation plane. As it can be seen, the nonuniform electric field causes two equal recirculating flow field of vertical vorticities up and downstream of the electrode in absence of the imposed bulk flow. These two recirculating regions disappear as the magnitude of the imposed bulk flow becomes bigger than 0.6 m/s where the Froude number also becomes bigger than 2.0, the critical value. Notice that, by increasing the bulk velocity, the recirculating field upstream of the electrode moves toward the wall and the axial velocity becomes weak next to the wall, fig.21d. This may also be confirmed by measured data from fig.7.10c. However, it may be concluded that a three dimensional flow calculation with turbulence modeling may still be necessary to achieve better agreement with the experimental data.

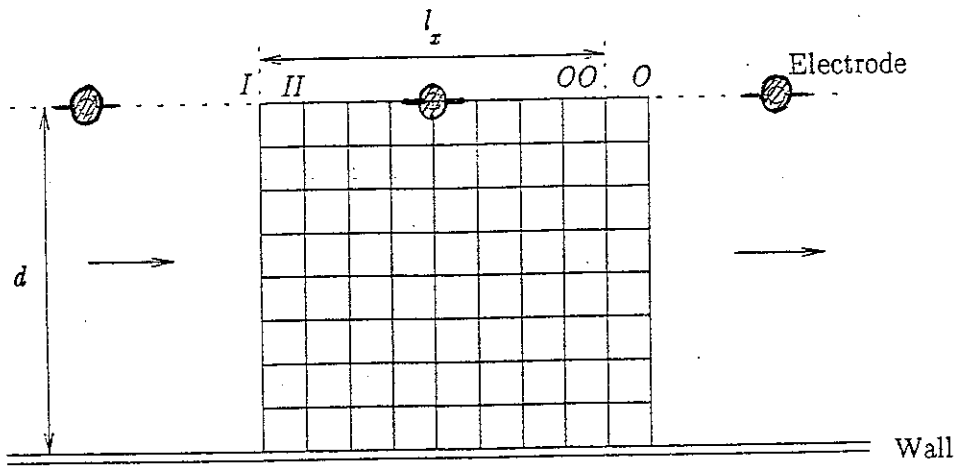

Fig. 7.19 Cross–sectional view of grid arrangement employed in connection wit periodic boundary conditions.

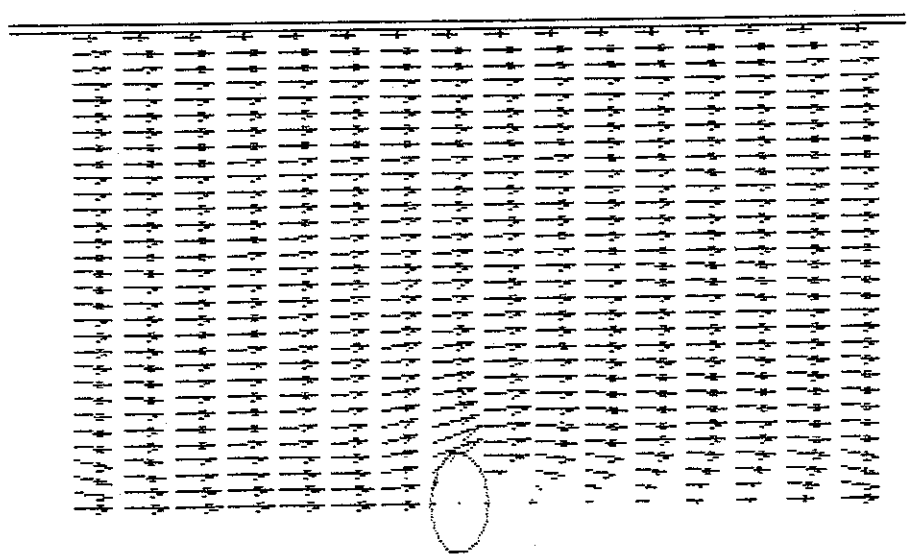

Fig. 7.20 Velocity vector plot from two dimensional calculation at horizontal plane shown cross–hatched in fig.7.2 with zero imposed potential on the electrodes.

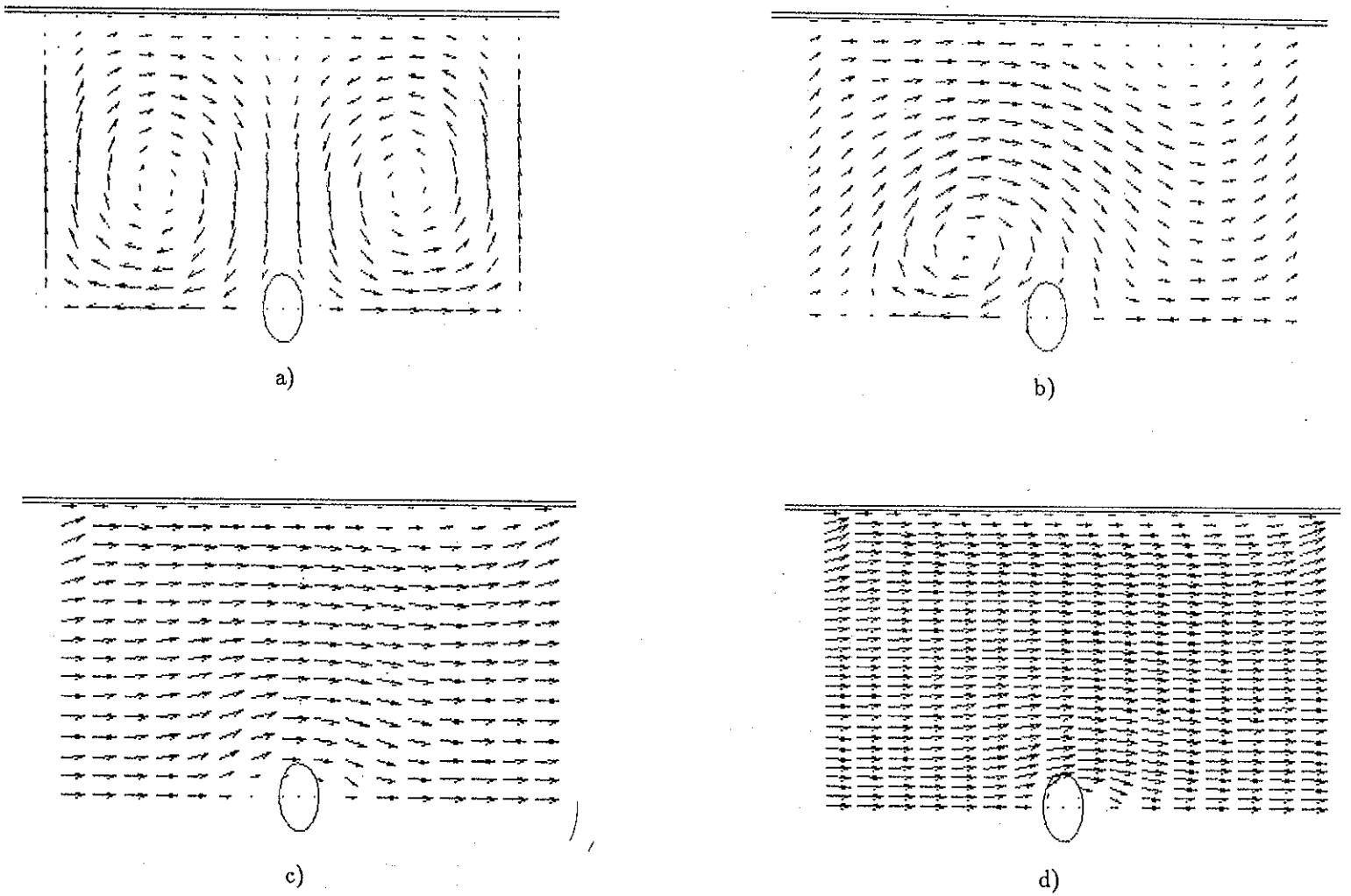

Fig. 7.21 Velocity vector plots from two dimensional calculations at horizontal plane shown by cross–hatched in fig.7.2 with 50 kV imposed potential on the electrodes, a) Uo = 0.0, b) Uo = 0.3, c) Uo = 0.6, and d) Uo = 1.0 m/s.

7.3 Conclusion and recommendations

The flow of particulate gas along the ESP is dominated by the electric field and the geometrical configurations of electrodes and collector plates. The flow patterns and the turbulence diffusion affect the spatial particle concentration which strongly influences the precipitation rate. Nonuniform electric field in drift region induces three–dimensional vorticity sources in bulk and induces secondary flows. The secondary flows may also be created by the wake behind the bulky electrodes or baffles on the collector plates. Fischer [35] has investigated the influence of the secondary flows on ESPs efficiency and he shows that the appearance of secondary flows of axial vorticity deforms the particle concentration profile which leads to reduction of the total efficiency.
The flow turbulence causes the diffusion of particles and reduces the laminar transport of particles to the collector plate, see chapter *8*. In this, the secondary flows induce velocity gradients and hence turbulence velocity fluctuations and diffusion in the bulk. Generation of secondary flows and turbulence fluctuations in ESP have been investigated by [8,19,50,62] which show that the creation and the stability of the electrodynamic secondary flows depends on the ratio of the fluid inertia to electrical forces (Froude number). Besides, the present investigation has also been concentrated on detailed experimental measurements of these electrically induced secondary flows which are necessary for establishing the flow properties. Flow properties like turbulent diffusion coefficient and the velocity near the collector plate are required in the numerical modeling of the flow arrangement in the system.

The fluctuation of the electric field and the space charge field in correlation with the velocity fluctuations give rise to additional turbulence production. But, this electrically produced turbulence is shown to have negligible influence on the level of turbulence production compared to the contribution of velocity gradients due to secondary flows. This has been investigated by [50] in details where the relationship between the turbulence level and the strength of the secondary flows of axial rolls is derived.

It has always been interesting to measure the particle reentrainment near the collector plate in order to establish the minus–flux of the already precipitated particles. Particle reentrainment as a negative effect lowers the ESPs efficiency. Therefore, in order to achieve accurate numerical results, it is necessary to establish the influence of this parameter. The LDA measurements on liquid seeding particles near the collecting wall of laboratory scale ESP shows that the minus–flux vanishes near the wall. But, this is not expected to be the case for solid particles when they reach a deposited dust layer since there may be occurring back corona, rapping or other form of reentrainment in the system.

For the present study, the electrical drift velocity of particles does not change the general flow pattern obtained from LDA measurements which, to first approximation, also describes that of the gas flow. However, for refined studies the drift velocity should always be computed and subtracted from the LDA–data to yield the velocity field of the fluid flow.

The turbulence fluctuation, whose mean is expressed as the *rms*, is a quantity which describes the discrepancy between the measured instantaneous and the mean value of the velocity field. The LDA measurements of the turbulence level in the precipitator indicate that the rising *rms* with increasing electric field strength stems from sources like, the secondary flows, velocity gradients due to the boundary layer at the collecting wall, the wake behind the electrodes, and the fluctuating electric field due to space charge fluctuations. Furthermore, according to [51] the false turbulence, due to variation of particle drift velocity in LDA measuring volume, increases the total level of

the measured turbulence. The difference between the particles electric drift velocities in an external electric field is due to variation in particle size and hence the particle mobility. These velocity changes within the LDA measuring volume will be perceived as turbulence by the LDA system. This is a kind of false turbulence additional to the turbulence from those already discussed sources. In order to obtain the magnitude of this false turbulence a method based on statically distribution of the particle size is outlined. The result of this estimation shows that the false turbulence contribution to the total measured level is ignorable.

The velocity measurements with the CA–100/100 electrodes indicate developing secondary flows (rolls) of axial vorticity. These axial rolls can also be simulated numerically with the same order of strength indicating that the magnitude of the turbulent diffusion coefficient is about 50 time the molecular diffusion. In the case where the Fibulax electrodes are used the measurements do not indicate any form of developing secondary flows, but there are some transversal deformations of the flow field which may have spatial three–dimensional patterns. The three–dimensional numerical simulations of these spatial flow patterns have not been possible due to the limited time of the present study. Therefore, the numerical treatment of the problem is based on a two–dimensional solution in a horizontally plane containing both the collector plate and the bulky electrode body. However, even though the two–dimensional calculations do not take the flow deformation in vertical direction into account, the comparison between the numerical results and the velocity measurements shows good agreement.

In order to make the flow calculations more flexible for detailed investigations of flow management, the following activities should be performed:

1– Since the calculations show that the vorticity field of Fibulax electrodes has also strong components in axial and transversal directions the flow field may have spatial patterns and should be calculated in three dimensions.

2– The measurements show that the turbulence level has strong spatial variations. These variation are proportional to the turbulence diffusion, therefore the assumption of constant turbulence diffusion in the numerical calculations may violate the results, and hence the modeling of turbulence variations may be necessary.

3– The negative–flux of solid particles due to boundary layer flow, and dust layer thickness, normal reentrainment, the and back corona phenomena must be established.

8 Particle transport and behavior in ESP

The particle precipitation inside the ESP depends on particle transport and behavior in the induced electric field and the flow field in between the electrodes and the collector plates. The charged particles, the electric field, and the flow field have strong influence on each other and the interaction between them changes the precipitation rate.

This chapter explains particle transport and behavior due to interaction between the main precipitation mechanisms inside the ESP.

8.1 Particle transport equation

As it is presented and discussed in chap. 2 and 4, the governing equation for steady particle transport consists of the convective and the diffusion terms in following form,

$$\nabla\cdot(n\mathbf{v}_p) - D\,\nabla^2 n = 0\,, \tag{8.1}$$

where n is the concentration, $\mathbf{v}_p$ is the particle velocity and D is the particle diffusion coefficient. The particle motion is influenced by the fluid motion and the electric drift velocity (chap. 7.1.3), $\mathbf{v}_p = \mathbf{v}_f + \mathbf{v}_e$.

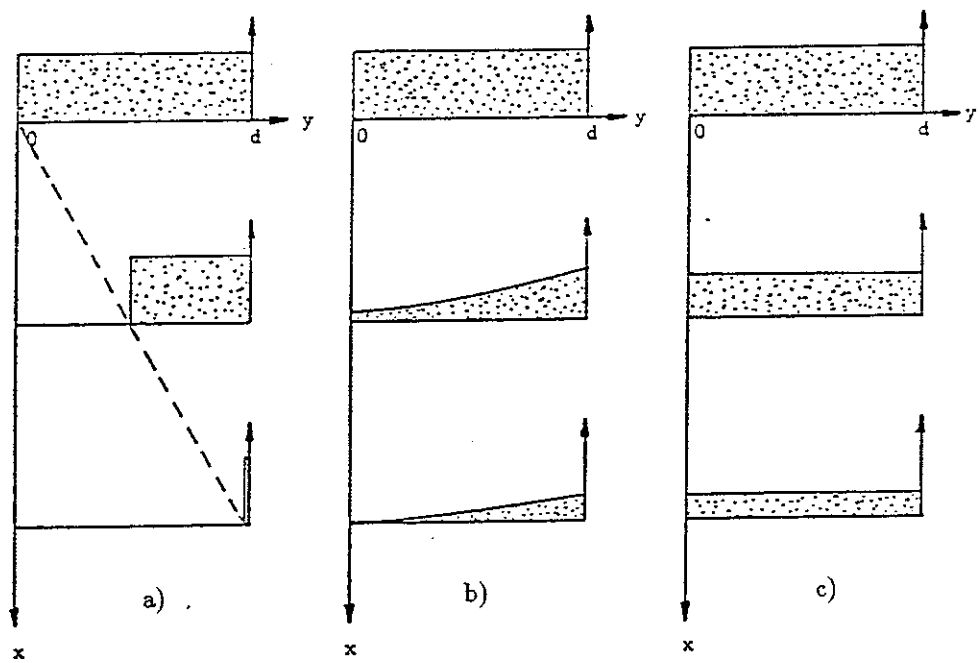

Fig. 8.1 Schematic illustration of the effect of various levels of turbulent diffusivity on the particle concentration profiles at three different streamwise axial positions. a) $D = 0$, b) $D \neq 0$, and c) $D = \infty$, from [8].

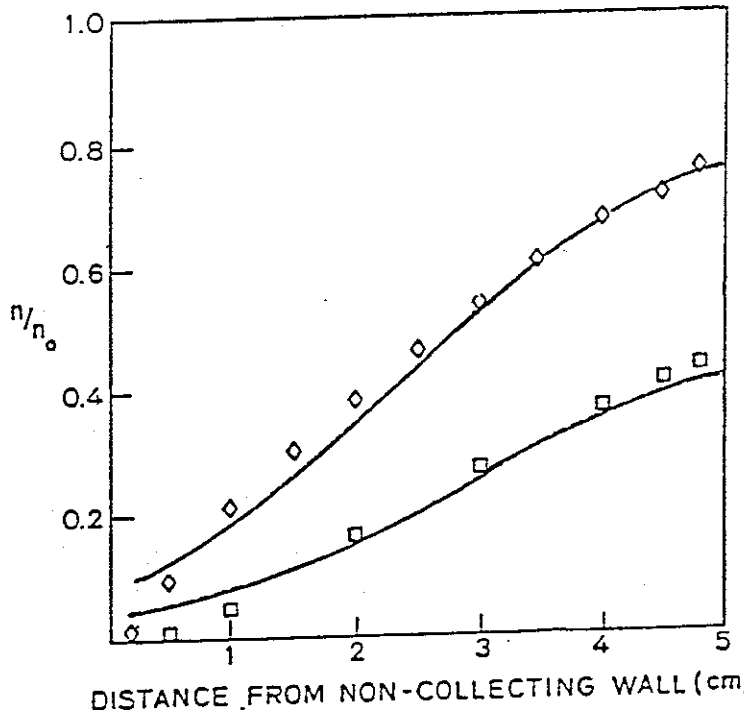

(A)

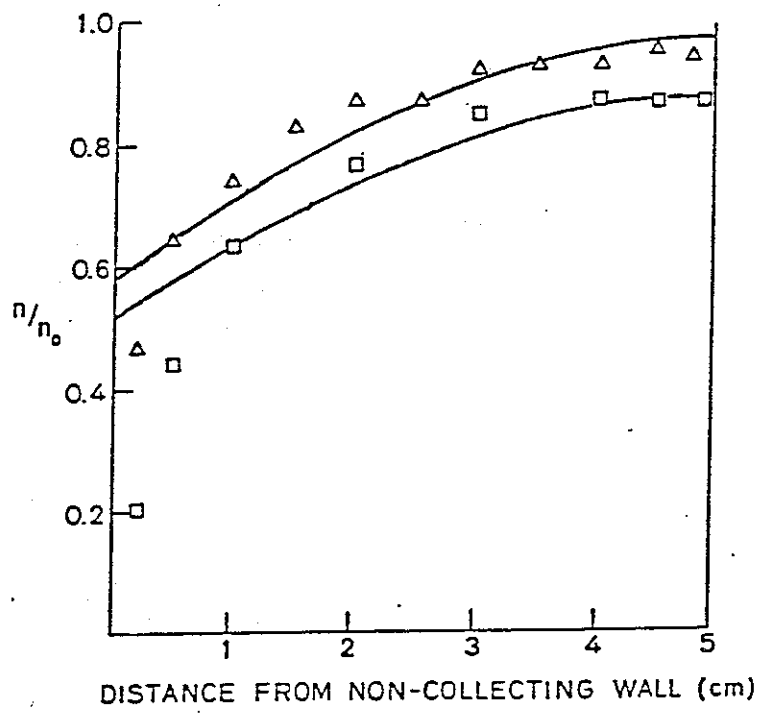

(B)

Fig. 8.2 Particle concentration profiles: 1 cm height baffles, $U_0 = 3$ m/s, $D = 30$ cm^2/s at two axial positions, x = 25 cm ◇, △ and x = 45 cm □ . A) $v_{ey} = 0.3$ m/s, B) $v_{ey} = 0.075$ m/s, from [6].

The diffusion coefficient in Eq.(8.1) determines the degree of turbulent mixing of particles inside the ESP and it has a direct connection to the turbulence level in the flow [8]. If the turbulent mixing approaches infinity, the particle concentration profile becomes uniform in transversal direction at any axial position, see fig. 8.1c. In this case the governing equation may be simplified to a one dimensional case where it is assumed that all changes occur in the axial direction, and the solution will be the same as the Deutsch equation (Eq.(4.3)). Thus, the Deutsch equation is an extreme case of turbulent mixing with a pessimistic prediction of the ESP efficiency. The opposite case of the Deutsch equation occurs when the turbulent mixing of particles becomes negligible, which causes an optimistic high efficiency due to the laminar transport of particles, fig. 8.1a. It is seen that none of these cases are realistic assumptions since the turbulence generation due to the flow arrangement and electric field production in the ESP are not negligible [50], and the truth lies somewhere in between, fig.8.1.b.

The experimental data obtained by Leonard et. al., [3] and [6] indicates, that the turbulent mixing may have a finite value and the measured concentration profile is a proof of this fact, fig.8.2.

Since the suspended particles of a few microns in diameter follow the fluid motions, the turbulent mixing of these particles may be the same as the surrounding gas. Therefore, the particle turbulent mixing coefficient, D will be assumed to have the same magnitude as the fluid turbulent diffusion coefficient, ν_T. See section 8.5.8.

8.2 Numerical discretization

The discretization of the governing equation is performed using a control volume formulation. In this formulation the scalar variables like the concentration and the property diffusion coefficient are placed at the center of the control volume, while the velocity vectors are prescribed at the control volume faces, see fig. 8.3a. Furthermore the central difference scheme and the upwinding hybrid scheme [56] are employed in discretization of diffusive and convective terms, respectively.

The grid is equidistant, the collector plate is smooth, and the electrode body is approximated by a square profile, see fig. 8.4.

8.3) Boundary conditions

The boundary conditions for the particle transport equation is implemented by Leonard et. al., [3] in the following approximations:

–inlet condition where the concentration is assumed having a constant profile of n_0 density,
–zero flux at the non–collecting surfaces,
–and zero slope at the collector plate.

The flux of particle concentration through the control volume surfaces is defined as

$$\phi = \mathbf{v}_p n - D\nabla n \,, \tag{8.2}$$

hence the zero flux condition at the non–collecting surfaces implies that

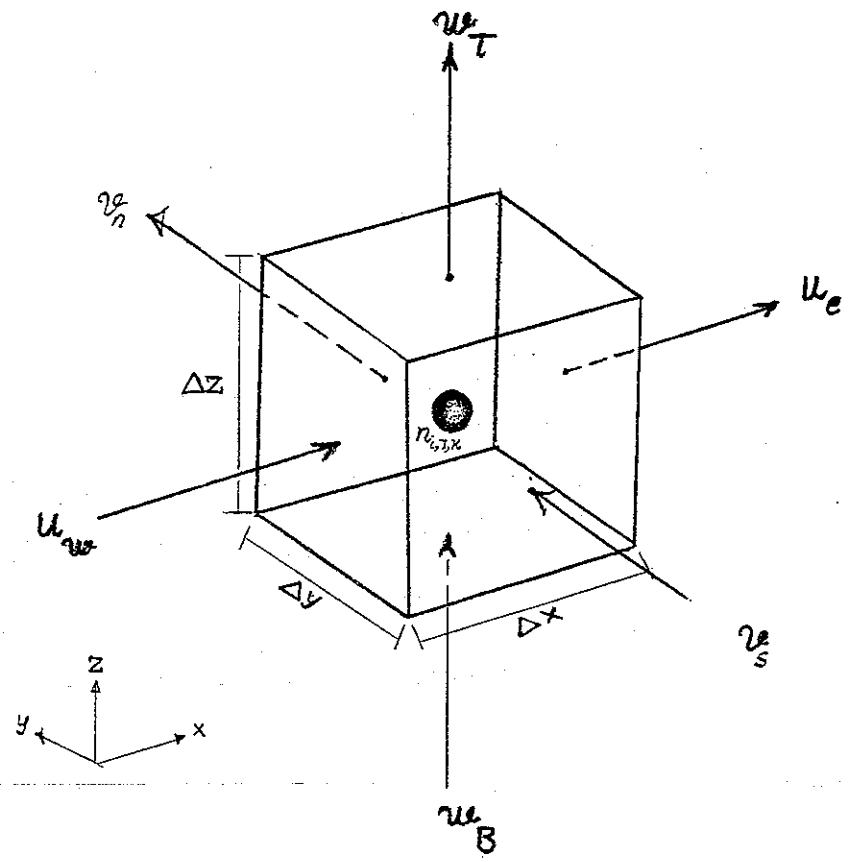

a)

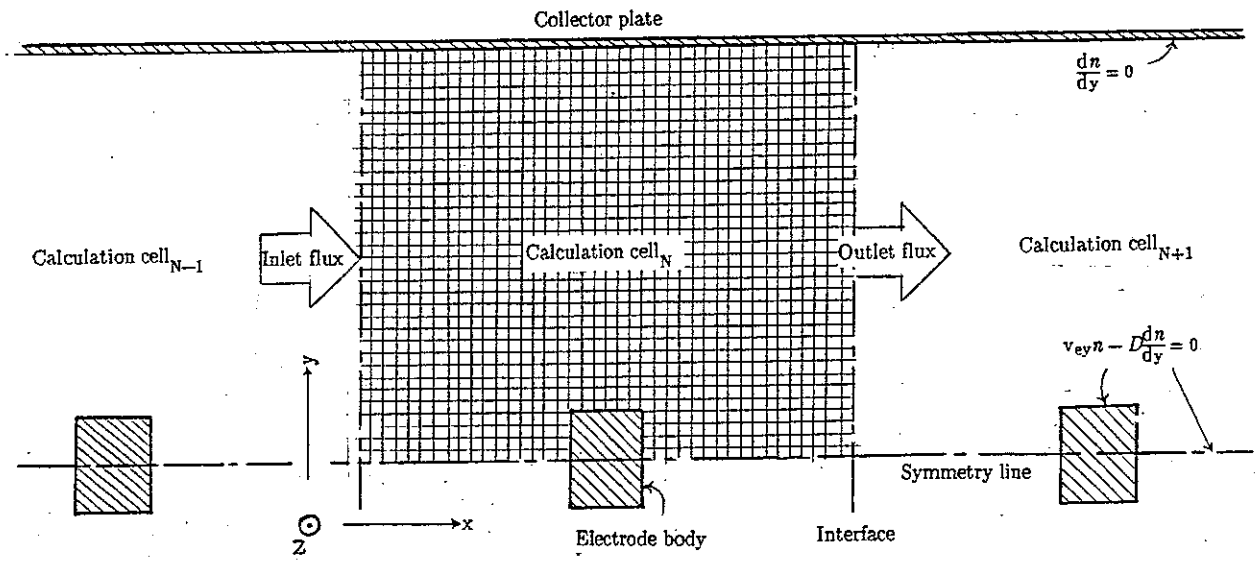

b)

Fig. 8.3 a) The position of the scalar quantities and the velocity vectors for three–dimensional control volume numerical formulation.
b) Cross–sectional view of grid arrangement, electrode collector geometry, and boundary conditions, and the interface between the neighboring symmetrical cells.

$$\phi = 0$$

or

$$\mathbf{V}_p n = D\nabla n \,.$$

The particle velocity at the collector plate equals the particle electric drift velocity perpendicular to the plate, v_{ey}. Hence the particle flux to the collector plate is

$$\phi_y = v_{ey} n \,.$$

Inserting this equation into Eq.(8.2) for the flux component perpendicular to collector plate, leads to

$$v_{ey} n = v_{ey} n - D \frac{dn}{dy}$$

or

$$\frac{dn}{dy} = 0 \,,$$

the zero slope condition at the collector plate.

These conditions are examined numerically by [3] and [8] and the results show good agreement with experiments.

As it was discussed in section 6.5.4, it will assume that the dust layer does not influence the electrical conditions (back corona does not occur) as long as the dust conductivity is greater than the gas conductivity or in other words the dust is low resistive. Furthermore, the influence of the dust layer on the flow management can be negligible for the layer thickness of a few millimeters.

8.4 Solution Algorithm

The Peclet number gives the limits for solving the transport equation either in elliptic or in parabolic way. This number for u, the axial component of the velocity field, in axial direction over the control volume length of Δx can be defined as

$$P_{ex} = \frac{u\Delta x}{D} \,.$$

The solution of the transport equation may be performed fully elliptic in transversal direction and parabolic due to high Peclet number in axial direction [56]. This will be a marching solution where the Peclet number must never become less than 2 in the axial direction. But, according to velocity calculations and measurements in chap. 7, there are recirculating flow fields up and downstream of the electrode body, which make the Peclet number less than 2 or negative. Therefore, the transport equation must be solved fully elliptic in these regions. This also implies that the calculations should be performed fully elliptic for the whole ESP section which demands large arrays and an unbounded program size. The alternative to this problem is to solve the particle transport equation for one periodic cell (see fig. 8.3b) fully elliptic to obtain the particle concentration field and mass flux through the cell. Then, the calculated mass flux at the outlet (interface) of this cell uses as inlet mass flux to the next calculation cell. This method may be justified by the fact that at the inlet and outlet of a calculation cell, the particle velocity profile is quite uniform and undisturbed by the wake downstream of the electrode. Thus the Peclet number is large and the transport of any scalar quantity in

these regions may be assumed to be parabolic. Hence, the concentration at the outlet of one calculation cell will not be influenced by the concentration changes in the next calculation cell. This solution will be called a block or a cell marching algorithm.

The SOR line by line method is selected as numerical method to solve Eq.(8.1). See also section 6.4.4 for more detailed description of this method.

8.4.1) Preliminary verification of the numerical program

A simple two dimensional version of the numerical program has been developed to test the experimental data presented by [8]. In this experiment precharged mono dispersed particles flow between two parallel plates. One with the potential φ_0 and the other one grounded. 2 cm baffles have been placed upstream before the inlet to produce favorable flow turbulence. The particle migration velocity is known from measurements and the diffusivity coefficient is estimated to be $D = 12 \times 10^{-3}$ m^2/s. It is assumed that the turbulence level is kept constant in the measuring section, and therefore D does not change in the axial direction.

Employing these boundary conditions and parameters in the numerical calculations, the result yields good agreement with experiments, see figure 8.4.

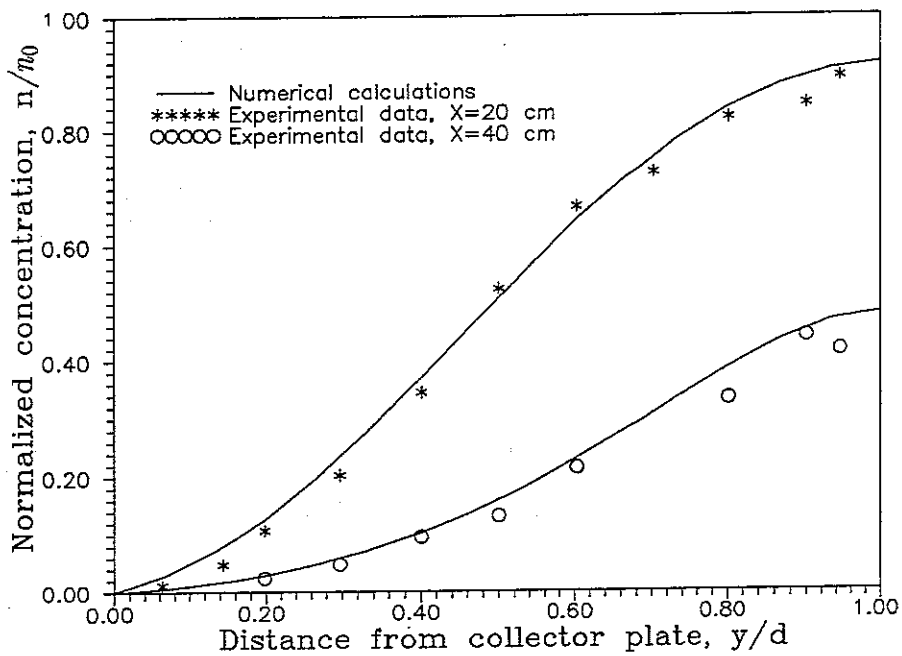

Fig. 8.4 Particle concentration profile for 2 cm double turbulence generating baffles: Uo = 2.0 m/s, $D = 12 \times 10^{-3}$ m^2/s, Wy = 0.2 m/s, experimental data from [8].

8.5 Particle behavior in ESP

Particle behavior inside ESP concerns the size distribution, charging mechanism, migration, precipitation at the collecting wall, dust layer formation, plate rapping, back corona phenomena, agglomeration, and re–entrainment. Some of these mechanism appear to have strong effects on the precipitation rate; therefore, to approach the physics of electrostatic precipitation, it is important to take their influence into account. It should be mentioned that since the present investigation concerns the ESP performance calculations at normal operating conditions, the contribution of back corona, agglomeration, and re–entrainment will not be included. It has not been possible to measure the minus flux due to the normal re–entrainment near the collecting plate for solid particles, therefore the contribution of this quantity will not be taken into account as well.

8.5.1) Size distribution

The migration velocity of particles depends on the particle size, therefore it is important to know the size of particles entering the ESP. The suspended particles in industrial emission gases have different shape and size. The shape of particles usually is quite irregular, therefore it is difficult to determine the particle size. In electrical precipitation, one is interested in the migration velocity of a particle in an electric field, and the Stokes diameter is most useful. However, there are also some other diameters like surface area diameter, volume diameter or mass diameter [31].

All together, particle size measurement gives us the possibility to have a quantitative view of the particle size and distribution.

Monodisperse aerosols seldom occur in nature or industry, therefore it is necessary to know the distribution from measurements or to formulate a mathematical description, as the input to the numerical calculations. Statistically, particle size distribution can be defined by two parameters, namely the geometric–mean particle size and the geometric standard deviation. This distribution is called log–normal distribution for size–frequency. The mathematical formulation of this distribution is given by

$$\gamma(d_p) = \frac{1}{\sqrt{2\pi}\,\sigma_g} \exp\left[-0.5\left(\frac{d_{pg}-d_p}{\sigma_g}\right)^2\right], \tag{8.3}$$

where $\gamma(d_p)$ is the frequency function, d_p is the particle diameter, d_{pg} is the geometric–mean particle size, and σ_g is the geometric standard deviation. A frequency distribution is shown in fig. 8.5. Any process which produces fine particles from an original bulk quantity gives a particle distribution which is close to a log–normal distribution.

Defining particle class d_p as particles in the size range $d_{p1} < d_p < d_{p2}$ one may define a normalized weighting coefficient, w_c, giving the percentage of particles within each particle class as

$$w_{c12} = \frac{\int_{d_{p1}}^{d_{p2}} \gamma(d_p)\ \mathrm{d}d_p}{c_d}, \tag{8.5}$$

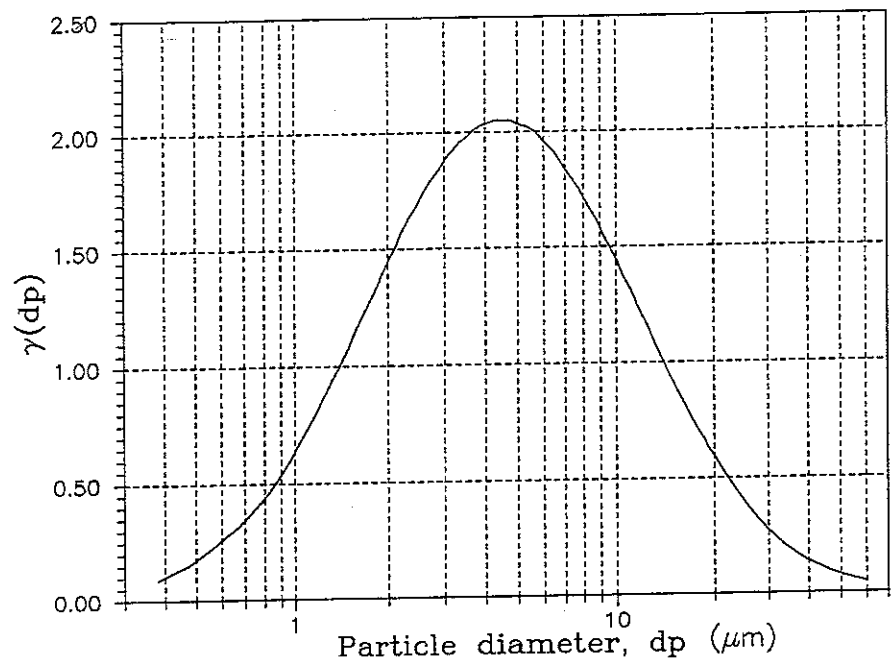

Fig. 8.5 Log–normal particle size distribution over 100 class of particles. $d_{pg} = 5.0$ μm, $\sigma_g = 2.5$ μm.

where the total concentration at the location is obtained from the cumulative distribution function,

$$c_d = \frac{1}{\sqrt{2\pi}\sigma_g} \int_0^{+\infty} \exp[-0.5(\frac{d_{pg}-d_p}{\sigma_g})^2]\, d d_p \,. \tag{8.4}$$

The weighting coefficient of each particle class varies along the ESP due to variation of the particle distribution. For instance, multiplying the weighting coefficient of a certain particle class at any axial position by the concentration, the result will be the particle concentration of that class at that axial position.

8.5.2) Charging mechanism

The main particle charging mechanisms in the corona electric field are the field and the diffusion charging [31]. The field charging is the most important mechanism for particles over 0.5 μm, while for particles below 0.2 μm the diffusion charging becomes the dominating mechanism. Particles in the range 0.2 – 0.5 μm are charged almost equally by the field and the diffusion charging mechanism.

In the field charging process, the gas ions under the effect of the electric field impact the surface of the particle and deliver their charges to it. Thus, an electric field at the surface of the particle will be established. The flux of free charges to the particle continues until the electric field at the surface of the particle becomes so strong that the external charging field will not be able to increase the ion density at the surface of the particle, implying that the particle has reached its saturation charge.

In the diffusion charging mechanism, the free ions due to their inter–molecular thermal motions impact the surface of the particle and increase the electron density.

White [31] has introduced the following equation for calculation of the saturation charge,

$$q_{sj} = \pi\epsilon_0\left[(1+\frac{2\lambda}{d_{pj}})^2 + \frac{1}{1+2\lambda/d_{pj}}\cdot\frac{\epsilon_r-1}{\epsilon_r+1}\right]\cdot d_{pj}^2\, E\,, \tag{8.6}$$

where q_{sj} is the saturation charge of j–th particle class with a diameter of d_{pj}, ϵ_0 is the vacuum permeability, λ is the ion free path, ϵ_r is the relative dielectric constant for the particle and E is the mean electric field in transversal direction. It should be mentioned that this equation contains both the contribution of the field charging and the diffusion charging mechanism.

8.5.3) Particle drift velocity and mobility

Charged particles of the size of a few microns under the effect of the electric Coulomb forces and the Stokes drag, reach the terminal drift velocity in a fraction of their resident time in the ESP. Employing the balance between the electrical Coulomb forces and the Stokes drag forces leads to

$$\mathbf{v_{ej}} = \frac{q_j \mathbf{E}}{3\pi\cdot\mu\cdot d_{pj}}\,, \tag{8.7}$$

where the $\mathbf{v_{ej}}$ is the electric drift velocity of j–th particle class, q_j is the particle charge, μ is the kinematic viscosity and $\mathbf{E}$ is the local electric field. As explained in chap. 7, the ratio $b_{pj} = q_j/(3\pi\cdot\mu\cdot d_{pj})$ is defined as the particle mobility. Particle charge, mobility , and drift velocity, depend on the charging electric field which will be discussed in the following section.

8.5.4) Interaction between particle space charge and charging field

Particle charge depends both on the electric field, the amount of free ions in space (space charge) and the resident time in the charging field. Employing the balance between the instantaneous ionic flux to the surface of a spherical particle and the resulting electric field, one may derive the following relationship for instantaneous particle charge, [47]

$$q_j = q_{sj}\cdot\frac{b_i\rho_i t}{b_i\rho_i t + 4\epsilon_0}\,. \tag{8.8}$$

In this equation, ρ_i is the ionic space charge and t is the residence time. And notice that the charging electric field is implicit included in q_{sj}.

Furthermore, Eq.(8.8) may be used in derivation of the equation for particle space charge, ρ_{pj} by dividing with the particle mass and multiplying by the mass concentration,

$$\rho_{pj} = q_{sj}\cdot\frac{b_i\rho_i t}{b_i\rho_i t + 4\epsilon_0}\cdot\frac{n_j}{m_{pj}}\,, \tag{8.9}$$

where n_j and m_{pj} are the concentration and the mass of j–th particle class. Figure 8.6 shows the variation of ρ_{pj} as a function of residence time for different levels of ρ_i for a given particle size d_{pj}.

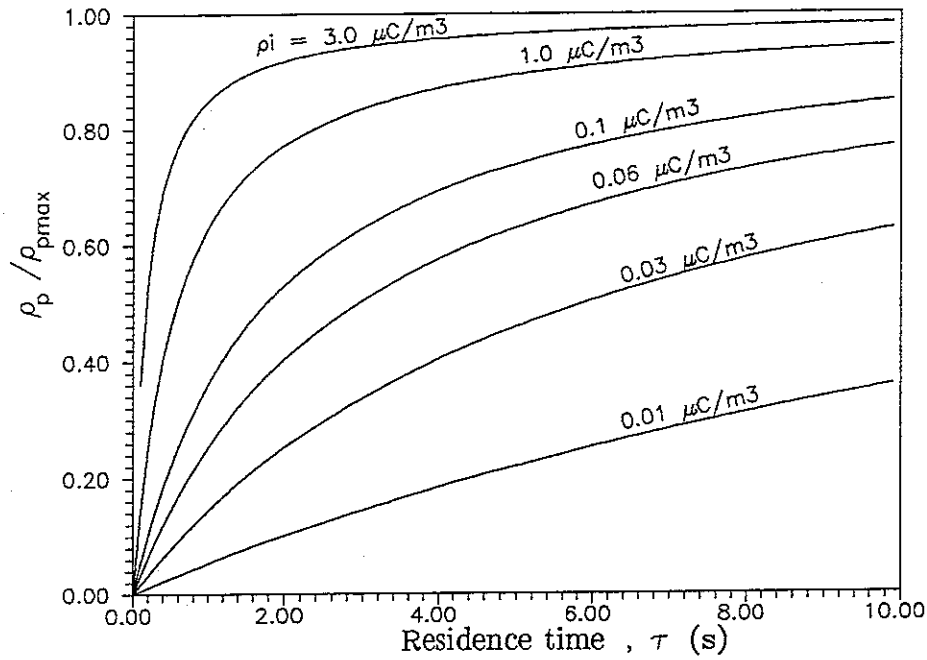

Fig. 8.6 The variation of particle space charge versus the residence time in ESP for different levels of ionic space charge for $d_p = 5$ μm.

The mean particle space charge, ρ_p at any point in ESP over different particle classes of a certain distribution can be defined as

$$\rho_p = \sum_{j=1}^{N_{pc}} q_j \cdot \frac{n_j}{m_{pj}}, \tag{8.10}$$

where N_{pc} is the number of particle classes and the index "$_j$" is the class number. Notice that n_j may also be defined as $n_j = w_{cj} \cdot n_m$, where n_m is the mean concentration over all particle classes and w_{cj} is the weighting coefficient belonging to each class.

The (mean) particle mobility, b_p may also be defined as

$$b_p = \sum_{j=1}^{N_{pc}} \frac{q_j}{3\pi\ \mu\ d_{pj}} w_{cj} \cdot \tag{8.11}$$

Particles in a strong charging field, which represents a significant amount of ionic space charge, reach their saturation charge already at the inlet of the ESP [31]. Therefore, the standard ESP efficiency models assume that particles are fully charged when entering the ESP. This means the particle mobility has reached its maximum value already at the inlet, hence the particle will move toward the collector plate with its maximum attainable drift velocity. Obviously, such models end up with an optimistic value for the efficiency if this assumption differs from the real charging mechanism inside the ESP. If for some reasons the ionic space charge becomes insufficient within the electric field, the particles will not reach their saturation charge even if the charging time becomes sufficiently large. Actually, this is a fact that should be examined carefully, which is now done.

Recalling the numerical results from chap.6 for the relationship between the current density and the particle space charge in fig. 6.32, it can be seen that the current density decreases for increasing particle space charge, and it then becomes negligible for $\rho_p = 30\ \mu C/m^3$. This means that even when there is a high potential difference between the electrodes and the collector plates, there is no corona emission in this region, implying that the corona current is quenched. Closer investigation of this phenomenon shows that the electric field near the emission electrode has become so weak, that it is not able to accelerate the electrons from the surface of the electrode to the drift region. Calculation of particle space charge for fully charged particles with $d_{pg} = 5\ \mu m$ and $\sigma_g = 2.5\ \mu m$ in a charging field of 330 kV/m and an inlet concentration of 5 g/m^3 results in a particle space charge of 80 C/m^3. Actually, this is a normal loading for ESPs and in some cases with heavy loading, the amount of inlet concentration may rise up to 120 g/m^3, which in turn will increase the amount of particle space charge 24 times. Obviously, this amount of particle space charge at the inlet of ESP is unrealistic due to the fact, that particles are neutral at the inlet and first begin to charge by entering the charging region. Hence, there will be an interaction between the corona emission and the induced particle space charge, and this interaction will continue until a balance between these two mechanisms is reached.

It is possible to model this interaction numerically in terms of the resulting equilibrium between the ionic corona space charge and particle space charge for one cell by solving the following equations in this order

1—assume $\rho_p = 0$
2—solve the equation for electric the field, Eq.(6.2)
3—solve for conservation of charge (current), Eq.(6.3)
4—solve Eq.(8.10) and Eq.(8.11) for ρ_p and b_p (b_p uses in Eq.(6.3))
5—start from step 2 until equilibrium value of ρ_p and ρ_i have been found.

Once the equilibrium between the ρ_p and ρ_i is established, the solution of the particle transport equation will lead to a new concentration field for calculating the balance between ρ_p and ρ_i in the next calculation cell.

When a particle moves through a charging field of various ion density and electric field strength, it may be assumed that the resulting charge on the surface of the particle may equal the charge on the same particle in an averaged charging field of the same ion density and electric field. This assumption makes it possible to have charged particles in the regions where there are no charging ions, and therefore the only parameter which can change the amount of particle space charge may be the concentration field.

When calculating particle space charge, the averaged electric field and the averaged ionic space charge are employed to calculate the weighted sum of charge/mass ratio of all particle classes. Then the multiplication of this parameter by the concentration field leads to the particle space charge field in the calculating cell.

8.5.5) Charging rate

In this part we will define the ratio,

$$C_r = \frac{b_i \rho_i t}{b_i \rho_i t + 4\epsilon_0}, \tag{8.12}$$

from Eq.(8.8) as the charging rate of particles. This ratio increases along the ESP as the concentration of particles and in turn particle space charge decreases and it becomes

equal to unity when the concentration becomes negligible. The charging rate is the ratio of the actual charge to the saturation charge. For a low inlet concentration and a strong charging field with high level of ionic space charge density the charging rate already approaches unity at the inlet of the ESP.

The charging rate has influence on the particle mobility and drift velocity. For instance, if particles have reached 50% of their saturation charge, then according to Eq.(8.7) the particle mobility and the drift velocity will be 50% of their maximum value. The multiplication of the charging rate by the particle mobility gives the instantaneous values of particle mobility in the actual calculating cell.

8.5.6) Dust formation on collector plate

Particles under the effect of coulomb forces move toward the collector plate and accumulate on the plate in form of a dust layer. The electric force, $F = \rho_i E/b_i$ keeps the dust layer at the collector plate and the layer thickness increases until the collected dust is removed by rapping. The dust layer density varies due to variation of the ion density and electric field at the collector plate. When the dust layer has reached a certain thickness the collector plates must be rapped.

The rapping time depends on the dust layer thickness at the collector plate and the dust layer thickness varies along the ESP due to variation of particle concentration in the axial direction. Therefore, the rapping time may be calculated for each cell in advance. It should be mentioned that the maximum dust layer thickness, δ_{max} is an experimentally determined value which is typpically about 5 mm for normal operating ESPs [53]. The dust mass flux deposited at the collector plate in one cell, $\Delta \dot{m}_{dust}$ may be calculated as the difference between the netto mass flux at the inlet and the netto mass flux at the outlet of the calculating cell,

$$\Delta \dot{m}_{dust} = \int_A \mathbf{v}_p n \cdot \mathbf{n} dA \,, \tag{8.13}$$

where **n** is the outward normal to the cell's inlet and outlet flux area, A.

If the resident time for particles in one cell is $\Delta t = l_x/U_0$, the collector area is $l_x \times l_z$, and the dust layer density is ρ_d, then the dust layer thickness for one sweep through the cell becomes

$$\delta = \frac{\Delta \dot{m}_{dust}}{U_0 \; l_z \; \rho_d} \,. \tag{8.14}$$

And the rapping time my be expressed as

$$\tau_{rapp} = \frac{\delta_{max}}{\delta} \Delta t \,. \tag{8.15}$$

The net mass flux to the collector plates from the inlet at any axial position in the ESP may also be calculated by subtracting the inlet mass flux, $\dot{m}_i$ from the outlet mass flux of the last calculation cell, $\dot{m}_u$ as follows

$$\dot{m}_i - \dot{m}_u = U_0 n_0 l_y l_z - \sum_{j,k}^{N,M} u_{xjk} n_{xjk} \Delta y \Delta z \,, \tag{8.16}$$

where n_0 is the inlet concentration, n_{xjk} and u_{xjk} are the concentration and velocity fields at the axial position x form the inlet, and summation refers to the numerical integration. Then the efficiency of the ESP may finally be calculated as

$$\eta = (\dot{m}_i - \dot{m}_u)/\dot{m}_i \,. \tag{8.17}$$

8.5.7) Estimation of the turbulent diffusion coefficient

The flow inside the ESP is affected by the geometry, turbulent diffusion and the electrical body forces on the ionized gas. Therefore, the variation of these parameters change the flow quality which in turn will influence on the transport of the particles. Assuming that particles in submicron size follows the flow patterns, then the particle turbulent diffusion coefficient, D, may have the same magnitude as the momentum diffusion coefficient, ν_T. Therefore, we will be content to estimate the influence of the bulk flow, the electrode–collector distance, and electric body forces on the turbulent diffusion coefficient, ν_T.

Assuming that the electric force production of the turbulent kinetic energy, κ, in the flow is in balance with the dissipation rate, ϵ, and diffusion of turbulent kinetic energy can be ignored, then the continuity of the turbulent kinetic energy may be expressed as

$$\nabla \cdot (v_f \kappa) = 0 \,. \tag{8.15}$$

If all variations occur in axial direction, then we may write

$$U_0 \, \kappa \, A = \text{Constant}, \tag{8.16}$$

where U_0 is the axial bulk flow and $A = l_y \times l_z$, the area perpendicular to U_0.

According to the (κ,l)–turbulence model [33], the turbulence diffusion coefficient, ν_T may be approximated as

$$\nu_T = l\sqrt{\kappa} \,, \tag{8.17}$$

or

$$\kappa = (\nu_T / l)^2 \,, \tag{8.18}$$

where l is the mixing length scale. Introducing Eq.(8.17) into Eq.(8.16), then the balance between two different systems with turbulence kinetic energies of κ_1 and κ_2 becomes

$$U_{01} \, \kappa_1 \, A_1 = U_{02} \, \kappa_2 \, A_2 \,,$$

or

$$U_0 \, (\nu_{T_1} / l_1)^2 \, l_{y1} \, l_{z1} = U_{02} (\nu_{T_2} / l_2)^2 \, l_{y2} \, l_{z2} \,. \tag{8.19}$$

Assuming that l_1 and l_2 are of the same order of magnitude and $l_{z1} = l_{z2}$, then we may write

$$\nu_{T_2} = \nu_{T_1}\left((U_{01}\, l_{y1})/(U_{02}\, l_{y2}) \right)^2 , \tag{8.20}$$

or

$$\kappa_2 = \kappa_1\, (U_{01}\, l_{y1})/(U_{02}\, l_{y2}) . \tag{8.21}$$

Equation (8.19) implies that if we know the magnitude of $\nu_T = \nu_{T_1}$ for one system, then by changing the flow velocity, U_0, or electrode–collector distance, l_y, we may be able to estimate the new value of $\nu_T = \nu_{T_2}$.

Even if Eq.(8.20) is a rough simplification of the turbulence balance, it contains the physics of the turbulence generation inside the ESP. This fact may also be supported by recalling the experimental data from fig. 7.17, which shows the turbulent velocity fluctuations are inversely proportional to the flow velocity. For instance, if we assume $\nu_{T_1} = 10^{-3}$ m^2/s for U_{01}= 1.0 m/s, then for U_{02} = 2.0 m/s ($l_{y1} = l_{y2}$), the diffusion coefficient decreases to $\nu_{T_2} = 0.25 \times 10^{-3}$ m^2/s. This relation will be used to estimate the magnitude of ν_T and D in the efficiency calculations for variable flow velocity and electrode–collector distance.

8.6) Program test and numerical results

This section will investigate the influence of dust loading, bulk flow, particles, electrode–collector distance, and turbulence diffusion mixing on the precipitation process. Furthermore the economical consequences due to variation of the flow velocity and the electrode–collector distance will be outlined.

Following parameters are used in calculation of the ESP's efficiency:

–Electrodes: Fibulax electrodes approximated by a square profile of 20 × 40 mm
–Collector plates: smooth
–Section length: 4.5 m
–Number of sections: 2
–Electrode–collector plate distance, l_y: 300 and 400 mm
–Distance between the electrodes, l_x: 300 mm
–Grid: equidistant, $\Delta x = \Delta y = \Delta z = 5$ mm
–Mean electric field between the electrodes and the collector plates, E: 3.3 kV/cm
–mean current density for clean ESP, J_m: 300 μA/m^2
–Corona onset at emission electrode, ρ_0: 240 μC/m^3
–Emission gas: air
–Gas density: 1.2 kg/m^3
–Gas temperature: 20 C^o
–Gas mobility, b_i: 2×10^{-4} m^2/Vs
–Ion path, λ: 137×10^{-9} m
–Bulk velocity, U_0: 0.5, 1.0, 1.5, 2.0 m/s
–Gas dynamic viscosity, μ: 18.5×10^{-6} kg·s/m
–Gas molecular momentum diffusivity, ν: 15.7×10^{-6} m^2/s
–Gas and particle turbulent diffusion coefficient ratio (l_y = 300 mm), $\nu_T/\nu = D/\nu$: 200.0,

50.0, 22.3, 12.5 for 0.5, 1.0, 1.5, and 2.0 m/s bulk velocities, respectively
—Gas and particle turbulent diffusion coefficient ratio (l_y = 400 mm), $\nu_T/\nu = D/\nu$: 150.0, 37.5, 16.6, 9.3 for 0.5, 1.0, 1.5, and 2.0 m/s bulk velocities, respectively
—Particle geometric mean diameter, d_{pg}: 5.0 μm
—Particle geometric standard deviation, σ_g: 2.5 μm
—Number of particle classes: 10
—Particle diameter of each class, d_p: 0.23, 0.68, 1.65, 3.09, 5.27, 8.54, 13.5, 20.98, 32.29, 49.38 μm.
—Relative dielectric constant for particles, ϵ_r: 10
—Dust mass density, ρ_d: 1000 kg/m^3
—Inlet concentration, n_0: 2 and 5 g/m^3
—Maximum permitted dust layer thickness, δ_{max}: 5 mm.
—Dust resistivity: less than 10^9 Ωm

The flow chart over the numerical program, "ESP" may be studied in table 8.1.

8.6.1) Dust loading effects

The concentration of charged particles between the emission electrodes and the collector plates lowers the performance of the charging mechanism which in turn changes the charging rate and decreases the current density at the collector plate. These variations are illustrated in fig. 8.7 and fig. 8.8. As it can be seen from these figures, the charging rate and the mean current density at the collector plate decreases with increasing the inlet dust loading. Particle space charge, ρ_p, decreases when particles get precipitated along the ESP causing the current density increases to its maximum value. A similar variation of current density was also observed by the measurements on large scale ESPs [53]. The particle concentration and space charge variation history are illustrated in fig. 8.9 and 8.10, respectively, for two levels of dust loading.

According to Eq.(8.7), Eq.(8.8) and Eq.(8.10), the variation of particle mobility and drift velocity is proportional to charging rate, C_r. Therefore, these two parameters vary similar to C_r in the axial direction. But, we should notice that the variation of mean particle mobility and drift velocity due to changes in the particle distribution and hence the weighting function along the ESP may not be the same as the mobility and the drift velocity changes of the individual particle classes. The variation of particle distribution and the mean particle mobility in axial direction are shown in fig. 8.11 and 8.12 respectively.

Precipitation of particles along the ESP increases the dust layer thickness at the collector plate. The dust layer variations in axial direction depends on the particle concentration and the precipitation rate within each calculation cell. The dust layer variation along the ESP is illustrated in fig. 8.13. Also, these results are obtained assuming no dust layer on plates. The rapping time, τ_{rapp}, for the first section becomes equal 106 minuets for 5 g/m^3 inlet dust loading.

The normalized particle concentration profile in transversal direction at different axial positions is shown in fig. 8.14. In this figure the uniform concentration at the inlet of the ESP becomes nonuniform in axial direction. But, the concentration profile may become uniform at any axial position if the turbulent diffusion coefficient, D approaches infinity which implies the Deutsch equation for the mass conservation in the ESP.

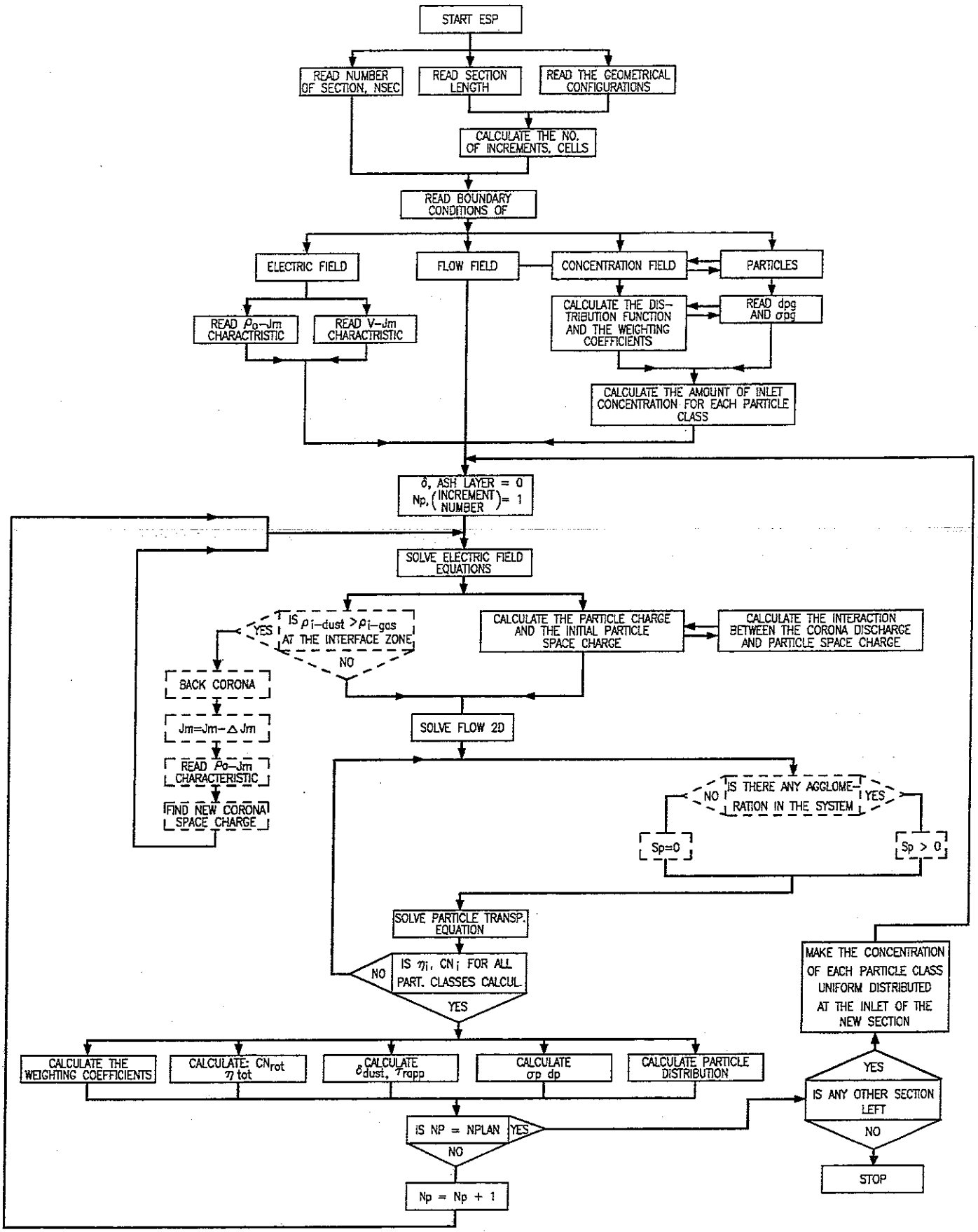

Table 8.1 Flow chart over the numerical operations in the ESP computer model.

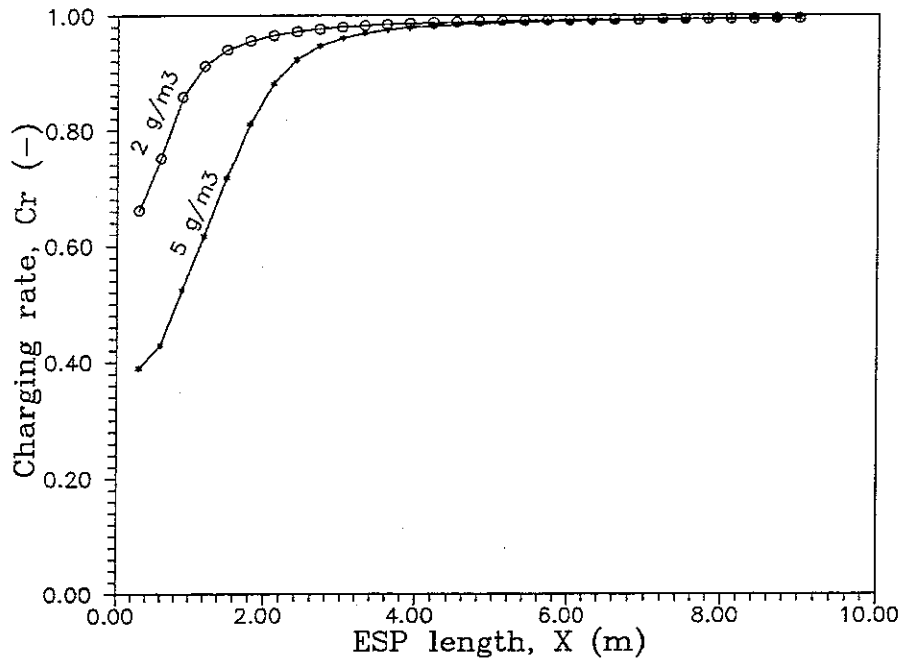

Fig. 8.7 Variation of charging rate along the ESP.

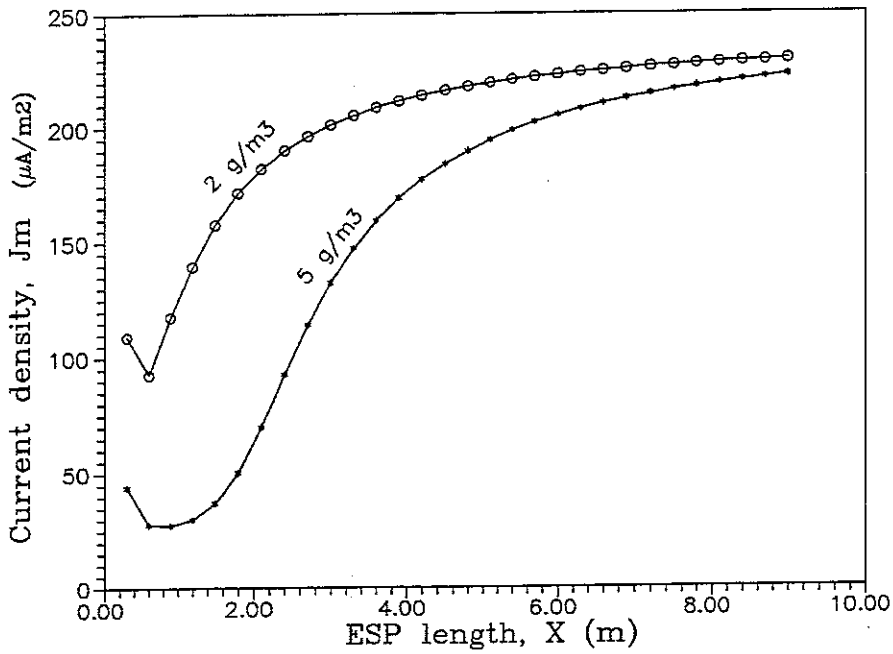

Fig. 8.8 Variation of averaged current density along the ESP.

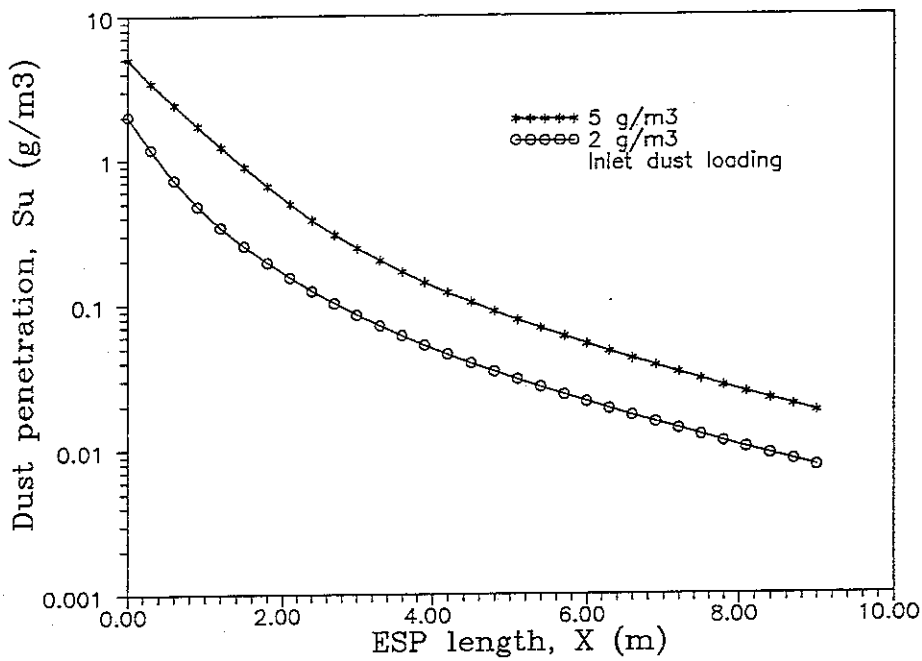

Fig. 8.9 Dust emission in axial direction for to different inlet loading of 5 and 2 g/m^3.

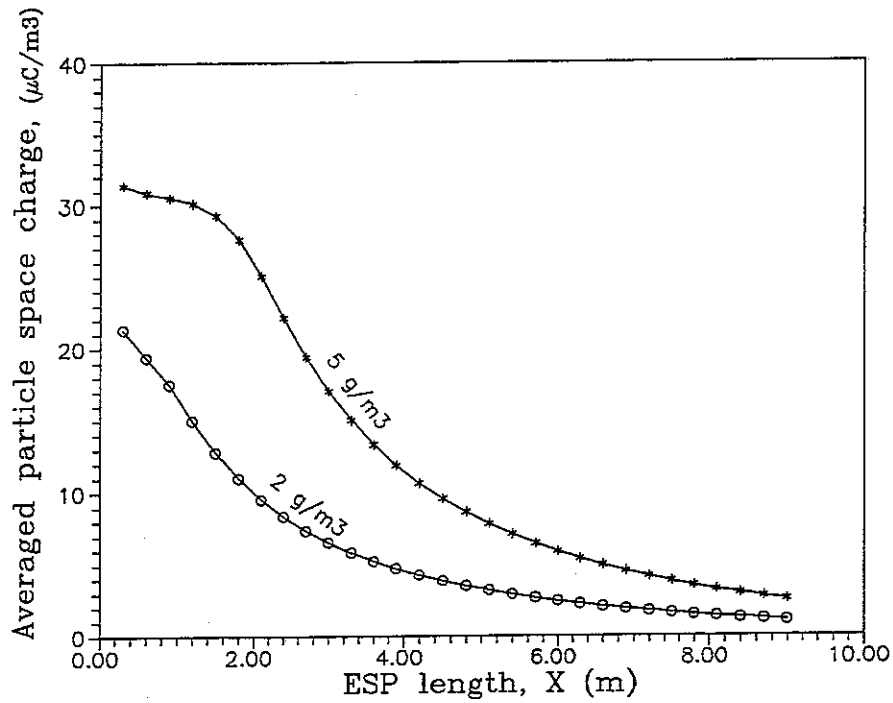

Fig. 8.10 The variation of particle space charge in axial direction for to different inlet loading of 5 and 2 g/m^3.

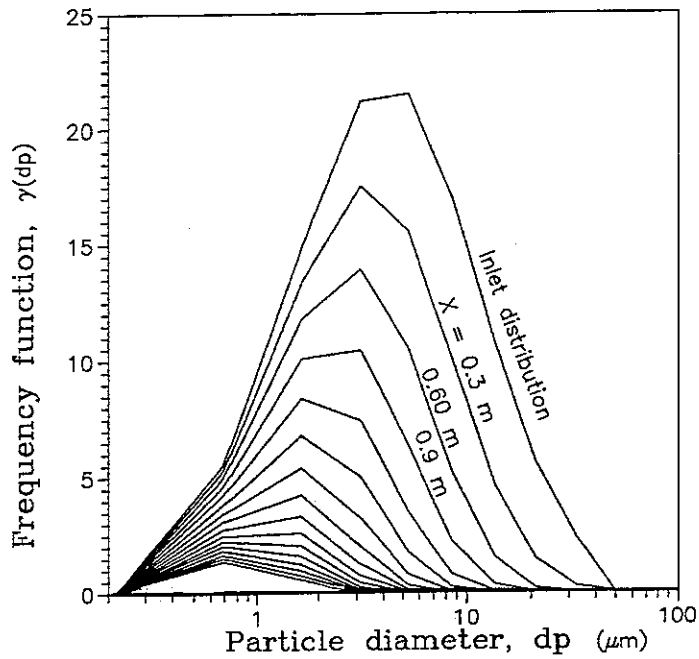

Fig. 8.11 Particle distribution in ESP at different axial positions over 10 class of particles.

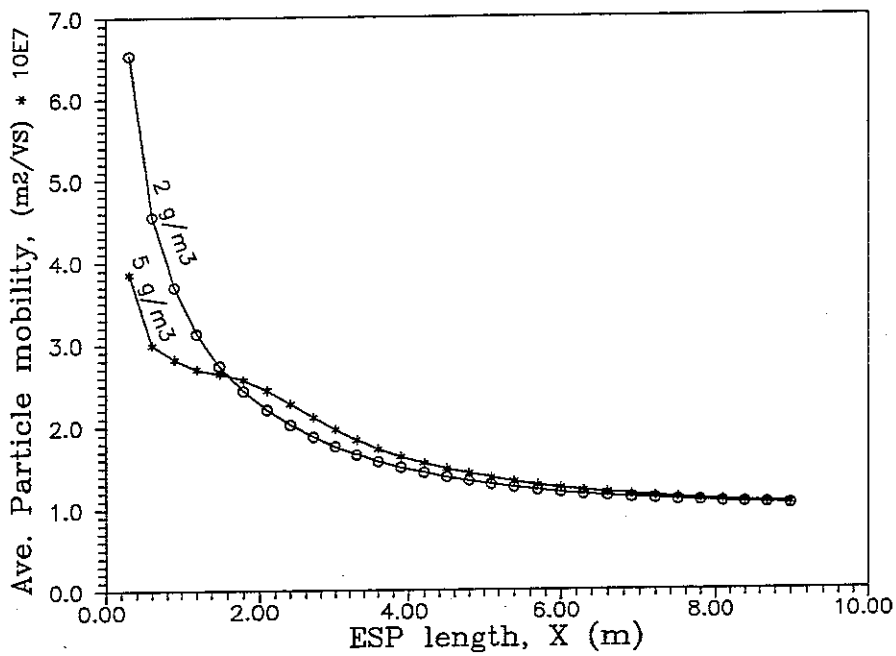

Fig. 8.12 Variations of the averaged particle mobility in axial direction.

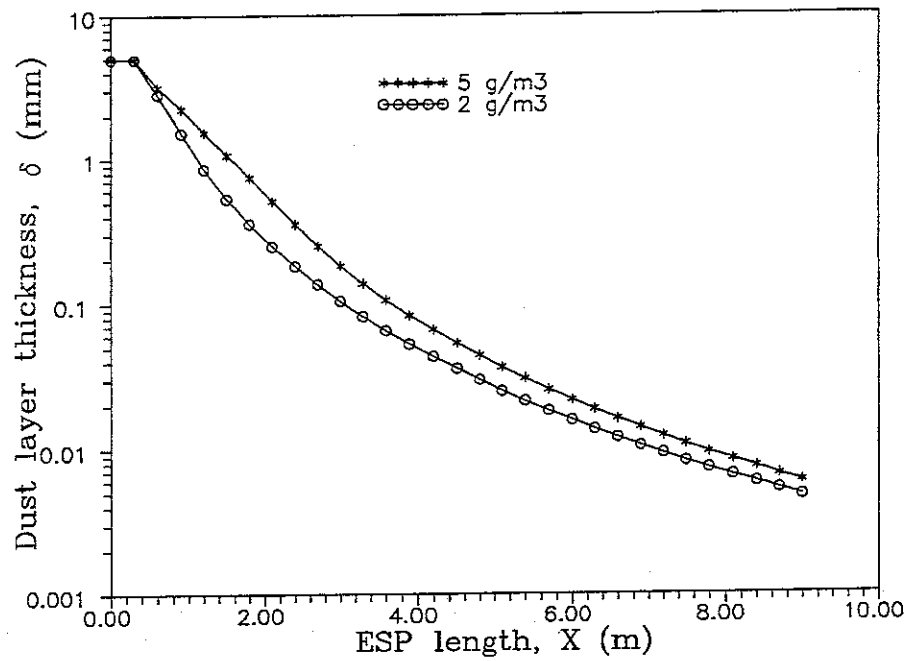

Fig. 8.13 The variations of dust layer thickness at the collector plate in axial direction at 106 minuets after rapping.

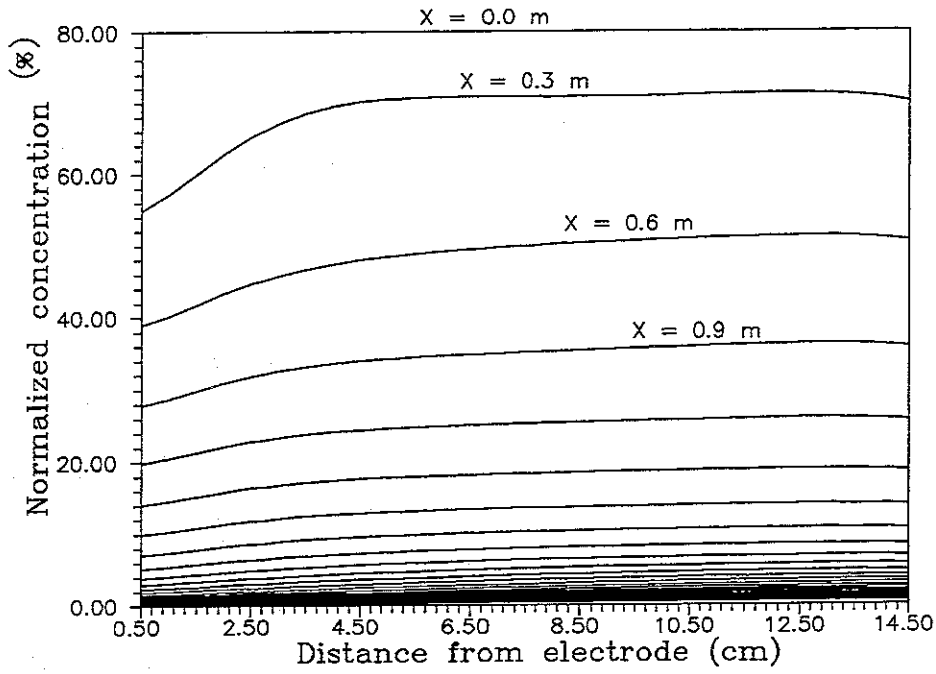

Fig. 8.14 Mean particle concentration profile at different axial positions. Channel wide is 15 cm and distance between the electrodes is 30 cm.

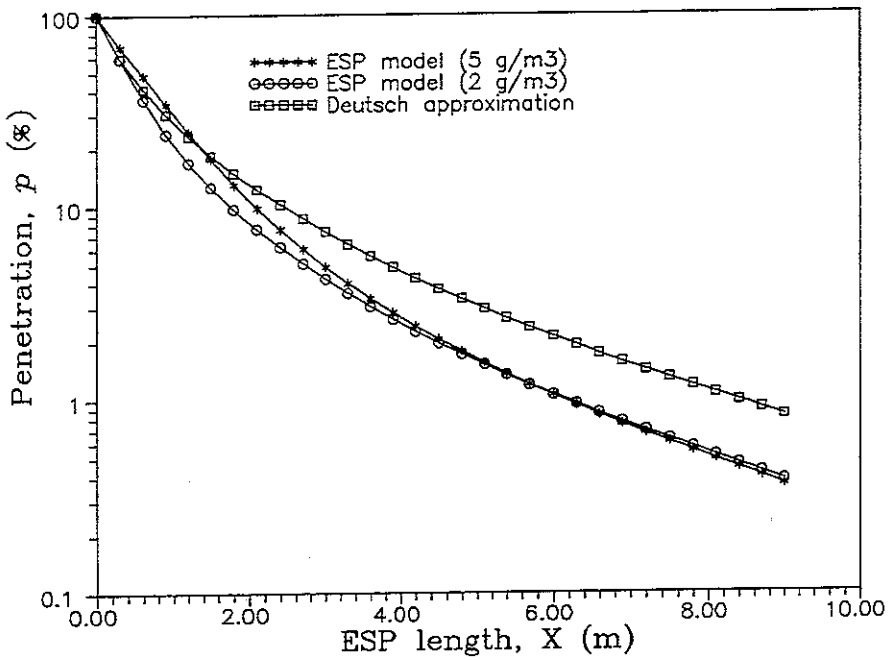

Fig. 8.15 Penetration changes throughout the ESP.

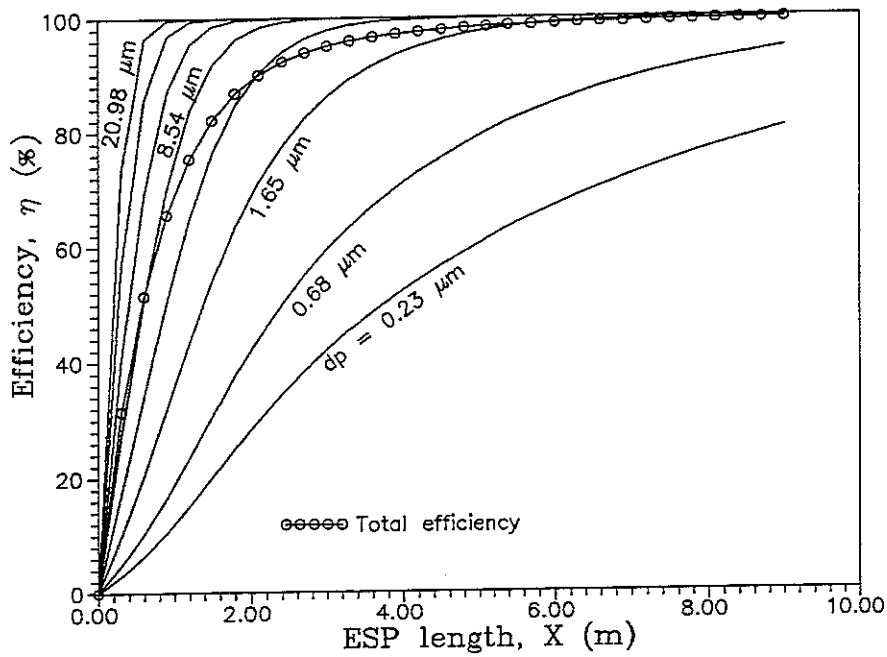

Fig. 8.16 Efficiency variations of different particle classes in axial direction.

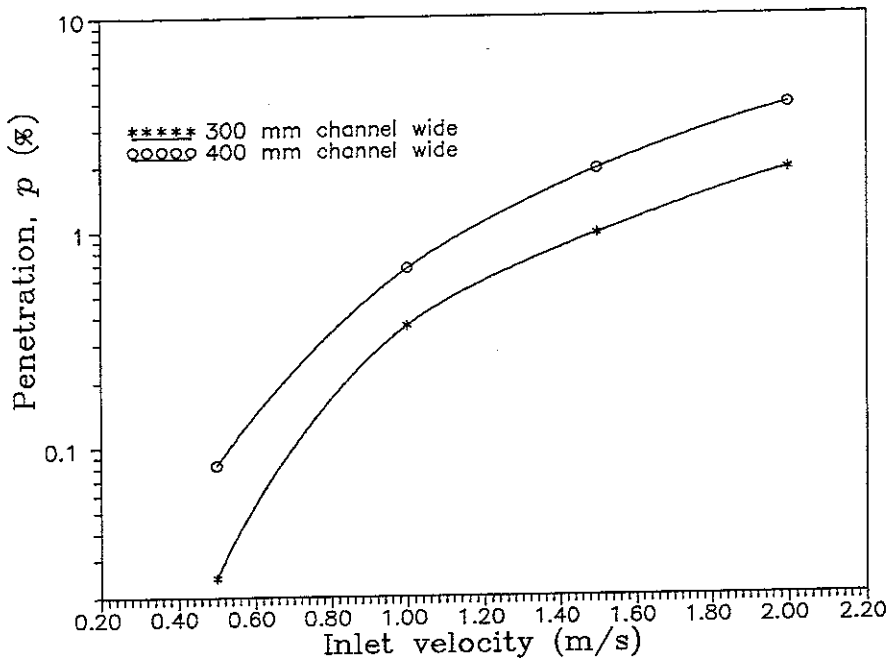

Fig. 8.17 Illustration of the penetration variations versus the inlet bulk velocity.

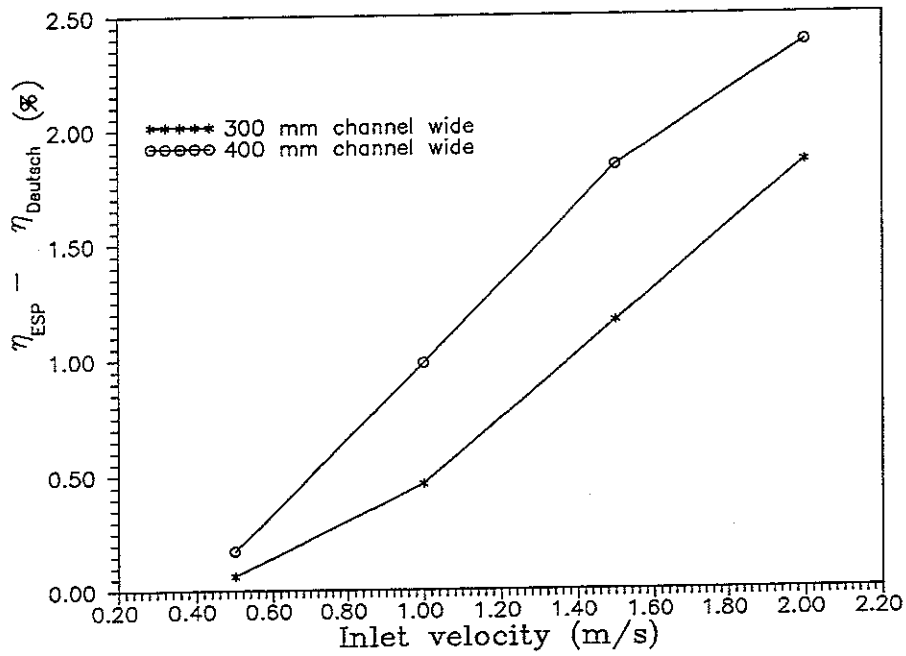

Fig. 8.18 The increase of the discrepancy between the Deutsch equation and the "ESP" calculations.

Figure 8.15 illustrates how the penetration changes in axial direction for both the Deutsch approximation with an infinite diffusion coefficient and the ESP model calculations with finite values for $D = \nu_T$ at all the axial positions.

The total efficiency of the ESP depends on the precipitation rate for each particle class. Particles of different size and drift velocity precipitate in different axial positions. Figure 8.16. shows the efficiency for 8 different classes in the distribution shown in fig. 8.11, as well as the total efficiency.

8.6.3) Effect of flow rate and electrode–collector distance on ESP efficiency

The ESP efficiency is strongly affected by the bulk velocity and the distance between the emission electrodes and collector plates. The effect of these parameters may also be fund in the Deutsch equation, Eq.(4.3) where U_0 and l_y are two of the main parameters influencing on the efficiency. According to the Deutsch's approximation the increase of the bulk velocity and the electrode–collector distance decreases the ESP efficiency. Therefore, we may expect the same tendency reflected in the numerical model as in the Deutsch approach.

Figure 8.17 shows the efficiency calculation results in the form of penetration, p for different imposed bulk velocities, U_0, and electrode–collector distances, l_y. It should be mentioned that all the inlet conditions to the "ESP" calculations are taken from an F.L.Smidth commercial ESP unit [53].

Comparing the results from the numerical calculation of the ESP efficiency with those of the Deutsch's predictions shows that by increasing the bulk velocity and the electrode–collector distance, the difference between these models increases, see fig. 8.18. The Deutsch model predicts lower values of efficiencies, hence is conservative.

8.7 Economical evaluation

The ESP price mainly depends on the geometrical design and the utilized mechanical and electrical facilities. For instance, an ESP with two sections contains an inlet and outlet flow diffuser, two frames holding the collector plates, two frames holding the emission electrode systems, two high voltage units, two dust hoppers, four rapping systems, and so on, see fig. 8.19. All these units are necessary in the design of an ESP, but there are some other parameters which may also change the ESP price drastically without affecting any of these units. The first parameter is the bulk velocity and the second parameter is the electrode–collector distance.

If we may be able to increase the bulk velocity, then according to flow continuity it will be possible to reduce the inlet area which means smaller ESP volume. Increasing the electrode–collector plate distance leads to reduction in the number of collector plates and electrodes for a given volume flow which in turn reduces the frames dimension and the total weight.

The Cost evaluation of an F.L.Smidth ESP unit (type: F) as a function of the inlet flow velocity and the electrode–collector distance is shown in fig. 8.20. This evaluation is performed under the circumstance that the ESP dust emission remains under the required level, $n|_{\text{outlet}} \cong 30$ mg/m^3. This emission level is guaranteed for $(U_0, l_y) = (1.0$ m/s, 300 mm) with a basic manufacturing price equal to unity.

As it can be concluded from fig. 8.20, an increase of both flow velocity and electrode–collector distance show the major influence on the reduction of the ESP price. But, it is interesting to see if the required dust emission limit can be fulfilled at off design conditions due to U_0 and l_y variations. Therefore, the "ESP" program has been tested for variable U_0 in the range 0.5–2.0 m/s with two different electrode–collector distances of l_y = 300 and 400 mm. The results are plotted in fig. 8.21. As it can be seen from this figure, the increase of the flow velocity and the electrode–collector distance raise the dust emission. But, according to these calculations it is possible to reduces the ESP basic price by either using a (U_0,l_y) = (1.22 m/s, 300 mm) or (U_0,l_y) = (0.97 m/s, 400 mm) combinations.

The first combination ends up with a price reduction of 9%, while in the second case the price reduces only about 3.2%.

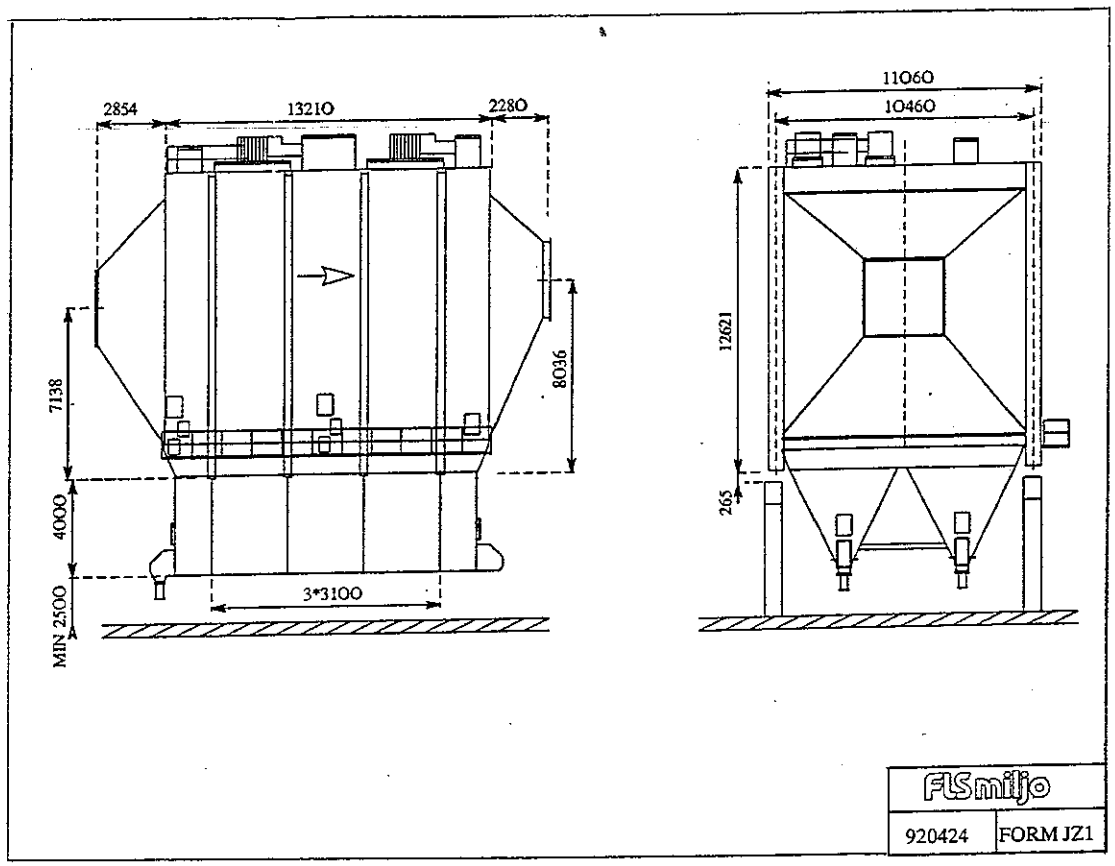

Fig. 8.19 Schematic front and side views of a F–type F.L.Smidth ESP design with two sections.

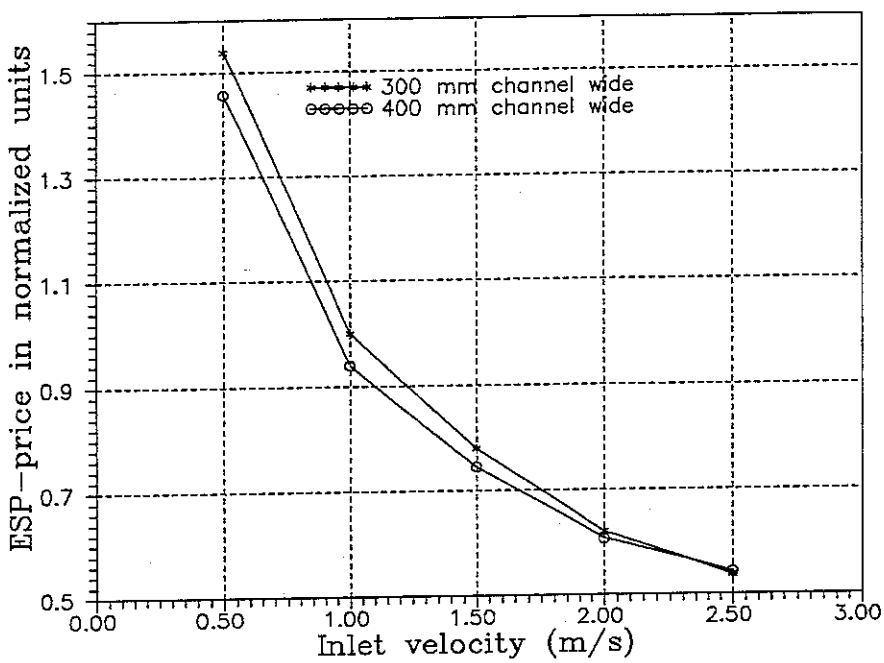

Fig. 8.20 The normalized ESP price versus bulk velocity for two different electrode—collector distances.

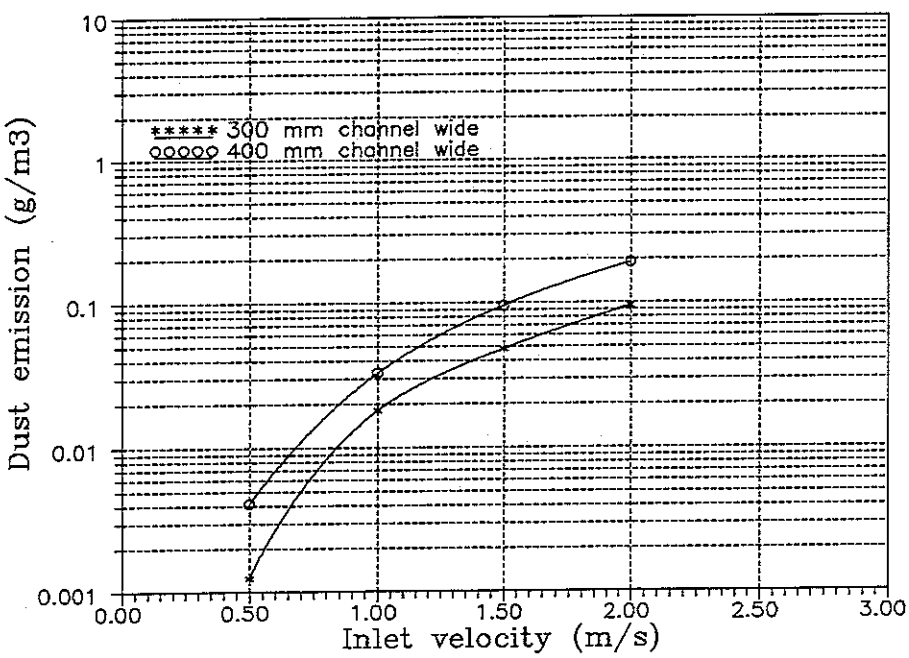

Fig. 8.21 Outlet dust emission versus bulk velocity for two different electrode—collector distances.

8.9 Conclusion and recommendations

The electrostatic precipitation of particulate gases has been the main method in industrial gas cleaning this century. The low energy consumption of this process compared to other removal methods makes ESPs the most attractive facility among large scale gas emission control methods. Therefore, there has been a great interest for further improvement of ESPs through both the experimental methods and theoretical calculations. The improvement of ESPs refers to reduction of both the dust emission level, the size, and the price. Due to the complexity of the process, it is difficult to study the effect of different parameters on the efficiency. Therefore, an effective three–dimensional efficiency calculating model has been developed to predict the particle transport and behavior inside electrostatic precipitators of complex geometries and variable conditions (variation of electric field, flow field and particle drift velocity along the ESP). The program is combined of three main parts solving the, 1) electrical conditions, 2) flow field, and 3) particle transport simultaneously which makes it possible to take the interaction between these elements during the precipitation process into account. It is assumed that the calculation performs for ESPs under normal operating conditions, therefore the influence of dust layer resistivity on the electrical conditions is not included. Furthermore, it is assumed that the dust layer thickness has no influence on the flow near the collector plate.

Since it has not been possible to prepare the experimental facilities for concentration measurements, the experimental data from [8] are used for testing a two dimensional version of calculation program, "ESP". The calculated results show excellent agreement with the experiments.

The main particle charging mechanisms in an ESP are field and diffusion charging where the maximum available charge depends on the particle resident time inside the ESP. Under the effect of a charging electric field particles with different size become differently charged. Therefore, the model takes the influence of the particle size distribution and the resident time of particles into account. The particles are divided into several classes introducing a log–normal size distribution, which is the most common distribution for particulate matters. Particle space charge reduces the production of the ionic space charge, the charging rate and the current density. This interaction between the ionic space charge and the particle space charge is modeled effectively, in which one of the main procedure in present model concerns the calculation of this mechanism.
As far as we know, this interacting mechanism has not been investigated before.

ESPs efficiency reduces by going from the laminar transport to the turbulent transport of particles between the electrodes and the collector plates. This mechanism has also been investigated by [1,2,6,7,10] who conclude that for a higher ESP efficiency the flow must be as laminar as possible. Since, particles in the range of few microns follows the fluctuating motions of the gas, the turbulent diffusion coefficient for particles is assumed to be in the same range as the fluid turbulent diffusion coefficient. From this assumption, a simple analytical expression is derived to calculate the turbulent diffusion coefficient for both the momentum and the particle diffusion. This model requires an empirical estimate for at least one flow condition in order to estimate the diffusion coefficients for other flow conditions.

As particle charge depends on the resident time in the charging electric field, the particles do not reach their saturation charge at the inlet of the ESP. In this region the electric drift velocity and hence the efficiency for individual particles is different from the maximum attainable value. Further, the particle charging rate shows to be strongly affected by the inlet dust loading. Apparently, other efficiency calculating models (see table 3.1) assume that particles reach their maximum charge and hence their maximum drift velocity already at the inlet of ESPs.

Particles of different size precipitate at different axial positions along the ESP. The large particles due to their higher charge are affected by strong Coulomb forces and therefore precipitate before the small ones. This mechanism changes the particle size distribution such that both the mean particle diameter and the geometrical standard deviation decreases in the axial direction.

The turbulence diffusion depends on both the duct width and the bulk velocity, therefore the influence of these parameters can not be investigated separately. The increase of turbulence decreases the laminar transport of the particles to the collector plate and hence lowers the ESPs efficiency.
When the flow velocity increases the particle resident time becomes shorter, and hence the probability for particle precipitation is reduced. When the electrode–collector distance increases, the transversal distance between the particles in the middle of the channel and the collector plate increases which increases the time for particles to reach the plate. The increase of flow velocity and electrode–collector distance decreases the turbulent diffusion and increases the laminar transport of particles, i.e. these parameters have opposite effects on the efficiency. In this the increase of flow velocity or electrode–collector distance dominate, with negative effects, on the ESPs efficiency. Actually, this is a general feature for both the Deutsch equation and the ESP calculation results. However, by increasing of flow velocity or electrode–collector distance, the Deutsch predicted results diverge from the ESP calculated results, in which the Deutsch model predicts the lower values. This implies that in the models using the Deutsch equation as the main tool in prediction of ESPs efficiency give results that become too conservative as the flow velocity or electrode–collector distance increases.

The environmental demands for higher precipitation efficiency have increased the need for more effective and nevertheless cheaper ESP units. If ESPs become smaller without exceeding the required dust emission, the manufacturing price will decreases and the unit may become more competitive. This has given rise to an economical evaluation, with focus on emission requirement for one already existing ESP, in order to examine the calculation results. These evaluations are performed on a FLSmiljø a/s ESP unit (type F) based on an empirical designing model. The evaluations indicate that the ESP price may be reduced by either employing a higher flow velocity or increasing the electrode–collector distance and still be able to fulfill the dust emission requirements. This implies that the current ESP design is near optimal, at least for the narrow parameter range studied. However, we may emphasize, the simple empirical model may not be useful outside this narrow parameter range, and more advanced models, such as the present one, should be used.
Another interesting case to be evaluated is when the ESP length may also vary, as well as the flow velocity and the electrode–collector distance. In this case, the ESP length will be varied in such a way that the penetration level keeps below the required level in all the flow and geometrical conditions. This evaluation may also show interesting results, and therefore it is recommended to be investigated.

Proposals recommended to improve the "ESP" program.

1) Since the aim of the present work was to implement the flow pattern influence on the ESP operation, it is recommended to include a fully three–dimensional flow calculation together with an effective turbulence model for both flow and particles in the "ESP" model.

2) A further development of the back corona model will effectively improve the program ability in efficiency prediction of the complex cases of high resistive dust.

3) Due to the re–entrainment connected with back corona phenomena, plate rapping, and the flow near the dust surface, further investigation is necessary in order to answer the questions concerning the adverse effects on the ESP.
Further improvement of the "ESP" results may be achieved by taking the contribution of the normal re–entrainment into account.

9 Project status: Achieved results compared to plan

A comparison between the planned research work of the present study and the obtained results may be summarized as follows:

a. Scientific objectives

The purpose of this study was to develop a numerical calculation model for prediction of electrostatic precipitation of particulate matters in industrial emission gases. Nevertheless, the the intention of this investigation was to try to optimize the design and the operation of the precipitator with respect to the true gas flow patterns, so called "flow management". As it concerns the modeling of the flow management and the electrostatic conditions, the present model is much more advanced than any other existing commercial model. The present model is distinct from others by the fact that few empirical approximations are necessary to obtain reasonable results. These include mainly turbulence level and effective diffusivity of particles, and electrical characteristics for different electrode configurations. The calculation model gives us confident information about the parameters affecting the ESP design. In order to promote the reliability of this program we suggest that the model should be verified for other large scale ESPs too.

b. Developmental objectives

In the present study there are comparisons between the calculated and the measured current densities for two different emission electrodes where the results show good agreement. Since the calculation model is able to take into account the complex geometrical configurations, it is possible to achieve reliable results. This is also the case with flow management performed for two–dimensional velocity and turbulence distributions. The turbulent gas flow, including the ionic wind is part of the physical model and therefore included in the computer code. Thus, the program can handle the effect of varying axial gas velocity and turbulence intensity on the precipitator efficiency. Changing these parameters deliberately by designing the precipitator internals and choosing important operation parameters correctly, in order to reduce the penetration, is flow management. Here, the influence from the two most important quantities: axial velocity and electrode–collector spacing is investigated, while the influence from the ionic wind and the turbulence is implied in the calculations. It should be mentioned that the influence of flow distribution due to inlet and outlet diffusers on the ESP has not been investigated since this requires a separate fully three–dimensional flow calculation for the whole unit.
Through the modeling of fluctuating electrical conditions it now is possible to take into account the effect of pulse energization on the system. However, this has not been demonstrated.
Before the present study began it was not possible to predict the importance and the influence of the axially variation of the particle space charge on the ESP efficiency and therefore the investigation of this mechanism was ignored. But, the basic investigations in this study has indicated that in order to obtain accurate results it is necessary to take the influence of this parameter into account. Therefore, the variation of particle space charge along the ESP for different classes of particles is modeled and included in the calculations.
Besides, due to time limits in the present study, it has not been possible to perform a basic investigation in order to increase the ESP efficiency by changing the design of electrode–collector plate system. But, on the other hand the tool for these investigations is available now.

c. Applicational objectives

The examination of possible increase in efficiency of a precipitator relative to that of a baghouse filter needs a full comparison of the individual elements from both the application, the manufacturing and the economical point of views. Even though, this comparison has not been the purpose of this project, the result may be valuable for industry.
The present ESP calculation model has made it possible to investigate the influence and the behavior of particles with different size distributions. Here, the turbulent diffusion plays a major roll in transport of particles to the collector plate. The influence of the turbulence on the particle transport in the ESP is modeled by including a diffusive term in the particle transport equation. Here, for more accurate results, the spatial variations of the turbulent diffusion in the system must be known, which demands a turbulence model to be constructed. But, due to time limits in this project, it has not been possible to make such a model.
Furthermore, the plate rapping loss is not included in the model, but the model is constructed in such a way that the influence of this mechanism or other mechanisms, like back corona and dust layer thickness, can be included without difficulty.

References

[1] S.A.Self, K.D.Kihm and M.Mitchner
Precipitator performance improvement through turbulence control. HTGL report No. 2—87. Mechanical Engineering Department, Stanford University, California, USA, Oct. 1987.

[2] K.D.Kihm, M.Mitchner and S.A.Self
Comparision of wire—plate and plate—plate electrostatic precipitator in turbulence flow. J. Electrostatics, 19, pp. 21—32, 1987

[3] G.L.Leonard, M.Mitchner and Self
An experimental study of the electrohydrodynamic flow in electrostatic precipitators. J. Fluid Mech., Vol. 127, pp. 123—140, 1983.

[4] D.H.Choi, S.A.Self, M.Mitchner and R.Leach
Experimental study of ash layer detachment and reentrainment under normal and shear rapping of electrostatic precipitator collector plates. 7th EPA/EPRI Symposiom on Particulate Control Technology, Nashville, Tennessee, Mar. 1989.

[5] S.A.Self, D.H.Choi, M.Mitchner and R.Leach
Experimental study of plate rapping and ash reentrainment. 3rd International confrence on Electrostatic Precipitators, Abano/Venice, Italy, Oct. 1987.

[6] G.Leonard, M.Mitchner and S.A.Self
Particle transport in electrostatic precipitators. 2nd Symposium on the Transfer and Utilization of Particulate Technology, Atmospheric Environment 14, 1980.

[7] S.A.Self, M.Mitchner, D.H.Choi, K.D.Kihm and R.Leach
Finite diffusivity effects in single—stage precipitators theory and experiment. 2nd Symposium on the Transfer and utilization of Particulate Technology, New Orleans, North Carolinna, USA, Feb. 1986.

[8] K.D.Kihm
Effect of nonuniformities on particle transport in electrostatic precipitators. Topical report T—258, Mechanical Engineering Department, Stanford University, USA, 1987.

[9] D.H.Choi, S.A.Self, M.Mitchner and R.Leach
Experimental study of ash rapping off the collector plates in a Lab—scale electrostatic precipitator. 4th Symposium on the Transfer and Utilization of Particulate Technology, San Diago, Californian, USA, Mar. 1990

[10] G.L.Leonard
Effect of turbulence on electrostatic precipitator performance. HTGL report No. 196. Mechanical Engineering Department, Stanford University, USA, 1982.

[11] J.P.Cooch, J.R.McDonald and S.Ogelsby
A Mathematical Model of Electrostatic Precipitator. Southern Research Institute, 2000 Ninth Avenue South, Birmingham, Alabama 35205, USA. Report No. EPA—650/2—75—037 . Apr. 1975.

[12] M.Satna
Determination of an electrostatic precipitator efficiency. A fuzzy sets theory approach.
Staub Reinhaltung der Luft 49, pp. 49—51, Springer—Verlag 1989.

[13] W.J.Liang, M.F.Oheng
Turbulent model for the performance of an ESP. 5th Int. Conf. in Numerical Meth. in Lam. and Turb. Flow, held in Montreal, Canada, 1987.

[14] P.S.Larsen and S.K.Sørencen
Effect of secondary flows and turbulence on electrostatic precipitator efficiency.
The Danish Center for Applied Mathematics and Mechanics. Report AFM No. 279, Feb. 1984.

[15] K.Ushimaru, G.W.Butler
Numerical solution of gas—solid flow in an electrostatic precipitator. ASME, FED—Vol. 10, 1984.

[16] J.R.Von Rosendal, M.R.MaliK, M.Y.Hussaini
Ion—Wind effects on Poiseuille and Blasius flow. AIAA Journal, Vol. 26, No. 8, pp. 961—968, 1988.

[17] J.H.Davidson, E.J.Shaughenccy
An electrostatic precipitator facility for turbulence research. 5th Symposium on the Transfer and Utilization of Particulate Control Technology, Vol. 2, Aug. 1984.

[18] T.Yamamoto, P.A.Lawless, N.Plaks, E.Sparks
Three—dimensional secondary flow and electrohydrodynamics for various electrostatic precipitator configurations. 7th Symposium on the Transfer and Utilization of Particulate Control Technology, Nashville , Tennessee, Mar. 1988.

[19] T.Yamamoto and H.R.Velkoff
Electrodynamic in an electrostatic precipitator. J. Fluid Mech. Vol. 108, pp. 1—18. 1981.

[20] T.Ohkubo, Y.Nomoto, T.Adachi
Electric field in a wire—duct electrostatic precipitator. J. Electrostatics, Vol. 18, pp. 289—303. 1986.

[21] S.Hassid, A.Oron and C.Gutfinger
An asymptotic description of electrostatic precipitator of charged particles in turbulence flow. J. Aerosol Sci. Vol. 18, No. 4, pp. 357—367, 1987.

[22] E.J.Shaughnessy, J.H.Davidson and J.C.Hay
The fluid dynamic of electrostatic precipitators: effect of electrode geometry. 5th Symposium on the Transfer and Utilization of Particulate Control Technology, 1984.

[23] K.Nishino, N.Kasagi, M.Hirata
Three—dimensional particle tracking velocity based on automated digital image processing. Department of Mechanical Engineering, The University of Tokyo, Tokyo 113, Japan. Also ASME, Vol. 111, Dec. 1989.

[24] W.Deutsch
Bewegung und Ladung der Elektrizitatstrager im Zylinderkondensator. Ann. Physik 68 s.335. 1922.

[25] B.Berg
Elektrofilter. Sartruck ur Teknisk Tidskrift, Stockholm. Aug. 1959.

[26] J.R.McDonald, W.B.Smith, and H.W.Spencer III
A Mathematical model for calculating electrical conditions in wire—duct electrostatic precipitation divices. J. Appl. Phys., 48(6), pp. 2231—2243, 1977.

[27] F.S.Maartmann/IØ
Dimensionering av elfiltere. AB Svenska Flaktfabriken, Blad 1 (4). Stockholm, Sweden, Mar. 1965.

[28] J.H.Davidson and P.J.McKinney
Electrodynamic precipitator flow with a barbed plate discharge electrode. Aerosol Science and Technology 12:319—334. 1990.

[29] H.H.Petersen
FLS' w—b theory. Vigerslev Alle 77 DK—2500 Kopenhagen, Denmark. Apr. 1979.

[30] Dr.C.Allander
Einwirkung der Korngrobenverteilung auf den Abschiedungsgrad von Elektrofiltern. Fa. AB Svenska Flæktfabriken, Stockholm, Sweden. HEFT 52, Staub 1957.

[31] H.J.White
INDUSTRIAL ELECTROSTATIC PRECIPITATION. Addison—Wesley, Inc., 1962.

[32] S.Ogelsby, G.B.Nichols
ELECTROSTATIC PRECIPITATION. Marcel—Dekker, Inc., 1978.

[33] V.S.Arpaci, P.S.Larsen
CONVECTION HEAT TRANSFER. Prentice—Hall, Inc, 1984.

[34] S.K.Sørensen
Teoritisk og eksperimental undersøgelse af elektrofilter. Report AFM — EP 88—05, Technical University of Denmark. Jan. 1984.

[35] M.Fischer
Elektrofiltres rensningsgrad. Report AFM — EP 88—05, Technical University of Denmark. Jan. 1988.

[36] L.S.Sørensen
Three—dimensional electro—fluid—dynamic in tuft corona wire—plate precipitator. Report AFM 89—03, Technical University of Denmark. Feb. 1989.

[37] M.Mitchner, S.A.Self
Basic studies to reduce electrostatic precipitators size and cost. EPRI report No. CS—3226 USA. Aug. 1983.

[38] E.Nasser
PARTICLE BREAKDOWN OR CORONAS. Fundamental of gaseous ionization and plasma electronics, Wiley, New York. 1971.

[39] H.Tennekes, J.L.Lumley
A FIRST COURSE IN TURBULENCE. The MIT press Cambridge. Mar. 1972.

[40] I.W.McAllister, G.C.Crichton, and E.Bregnsbo
Experimental study on the onset of positive corona in atmospheric air. Department of Physics, Building 309B, Technical University of Denmark, DK—2800 Lyngby, Denmark. 1985.

[41] K.D.Kihm
Effect of nonuniformities on particle transport in electrostatic precipitator. HTGL topical report T–258, Mechanical Engineering Department, Stanford University, California, USA. Mar. 1987.

[42] P.Kumar and C.A.Sastsy
Charging of aerosol particles by unipolar ions with an applied electric field. J. Environmental Protection, vol. 8, pp.568–585, Aug. 1988.

[43] P.A.Lawless
Numerical solution of Laplaces equation and ion current flow by the use of flux–tube/equipotential relaxation. Research Triangle Institute, P.O.Box. 12194, USA. IEEE 1989.

[44] C.Hirsch
An analysis of flow models: from Navier–Stokes to potential flow equations. Lecture Series 1990–04, von Karman Institute for Fluid Dynamics, Belgium. Apr. 1990.

[45] J.H.Vincent
Aerosol sampling science and practice. Institute of Occupational Medicine, Edinburgh, UK. 1989.

[46] H.P.Thomsen
Strømningundersøgelse i et tråd–plade elektrofilter med negative corona. Rapport AFM 83–02, Technical University of Denmark. Jan. 1983.

[47] L.Barlbo, P.Carslund
Strømning i elektrofilter. Rapport AFM–EP 80–05, Technical University of Denmark, Denmark. Dec. 1980.

[48] L.Guangda, E.M.Christensen, P.S.Larsen
LDA–study of flow fields in electrostatic precipitator. Rapport AFM 84–05. Technical University of Denmark. Dec. 1984.

[49] S.K.Sørensen
Teoretisk og eksperimentel undersøgelse af electrofilter. Int. raport AFM 84–02, Technical University of Denmark. Jan. 1984.

[50] J.Zamany
Turbulence in electrostatic precipitators. AFM 90–07, Technical University of Denmark. Feb. 1990.

[51] S.A.Self
Private communication, Mechanical Engineering Department, Stanford University, USA. Mar. 1990.

[52] P.A.Lawless
Private communication. EPRI conference, San Diago, USA. Mar. 1990.

[53] FLS miljø a/s
Internal papers on the methods and experimental works. F.L.Smidth Company, Vigerslev Alle 77, DK–2500 Valby, Denmark. 1990.

[54] T.Bjerge
ELECTRON— OG ATOMFYSIK
Ejnar Munksgaard, København. 1954.

[55] C.E.Akerlund
A method for calculating electric field and current distributions along profiled collecting electrodes in a wire—plate electrostatic precipitator. Flækt Industri AB, Sweden. Presented in thrid international conference on Electrostatic precipitation in Italy. Oct. 1987.

[56] S.V.Patankar
NUMERICAL HEAT TRANSFER AND FLUID FLOW. Hemispher Publishing Corporation, New York. 1980.

[57] W.F.Ames
NUMERICAL METHODS FOR PARTIAL DIFFERENTIAL EQUATIONS. Second Edition, Academic press, New York, USA. 1977.

[58] H.P.Thomsen, E.M.Christensen, J.V.Christensen, P.S.Larsen
Forsøgskanal for strømningsundersøgelse i electrofilter. Raport AFM 81—03, Technical University of Denmark. Jun. 1981.

[59] O.J.Tassicker
Ph.D Dissertation. Department of Elec. Eng., Wallongong University College. Univ. New South Wales, Oct. 1977.

[60] J.R.MaDonald, M.H.Ogerson and R.B.Mosley
Charge measurements on individual particles exiting labratory precipitators with positive and negative corona at various tempratures. J. Appl. Phys., vol.51, 3632—3643. 1980.

[61] P.A.Lawless, L.E.Sparks
Measurments of ion mobilities in air and sulfurdioxide—air mixture as a function of temperature. Atmospheric Enviroment, Vol. 14, pp. 199—217, 1986.

[62] P.S. Larsen
Secondary flows in negative corona precipitator
DCAMM Report No.337, Technical University of Denmark. Oct. 1986.

[63] L.S. Sørensen, P.S. Larsen, E.M. Christensen and J.V. Christiansen
Secondary flow and turbulence in negative corona precipitator with large—diameter, barbed electrodes. Proc. Third Int. Conf. on Electrostatic Precipitation, Abano, Italy, Oct. 1987.

[64] J.N. Sørensen, P.S. Larsen And J.Zamany
Experimental and Numerical Analysis for Flows in Negative Corona Precipitator.
Proc. Eigth Int. Conf. on Electrostatic Precipitation, 13—3 Technical University of Munich, Sep. 1991.

[65] J. Zamany
Roll inspection in negative corona precipitators. Rapport AFM — EP 89—03, Technical University of Denmark, Feb. 1989.

Appendix A

Discretization of electric field equation

This appendix concerns the discretization of the electric field equations. The potential field equation, Eq.(6.15) in two dimension can be derived as

$$\frac{\partial^2 \varphi}{\partial x^2} + \frac{\partial^2 \varphi}{\partial y^2} = - \frac{\rho_i + \rho_p}{\epsilon_0} . \tag{A1}$$

Central difference in x-direction gives:

$$\frac{\partial^2 \varphi}{\partial x^2} \simeq \frac{\varphi_{i+1,j} - 2\varphi_{i-j} + \varphi_{i-1,j}}{\Delta x^2} . \tag{A2}$$

And central difference in y-direction gives:

$$\frac{\partial^2 \varphi}{\partial x^2} \simeq \frac{\varphi_{i,j+1} - 2\varphi_{i,j} + \varphi_{i,j-1}}{\Delta y^2} . \tag{A3}$$

For

$$\rho_i = \rho_{i_{i,j}} ,$$

$$\rho_p = \rho_{p_{i,j}} ,$$

hence

$$\varphi_{i,j} \left[\frac{2}{\Delta x^2} + \frac{2}{\Delta y^2} \right] = \frac{1}{\Delta x^2} \varphi_{i+1,j} + \frac{1}{\Delta x^2} \varphi_{i-1,j} + \frac{1}{\Delta y^2} \varphi_{i,j+1} +$$

$$\frac{1}{\Delta y^2} \varphi_{i,j-1} + \frac{\rho_{i_{i,j}} + \rho_{p_{i,j}}}{\epsilon_0}$$

or

$$A_p \varphi_{i,j} = A_e \varphi_{i+1,j} + A_w \varphi_{i-1,j} + A_n \varphi_{i,j+1} + A_s \varphi_{i,j-1} + S_p , \tag{A4}$$

where

$$A_p = \frac{2}{\Delta x^2} + \frac{2}{\Delta y^2} \quad , \quad A_e = \frac{1}{\Delta x^2} \quad , \quad A_w = \frac{1}{\Delta x^2} ,$$

$$A_s = \frac{1}{\Delta y^2} \quad , \quad A_n = \frac{1}{\Delta y^2} \quad \text{and} \quad S_p = \frac{\rho_{i_{i,j}} + \rho_{p_{i,j}}}{\epsilon_0}$$

are the influence coefficients of the three-diagonal matrix.

The ionic transport equation, Eq.(6.20)

$$E \cdot \nabla \rho + (\rho_i + \rho_p) \frac{\rho}{\epsilon_0} = 0 , \tag{A5}$$

in two dimensions can be derived as

$$E_x \cdot \frac{\partial \rho}{\partial x} + E_y \cdot \frac{\partial \rho}{\partial y} + (\rho_i + \rho_P)\frac{\rho}{\epsilon_0} = 0 \,. \tag{A6}$$

The discretization in x–direction gives

$$E_x \cdot \frac{\partial \rho}{\partial x} = E_{x,i,j} \cdot \frac{A\cdot\rho_{i+1,j} + B\cdot\rho_{i,j} - A\cdot\rho_{i,j} - B\cdot\rho_{i-1,j}}{(A+B)\cdot\Delta x} \tag{A7}$$

where

$$\left.\begin{array}{l} A = 0 \quad B = 1 \quad \text{for} \quad E_x > 0 \\ A = 1 \quad B = 0 \quad \text{for} \quad E_x < 0 \end{array}\right\} \text{ upwinding, x–direction}$$

And the discretization in y–direction gives

$$E_y \cdot \frac{\partial \rho}{\partial y} = E_{y,i,j} \cdot \frac{C\cdot\rho_{i,j+1} + D\cdot\rho_{i,j} - C\cdot\rho_{i,j} - D\cdot\rho_{i,j-1}}{(C+D)\cdot\Delta y} \tag{A8}$$

where

$$\left.\begin{array}{l} C = 0 \quad D = 1 \quad \text{for} \quad E_y > 0 \\ C = 1 \quad D = 0 \quad \text{for} \quad E_y < 0 \end{array}\right\} \text{ upwinding, y–direction}$$

For

$$\left.\begin{array}{l} \rho_i = \rho^{old}_{i,j} \\ \rho_P = \rho_{P_{i,j}} \\ \rho = \rho_{i,j} \end{array}\right\} \Rightarrow (\rho_i + \rho_P)\frac{\rho}{\epsilon_0} = \left[\rho^{old}_{i,j} + \rho_{P_{i,j}}\right]\frac{\rho_{i,j}}{\epsilon_0} \,,$$

hence

$$\rho_{i,j}\left[\frac{E_{x_{i,j}}(B-A)}{(A+B)\Delta x} + \frac{E_{y_{i,j}}(C-D)}{(C+D)\Delta y}\frac{\rho^{old}_{i,j} + \rho_{P_{i,j}}}{\epsilon_0}\right] = \tag{A9}$$

$$\frac{E_{x_{i,j}}}{(A+B)\Delta x}(A\cdot\rho_{i+1,j} - B\cdot\rho_{i-1,j}) - \frac{E_{y_{i,j}}}{(C+B)\Delta y}(C\cdot\rho_{i,j+1} - B\cdot\rho_{i,j-1})$$

or

$$\rho_{i,j}\cdot A_P = A_e\,\rho_{i+1,j} + A_w\cdot\rho_{i-1,j} + A_n\cdot\rho_{i,j+1} + A_S\cdot\rho_{i,j-1} \tag{A10}$$

where

$$A_P = \left[\frac{E_{x_{i,j}}(B-A)}{(A+B)\Delta x} + \frac{E_{y_{i,j}}(C-D)}{(C+D)\Delta y}\frac{\rho^{old}_{i,j} + \rho_{P_{i,j}}}{\epsilon_0}\right] ,$$

$$A_e = \frac{A \cdot E_{x_{i,j}}}{(A+B)\Delta x}, \quad A_w = \frac{B \cdot E_{x_{i,j}}}{(A+B)\Delta x},$$

$$A_n = \frac{C \cdot E_{y_{i,j}}}{(C+D)\Delta y} \quad \text{and} \quad A_s = \frac{D \cdot E_{y_{i,j}}}{(C+D)\Delta y}$$

are influence coefficiets of the three diagonal matrix.

Appendix B

One dimensional solution of electric field equations with influence of space charge

This appendix concerns the solution of the electric field condition for the case with two parallel plates, one with potential φ_0 and a uniform corona discharge of ρ_0 and the other one grunded. The governing equation is

$$\frac{d^2\varphi}{dy^2} = -\frac{\rho}{\epsilon_0}, \tag{B1}$$

where, for

$$-\frac{d\varphi}{dy} = E, \tag{B2}$$

then we can write

$$\frac{dE}{dy} = \frac{\rho}{\epsilon_0}. \tag{B3}$$

Accorrding to conservation of current,

$$\frac{dJ}{dy} = 0 \tag{B4}$$

or

$$J = \text{constant}.$$

The current density is defined as

$$J = E \cdot \rho \cdot b, \tag{B5}$$

which leads to

$$\rho = \frac{J}{E \cdot b}. \tag{B6}$$

Inserting Eq.(B6) into Eq.(B3) leads to

$$\frac{dE}{dy} = \frac{J}{\epsilon_0 \, E \, b}$$

or

$$\int E \, dE = \int \frac{J}{\epsilon_0 \, b} \, dy,$$

which after the integration will give

$$E = \sqrt{\frac{2J}{\epsilon_0 \, b} \, y}. \tag{B7}$$

Imploying Eq.(B7) in Eq.(B2), leads to

$$\varphi = -\frac{2}{3}\sqrt{\frac{2J}{\epsilon_0 \, b}} \cdot y^{2/3} + c_1. \tag{B8}$$

The boundary conditions at the electrode plate is

$$\varphi = \varphi_0 \quad \text{for} \quad y = 0,$$

which gives

$$c_1 = \varphi_0 .$$

And the boundary condition at the collector plate is

$$\varphi = 0 \quad \text{for} \quad y = l_y,$$

which gives

$$\left[\frac{3}{2}\frac{\varphi_0}{l_y^{3/2}}\right]^2 = \frac{2}{b}\frac{J}{\epsilon_0}$$

or

$$J = \frac{9}{8} \cdot \frac{\varphi_0^2 \cdot b \cdot \epsilon_0}{l_y^3} . \tag{B9}$$

Inserting this equation into Eq.(B8) gives

$$\varphi = -\varphi_0\left[\frac{y}{l_y}\right]^{3/2} + \varphi_0 . \tag{B10}$$

And inserting Eq.(B9) into Eq.(B6) and Eq.(B7) lead to

$$\rho = \frac{3}{4}\frac{\varphi_0 \ \epsilon_0}{l_y\sqrt{l_y}} \cdot \frac{1}{\sqrt{y}}, \tag{B11}$$

and

$$E = \frac{3}{2}\frac{\varphi_0}{l_y} \cdot \sqrt{\frac{y}{l_y}} . \tag{B12}$$

Appendix C

Mass/number of density distributtion measurements of seeding particles

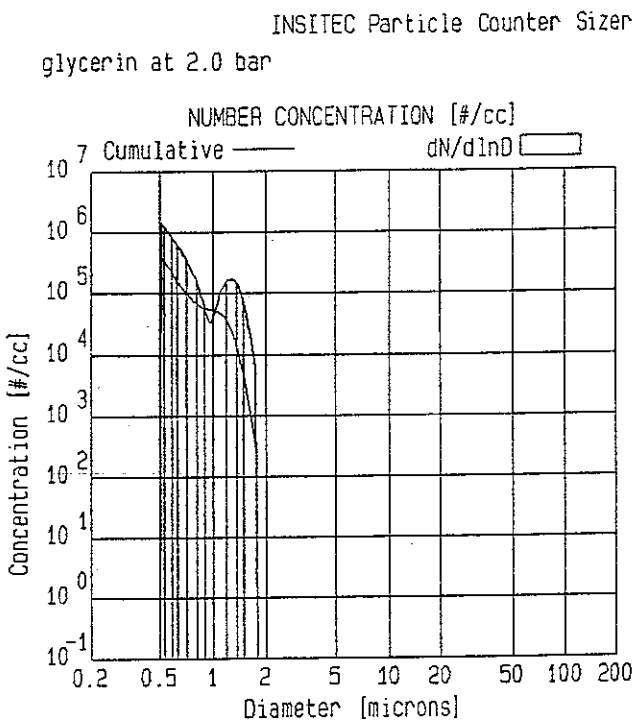

File	: GLYE
Date	: 2/3/1987
Time	: 10:05:22
Trans.	: 81.8 %
Valid	: 97.7 %
Speed	: 1.14 ± 0.45
Density	: 2.70 gm/cc
D32	: 0.92 microns
Oversize:	0.0 %

%	Diam	Cum Numb
99.9	0.50	3.9E+05
99.0	0.50	3.8E+05
90.0	0.51	3.5E+05
70.0	0.54	2.7E+05
50.0	0.60	1.9E+05
30.0	0.69	1.2E+05
10.0	1.19	3.9E+04
1.0	1.50	3.9E+03
0.1	1.72	3.9E+02

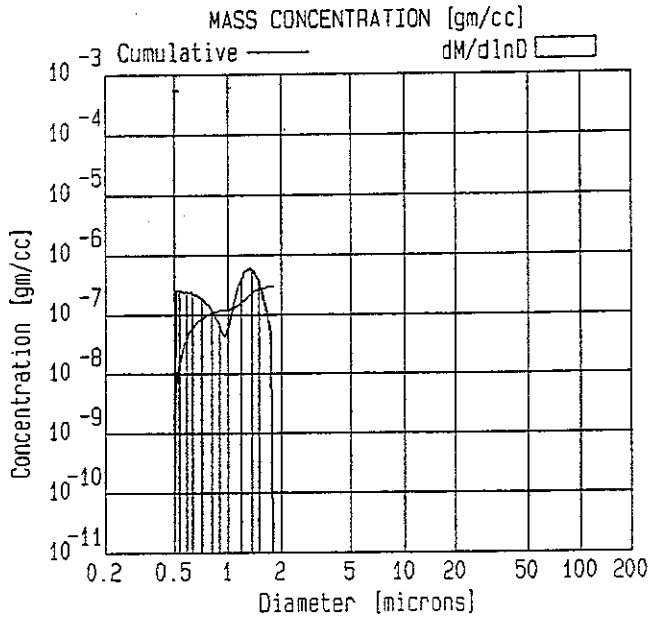

File	: GLYE
Date	: 2/3/1987
Time	: 10:05:22
Trans.	: 81.8 %
Valid	: 97.7 %
Speed	: 1.14 ± 0.45
Density	: 2.70 gm/cc
D32	: 0.92 microns
Oversize:	0.0 %

%	Diam	Cum Mass
99.9	1.74	2.9E-07
99.0	1.67	2.8E-07
90.0	1.48	2.6E-07
70.0	1.32	2.0E-07
50.0	1.17	1.4E-07
30.0	0.72	8.6E-08
10.0	0.55	2.9E-08
1.0	0.50	2.9E-09
0.1	0.49	2.9E-10

Appendix D

Particle space charge influence on the electric field between two parallel plates

This appendix derives and solves the governing equation for the case where precharged particles enters a region of uniform electric field between two parallel plates, so

$$\frac{d^2\varphi}{dy^2} = -\frac{\rho_P}{\epsilon_0}, \tag{D1}$$

where φ is the potential, ρ_P is the particle space charge, ϵ_0 is the air permitivity.

Assuming a uniform distributed particle charge (uniform charged particle concentration) in between the plate electrode and the collector plate leads to

$$\frac{d\varphi}{dy} = -\frac{\rho_P}{\epsilon_0} y + c_1 \tag{D2}$$

or

$$\varphi = -\frac{1}{2}\frac{\rho_P}{\epsilon_0} y^2 + c_1 y + c_2 . \tag{D3}$$

Boundary conditions are:

$$\varphi = \varphi_0 \quad \text{for} \quad y = 0$$

and

$$\varphi = 0 \quad \text{for} \quad y = l_y .$$

Inserting these boundary conditions into Eq.(D3) leads to

$$\varphi = -\frac{1}{2}\frac{\rho_P}{\epsilon_0} y^2 - \frac{\varphi_0 - \frac{1}{2}\frac{\rho_0}{\epsilon_0} l_y^2}{l_y} y + \varphi_0 \tag{D4}$$

and

$$E = -\frac{d\varphi}{dy} = -\frac{\rho_P}{\epsilon_0} y - \frac{\varphi_0}{l_y} + \frac{1}{2}\frac{\rho_P}{\epsilon_0} l_y . \tag{D5}$$

Then, at $y = \frac{1}{2} l_y$ the electric field, E, equals $-\frac{\varphi_0}{l_y}$.

FLS miljø a/s
Ramsingsvej 30, DK-2500 Valby
Copenhagen, Denmark
Telephone +45-36 18 11 00
Telefax +45-31 17 45 99
Telex 19053 flsem dk

Agents and representatives in:
Brazil, Canada, F.R. of Germany, Finland, France, India, Indonesia, Italy, Japan, Korea, Mexico, Poland, P.R. of China, Spain, Sweden, Taiwan R.O.C., Thailand, Turkey, United Kingdom and USA